INFORMATION TO USERS

This material was produced from a microfilm copy of the original document. While the most advanced technological means to photograph and reproduce this document have been used, the quality is heavily dependent upon the quality of the original submitted.

The following explanation of techniques is provided to help you understand markings or patterns which may appear on this reproduction.

1. The sign or "target" for pages apparently lacking from the document photographed is "Missing Page(s)". If it was possible to obtain the missing page(s) or section, they are spliced into the film along with adjacent pages. This may have necessitated cutting thru an image and duplicating adjacent pages to insure you complete continuity.

2. When an image on the film is obliterated with a large round black mark, it is an indication that the photographer suspected that the copy may have moved during exposure and thus cause a blurred image. You will find a good image of the page in the adjacent frame.

3. When a map, drawing or chart, etc., was part of the material being photographed the photographer followed a definite method in "sectioning" the material. It is customary to begin photoing at the upper left hand corner of a large sheet and to continue photoing from left to right in equal sections with a small overlap. If necessary, sectioning is continued again – beginning below the first row and continuing on until complete.

4. The majority of users indicate that the textual content is of greatest value, however, a somewhat higher quality reproduction could be made from "photographs" if essential to the understanding of the dissertation. Silver prints of "photographs" may be ordered at additional charge by writing the Order Department, giving the catalog number, title, author and specific pages you wish reproduced.

5. PLEASE NOTE: Some pages may have indistinct print. Filmed as received.

University Microfilms International
300 North Zeeb Road
Ann Arbor, Michigan 48106 USA
St. John's Road, Tyler's Green
High Wycombe, Bucks, England HP10 8HR

78-4736

KESSLER, Robert Charles, 1948-
A NUMERICAL STUDY OF CLEAR-SKY NOCTURNAL FOG.

The University of Michigan,
Ph.D., 1977
Physics, atmospheric science

University Microfilms International, Ann Arbor, Michigan 48106

A NUMERICAL STUDY OF CLEAR-SKY NOCTURNAL FOG

by
Robert Charles Kessler

A dissertation submitted in partial fulfillment
of the requirements for the degree of
Doctor of Philosophy
(Atmospheric Science)
in The University of Michigan
1977

Doctoral Committee:

Associate Professor Dennis G. Baker, Chairman
Professor Donald J. Portman
Professor Ralph G. Smith
Harry Moses, U.S. Energy Research and
Development Administration

ACKNOWLEDGEMENTS

I thank Professor Dennis G. Baker for serving as chairman of my dissertation committee. Professor Baker has provided encouragement, advice, and support throughout this study.

Dr. Harry Moses has always found time to see me during his busy monthly visits to Ann Arbor. I thank him for his down-to-earth approach and for his many helpful suggestions.

I thank Professors Donald J. Portman and Ralph G. Smith for their review and criticism of the manuscript.

Ms. Becky Glover exhibited a great deal of diligence and fortitude in typing the manuscript.

Finally, I would like to thank my fellow residents of John Nakamura Co-op for providing a stimulating living environment during my period of graduate study, and for their tolerance of my piano improvisations.

TABLE OF CONTENTS

ACKNOWLEDGEMENTS.....ii

LIST OF TABLES.....iv

LIST OF FIGURES.....v

CHAPTER I: INTRODUCTION.....1

CHAPTER II: BACKGROUND.....4

CHAPTER III: DESCRIPTION OF THE MODEL.....15

CHAPTER IV: VERIFICATION OF THE MODEL.....39

CHAPTER V: ANALYSIS OF MODEL SENSITIVITY.....76

CHAPTER VI: CONCLUSIONS.....111

REFERENCES.....116

LIST OF TABLES

Table		Page
4.1	Relevant data for selected Flint Fog cases	42
4.2	Comparison of model and observed fog onset times	44
4.3	Hourly observations at Flint: 20-21 SEP 1960	55
4.4	Hourly observations at Flint: 15-16 SEP 1963	63
4.5	Relevant data for selected Flint "no-fog" cases	70

LIST OF FIGURES

Figure		Page
3.1:	Schematic diagram of initial soil temperature profile	19
3.2:	Contribution of a water-vapor slab to the downward flux of long-wave radiation at the surface	28
4.1:	Comparison of model-generated temperature and dew point with Flint hourly observations for case 1	45
4.2:	As in Fig. 4.1, for case 2	46
4.3:	As in Fig. 4.1, for case 3	46
4.4:	As in Fig. 4.1, for case 4	47
4.5:	As in Fig. 4.1, for case 5	47
4.6:	As in Fig. 4.1, for case 6	48
4.7:	As in Fig. 4.1, for case 7	48
4.8:	As in Fig. 4.1, for case 8	49
4.9:	As in Fig. 4.1, for case 9	49
4.10:	As in Fig. 4.1, for case 10	50
4.11:	As in Fig. 4.1, for case 11	50
4.12:	Model-generated profiles of specific humidity for case 6	52
4.13:	Comparison of model-generated temperature and dew point with Flint hourly observations for both pre- and post-fog periods, case 3	57
4.14:	Evolution of pre-fog θ profile, case 3	58
4.15:	As in Fig. 4.14, for K	58
4.16:	Evolution of post-fog θ profile, case 3	59
4.17:	As in Fig. 4.16, for K	59
4.18:	As in Fig. 4.16, for ℓ	60

Figure		Page
4.19:	Model-generated ℓ at z=1 m as a function of time, case 3	60
4.20:	Comparison of model-generated temperature and dew point with Flint hourly observations for both pre- and post-fog periods, case 10	64
4.21:	Evolution of pre-fog θ profile, case 10	65
4.22:	As in Fig. 4.21, for K	65
4.23:	Evolution of post-fog θ profile, case 10	66
4.24:	As in Fig. 4.23, for K	66
4.25:	As in Fig. 4.23, for ℓ	67
4.26:	Model-generated ℓ at z=1 m as a function of time, case 10	67
4.27:	As in Fig. 4.1, for case 12	71
4.28:	As in Fig. 4.1, for case 13	71
4.29:	As in Fig. 4.1, for case 14	72
4.30:	As in Fig. 4.1, for case 15	72
4.31:	As in Fig. 4.1, for case 16	73
4.32:	As in Fig. 4.1, for case 17	73
5.1:	Initial soil temperature profiles: basic run, run B1, and run B2	78
5.2:	Model-predicted θ at z=1 m: basic run, run B1, and run B2	79
5.3:	Model-predicted θ at z=1 m: basic run, run C1, and run C2	82
5.4:	Model-predicted θ at z=1 m: basic run, run C3, and run C4	83
5.5:	Initial θ profiles: basic run and run D1	86
5.6:	Model-predicted θ at z=1 m: basic run and run D1	87
5.7:	Model-predicted q at z=1 m: basic run and run D1	88

Figure		Page
5.8:	Model-predicted q at z=1 m: basic run and run E1	90
5.9:	Profiles of q at t=3.5 hr: basic run and run E2	91
5.10:	Relative humidity computed from model θ and q at z=1 m, for case 6	93
5.11:	Initial K profiles: basic run, run G1, and run G2	95
5.12:	Model-predicted θ at z=1 m: basic run, run G1, and run G2	96
5.13:	Profiles of θ at t=7 hr: basic run, run G1, and run G2	97
5.14:	Profiles of q at t=7 hr: basic run, run G1, and run G2	98
5.15:	Model-predicted θ at z=1 m: basic run and run G3	101
5.16:	Model-predicted θ at z=1 m: basic run, run H1, and run H2	103
5.17:	Model-predicted ℓ at z=1 m: basic run, run H1, and run H2	104
5.18:	Profiles of ℓ at t=4 hr: basic run, run H1, and run H2	105
5.19:	Profiles of ℓ at t=6 hr: basic run and run H1	106
5.20:	Model-predicted θ at z=1 m: basic run, run H3, and run H4	107
5.21:	Model-predicted ℓ at z=1 m: basic run, run H3, and run H4	108
5.22:	Profiles of ℓ at t=6 hr: basic run, run H3, and run H4	110

CHAPTER I: INTRODUCTION

Reliable forecasts of fog are of great economic value. Significant visibility reduction can impede both air and ground transportation. Also, the presence of fog can exacerbate the effects of chemical pollutants.

Nomograms relating nocturnal fog occurrence to observed meteorological variables at or near sunset have been developed for a number of locations, most notably by George (1950). These nomograms are based upon climatological data. While useful in the making of forecasts, such a nomogram accounts for atmospheric processes only in a statistical sense. Presumably, fog forecasts could be much improved by direct and effective simulation of the relevant physical processes in a numerical model.

Numerical fog models have been developed previously by Fisher and Caplan (1963), Zdunkowski and Nielsen (1969), Zdunkowski and Barr (1972), Pilie *et al.* (1972), Lala *et al.* (1975), and Brown and Roach (1976). In all previous fog modelling experiments except that of Lala *et al.*, the major objective has been to reproduce the features of a typical nocturnal fog situation. To fulfill this objective, hypothetical initial conditions for the models seem to be formulated to produce a model fog. While such an approach may illustrate the physics of fog growth, it does not address the problem of predicting whether or not fog will form.

The major objective of Lala et al., on the other hand, was to predict the onset of fog. Of the previous models, theirs is the only one which is tested against observations; initial conditions for the Lala model are obtained from each of four radiosonde soundings at Albany, New York. However, Lala et al. do not carry their modelling beyond the onset of fog at shelter level.

The model used in this study has been designed to predict both the onset and development of fog on clear nights. The study has two objectives: (1) to investigate the relative roles of various physical processes in fog formation; and (2) to determine whether or not such a model is a viable forecast tool. The current model incorporates important features of previous models.

A major aspect of the study has been the comparison of the model with observations. Eleven cases in which fog was observed to form on clear nights at Flint, Michigan, along with six cases in which fog did not form, were selected for model verification. A model run is made in each of these cases, with initial conditions formulated from 0000 GMT radiosonde data. Model results are then compared with hourly shelter-level observations of temperature, dew point, and visibility.

The response of the model to changes in each of several assumptions and parameters has been evaluated. In addition to testing the sensitivity of the model, this in-

vestigation examines the relationship of various characteristics of the atmosphere and soil to fog formation, and highlights areas in which observational research is needed to further improve fog forecasts.

Chapter II of the thesis includes a discussion of the physics of fog formation and a summary of the content and results of previous fog models. Chapter III contains a detailed description of the current model. The results of model verification are presented and discussed in Chapter IV. The sensitivity of the model is evaluated in Chapter V. Conclusions and suggestions for further research are presented in Chapter VI.

CHAPTER II: BACKGROUND

A. PHYSICS OF FOG FORMATION

According to international definition, a "fog" is a cloud of water droplets which envelops an observer at the earth's surface and restricts his visibility to 1 km or less. (The U.S. Airways Code allows an observer to report "fog", "ice fog", or "ground fog" for obstructions to visibility up to 7 miles). For fog to form, the air must be sufficiently saturated for condensation to occur. The relative humidity at which condensation commences is dependent upon the number and chemical composition of available condensation nuclei. In non-polluted areas, this relative humidity is close to 100%; in heavily polluted urban areas, where nuclei are abundant, fog droplets can appear at relative humidities as low as 80% (George, 1950).

Four mechanisms may effect the saturation of initially unsaturated low-level air: (1) vertical transfer of heat and moisture by turbulent eddies; (2) long-wave radiative cooling of the surface and lower atmosphere; (3) heat loss or moisture gain through horizontal advection; and (4) evaporation of water into the air. Once saturation has been attained, visibility and fog extent are governed by the microphysical processes of nucleation and droplet growth.

An ideal fog prediction model should include accurate

representations of all macrophysical and microphysical processes involved in fog formation. However, in this model, an ensemble of fog droplets is characterized as a mass of liquid water; water phase change is treated as a macrophysical process adding to or subtracting from the total liquid water content at a given level of the fog.

B. CONTENT OF PREVIOUS FOG MODELS

The fog models mentioned in the previous chapter are similar in principle, although they differ in various details. All of the models are based upon the assumption that the potential temperature (θ), specific humidity (q), and liquid water concentration (ℓ) are governed by equations of the form

$$\frac{\partial Q}{\partial t} = \frac{\partial}{\partial z}\left(K\frac{\partial Q}{\partial z}\right) + \vec{V}_2 \cdot \vec{\nabla}_2 Q + S \qquad (2.1)$$

where Q is the variable under consideration, K is the turbulent exchange coefficient, $\vec{V}_2$ is the horizontal wind vector, $\vec{\nabla}_2 Q$ is the horizontal gradient of Q, and S represents sources and sinks of Q. The first and second terms on the right-hand side of (2.1) account for turbulent exchange and advection of Q, respectively. The source-sink term S accounts for any change in Q resulting neither from turbulent exchange nor from advection. S includes the effects of long-wave flux divergence, water phase change,

and droplet settling.

Starting from a given set of initial conditions, representative of conditions before fog formation, the model equations are integrated with respect to time. Provision is made for adjustments of θ, q, and ℓ, wherever and whenever the model atmosphere becomes saturated. The profile of ℓ indicates the density and vertical extent of the fog.

If advection is omitted, a model is one-dimensional, requiring upper and lower boundary conditions on the prognostic variables. If advection is included, lateral boundary conditions are also specified.

All of the above models were initially applied to fog situations in which advection is unimportant, and thus omit the advection term in (2.1). The Fisher-Caplan and Pilie models were later modified to include advection by imposition of a logarithmic wind profile and lateral boundary conditions (Mack et al, 1973). Since the model developed in this study is one-dimensional, the discussion which follows concerns one-dimensional models only.

The various models differ among themselves in four major areas: (1) lower boundary conditions on heat and moisture; (2) treatment of long-wave radiation; (3) the formulation of the turbulent exchange coefficient; and (4) the treatment of droplet settling.

As a lower boundary condition for heat, the Fisher-

Caplan model simply constrains θ to vary in a prescribed manner at the surface. In all other models, a balance between the fluxes of radiant, sensible, and latent heat

$$Q_R - Q_A - Q_L + Q_S = 0 \qquad (2.2)$$

is imposed at the surface. Here Q_R is the net upward long-wave flux at the surface, Q_A is the turbulent flux of sensible heat from the atmosphere to the surface, Q_L is the turbulent flux of latent heat from the atmosphere to the surface, and Q_S is the flux of sensible heat from the soil to the surface. Use of equation (2.2) requires the inclusion of a prognostic equation for soil temperature

$$\frac{\partial T_s}{\partial t} = k_s \frac{\partial^2 T_s}{\partial z^2} \qquad (2.3)$$

where T_S is soil temperature and k_s is soil diffusivity. T_s is held constant at a specified depth.

The lower boundary conditions on moisture employed in the Fisher-Caplan, Zdunkowski-Nielsen, and Zdunkowski-Barr models result in conservation of the total moisture in an air column. Fisher and Caplan require the fluxes of vapor and liquid water to be zero at the surface at all times; the Zdunkowski-Nielsen and Zdunkowski-Barr models require a constant surface specific humidity before fog formation and the flux of total moisture ($q+\ell$) to be zero at the surface during fog.

Such boundary conditions preclude the formation of

dew, a process which can inhibit saturation by removing moisture from the lower layers of the atmosphere. The Pilie, Lala, and Brown-Roach models account for dew formation by allowing surface condensation after the surface has cooled to its saturation point. When the surface is unsaturated, a no-flux condition on water vapor is maintained.

Long-wave radiation contributes to the cooling of the lower atmosphere in two ways. Cooling of the surface through radiation results in a turbulent flux of heat from the atmosphere to the surface. The atmosphere is also cooled by the divergence of the long-wave flux resulting from absorption, re-radiation, and scattering by water vapor and liquid water (Geiger, 1965).

In the Fisher-Caplan model, the forcing of θ at the model surface ostensibly incorporates the effects of surface radiative heat loss. Long-wave flux divergence is ignored in this model.

In the Pilie model, the surface is assumed to radiate as a black body. In the absence of fog, the downward long-wave flux at the surface is assumed to equal three-fourths the black body value. This yields an assumed net surface flux equal to $0.25\sigma T_o^4$, where σ is the Stefan-Boltzman constant and T_o is the model surface temperature. When model fog is present, a bulk extinction coefficient, computed from an idealized droplet size distribution,

characterizes absorption of long-wave radiation by the fog droplets; the computation of net surface flux and flux divergence within the fog is based on this coefficient. The Pilie model ignores long-wave flux divergence due to water vapor.

In the Zdunkowski-Nielsen, Zdunkowski-Barr, Lala, and Brown-Roach models, net surface long-wave flux and atmospheric radiative cooling are directly computed from the vertical profiles of θ, q, and ℓ generated by the models. In general, these computations are based upon tabulated water vapor emissivities and upon assumed relationships between fog droplet size distribution and liquid water content.

Time-independent vertical profiles of the turbulent exchange coefficient K are utilized by the Fisher-Caplan, Zdunkowski-Nielsen, Lala, and Brown-Roach models. Generally, in these models K is determined by a polynomial function of height in which the maximum K value and height of the maximum are varied for different model runs.

Fisher and Caplan also used a K profile which is a product of (1) an arbitrary function of height and (2) a function of the model-generated stability.

The Pilie and Zdunkowski-Barr models generate K profiles at each model time step. Pilie et al. derive an expression for K which depends on a combination of the model-predicted stability and a friction velocity u_*, which must

be externally specified. In the Zdunkowski-Barr model, prognostic equations for momentum are solved at each time step to obtain wind profiles; K is then computed from these wind profiles, using the expression formulated by Blackadar (1962). It should be noted that Zdunkowski and Barr find it necessary to make stringent assumptions, including a choice of u_*, when formulating their initial wind profile in order to obtain reasonable solutions to their momentum equations.

No allowance for gravitational settling of fog droplets is made in the Fisher-Caplan, Zdunkowski-Nielsen, and Zdunkowski-Barr models. In the Pilie and Brown-Roach models, a mean settling velocity is expressed as a function of liquid water content, obtained by (1) formulating a relationship between liquid water content and droplet size distribution, and (2) computing a mean droplet fall speed using Stokes' Law.

C. COMPARISON OF PREVIOUS FOG MODEL PREDICTIONS WITH OBSERVATIONS

Development of the nocturnal temperature profile is described in Geiger (1965). A ground-based inversion propagates upward, driven by the radiative heat loss at the ground. The cooling of the overlying atmosphere is the resultant of the divergence of the long-wave flux and the divergence of the turbulent flux of heat toward the sur-

face. All previous fog models generate a strong pre-fog inversion.

Tabulations of observed temperature profiles within fog are provided by Kolenkova (1971). When fog forms, a portion of the long-wave radiation emitted by the surface is absorbed by fog droplets and re-radiated back toward the surface, reducing the net surface long-wave flux. As the thickness and depth of the fog increases, cooling at the ground ceases. The fog top takes over as the effective radiating surface; as a result, the temperature profile in the lower part of the fog may become unstable, while the inversion persists above the fog top.

In the Fisher-Caplan model, fog radiative effects are ignored. When the externally specified turbulent exchange coefficient is used in this model, the ground based inversion continues to intensify during fog formation, as would be expected if fog were transparent to long-wave radiation. In the Fisher-Caplan model with internally generated exchange coefficients, the inversion weakens somewhat near the surface when the fog forms; this behavior is probably related to the release of large amounts of latent heat associated with unrealistically high liquid water contents.

In the Zdunkowski-Nielsen, Zdunkowski-Barr, Pilie, and Brown-Roach models, destabilization of the θ profile

takes place to varying extents with the model fogs. Computed values of long-wave flux divergence which may be unrealistically large result in intense inversions near the model fog top in the Zdunkowski-Nielsen and Brown-Roach models.

Maximum liquid water contents measured in fogs have been of the order of 0.2 g kg^{-1} (Eldridge, 1966; Pilie et al, 1972). Visibility in fog is a function not only of liquid water content, but also of droplet size distribution. Pilie et al. observed minimum visibilities of around 200 m, while Eldridge (1971) computes a visibility of 75 m for a "stable" fog with a liquid water content of 0.2 g kg^{-1}.

The Fisher-Caplan model predicts liquid water concentrations in excess of 2.0 g kg^{-1}. Since the surface temperature forcing in this model is independent of the presence of fog, significant post-saturation cooling takes place, resulting in excessive liquid water concentrations.

Maximum liquid water concentrations predicted by the Zdunkowski-Nielsen, Zdunkowski-Barr, Pilie, and Brown-Roach models generally fall between 0.3 and 0.6 g kg^{-1}. There is no clear explanation for the smaller, but still significant deviations from observed liquid water concentrations produced by these models.

The vertical extent of model fogs is affected by the formulation of K and by the inclusion or exclusion of

droplet settling. The effect of K is strikingly illustrated in the Fisher-Caplan model. The externally specified K profile results in a fog extending upward to a height of 400 m, while the use of the stability-dependent K profile limits the upward propagation of the forced surface cooling, and thus the fog depth, to around 15 m. The Zdunkowski-Nielsen and Zdunkowski-Barr model fogs reach heights of 100-200 m, while the Pilie and Brown-Roach models produce maximum fog heights of 10-50m. Fogs produced by the Zdunkowski-Nielsen and Zdunkowski-Barr models tend to "lift" a few hours after they first appear; i.e., liquid water concentrations decrease near the ground and increase at the fog top. This behavior may result from the lack of an expression for droplet settling in either of these models. Brown and Roach obtain a similar result by running their model without its droplet settling term.

Lala et al. present comparisons of model-predicted temperature, dew point, and time of fog onset with shelter-level observations. Although they are able to predict fog in two cases where fog was observed, their apparent success is based in large part on specification of the "right" time-dependent K profile and also on the questionable substitution of a later set of shelter-level observations for the initial shelter-level temperature and dew point reported at the time of the radiosonde.

Lala et al. isolate the effect of long-wave flux diver-

gence due to water vapor by running their model with and without this term for the same set of initial conditions. They find that significantly more shelter-level cooling--roughly 6°K over an 8-hour period--is predicted with the flux divergence included than without it. Similarly, they isolate the effect of dew formation by running the model with and without it on a "no-fog" case. With dew formation included, their model does not predict fog; without it, a model fog appears within 4 hours.

The most realistic features of previous models have been incorporated into the current model. The expression of turbulent exchange coefficients in the current model is a modification of that used by Pilie et al. Long-wave radiative transfer in the absence of fog is treated similarily to that in the Lala model; the treatment of long-wave radiation within fog is basically that of the Pilie model. Droplet settling is handled as in the Brown-Roach model.

A detailed discussion of all features of the current model is found in the next chapter.

CHAPTER III: DESCRIPTION OF THE MODEL

A. PROGNOSTIC EQUATIONS

The model consists of the following prognostic equations for potential temperature (θ), specific humidity (q), liquid water content (ℓ), and soil temperature (T_s).

$$\frac{\partial \theta}{\partial t} = \frac{\partial}{\partial z}\left(K \frac{\partial \theta}{\partial z}\right) - \frac{1}{c_p \rho} \frac{\partial F_N}{\partial z} + \frac{1}{c_p \rho} S_{LH} \qquad (3.1)$$

$$\frac{\partial q}{\partial t} = \frac{\partial}{\partial z}\left(K \frac{\partial q}{\partial z}\right) - S_p \qquad (3.2)$$

$$\frac{\partial \ell}{\partial t} = \frac{\partial}{\partial z}\left(K \frac{\partial \ell}{\partial z}\right) + S_p + \frac{\partial}{\partial z}(\bar{v}\ell) \qquad (3.3)$$

$$\frac{\partial T_s}{\partial t} = k_s \frac{\partial^2 T_s}{\partial z^2} \qquad (3.4)$$

where K is the turbulent exchange coefficient (assumed equal for the exchange of all atmospheric properties), k_s is the soil diffusivity, F_N is the net long-wave radiative flux (positive upwards), S_{LH} is the rate of latent heat gain or loss through condensation or evaporation, and S_p is the rate at which moisture condenses or evaporates, and $\bar{v}$ is the mean droplet fall speed.

Equations (3.1) and (3.4) are coupled by a <u>heat balance</u> equation at $z=0$:

$$F_{N_{z=0}} - \rho\, c_p\, K \left.\frac{\partial \theta}{\partial z}\right|_{z=0} - \rho\, L\, K \left.\frac{\partial q}{\partial z}\right|_{z=0} + \rho_s\, c_s\, k_s \left.\frac{\partial T_s}{\partial z}\right|_{z=0} = 0 \qquad (3.5)$$

Note that $T_s = \theta$ at $z=0$. ρ denotes atmospheric density, ρ_s denotes soil density, c_p denotes the specific heat of air at constant pressure, c_s denotes the specific heat of the

soil, and L denotes the latent heat of vaporization of water. Equation (3.5) states that the radiative heat loss from the surface is balanced by the sum of (a) the turbulent flux of sensible heat toward the surface from the atmosphere; (b) the turbulent flux of latent heat toward the surface from the atmosphere; and (c) the flux of sensible heat from the soil toward the surface.

The prognostic equations are solved upon a vertical grid which extends from the surface upward to a height of 472 m and downward to a soil depth of 0.72 m. There are 25 atmospheric grid levels and 15 soil grid levels. The first atmospheric grid level above the surface is set at a height of 1 m, the first soil grid level below the surface is set at a depth of 0.01 m. The spacing between grid levels increases as height or depth increases; the grid expansion ratio is 1.2 for both atmosphere and soil.

B. BOUNDARY CONDITIONS

As a lower boundary condition on heat, T_s is held constant throughout the model run at the lowest soil grid level. Diurnal variation of soil temperature at this level is negligible(Geiger, 1965).

Since soil moisture is not treated in the model, a lower boundary condition on moisture at z=0 is imposed. q is held constant at z=0 until surface cooling results

in saturation. In addition, the surface moisture flux, which appears in the latent heat term of (3.5), is held at zero until surface saturation is attained. Once the surface becomes saturated, q at the surface is equal to the saturation specific humidity at the surface temperature, and the no-flux condition on q is removed. This boundary condition allows removal of moisture from the model atmosphere through dew formation.

At the upper boundary of the model, θ and q are constrained to vary in a prescribed manner. For verification purposes, values of θ and q at the beginning and end of a model run are obtained for the uppermost atmospheric grid level by interpolating the 0000 GMT and 1200 GMT radiosonde data. It is assumed that θ varies sinusoidally at the model top with a period of 24 hours and a maximum at the beginning of the model run, while q at the model top is assumed to vary linearly with time.

C. INITIALIZATION OF THE MODEL

Initial values of θ and q are assigned to each atmospheric grid level by interpolating and extrapolating the temperature and relative humidity data from a radiosonde sounding. Before interpolating, the relevant levels of temperature are converted to θ via Poisson's equation

$$\theta = T\left(\frac{1000}{P}\right)^{0.286} \qquad \text{(P in mb.)} \qquad (3.6)$$

In (3.6), P denotes atmospheric pressure. Relative humidity is multiplied by the saturation mixing ratio as indicated on a pseudoadiabatic plot of the sounding to obtain the actual mixing ratio. To convert mixing ratio (m) to specific humidity, the approximation

$$q \simeq m\left(1 - \frac{m}{0.621p}\right) \tag{3.7}$$

with m and q in g kg^{-1} and P in mb, is used.

The sounding is interpolated logarithmically to obtain θ and q for grid levels lying between shelter level (1.5 m) and 50 m. Above 50 m, the sounding is interpolated linearly.

To obtain initial values of θ and q at z=1 m, data from the sounding are extrapolated logarithmically downward from shelter level. The initial value of θ at the surface is obtained by extrapolating the θ profile logarithmically downward to z=0.01 m and assigning this value to z=0 m, which Geiger (1965) gives as a representative roughness height for an airfield. The initial value of q at the surface is assumed to equal the initial value of q at z=1 m.

T_s must be initialized at each soil grid level. A three-layer initial soil temperature profile, schematically illustrated in Figure 3.1, is assumed. This profile is based on a set of soil temperature profile observations (Geiger, 1965). In the first layer below the surface,

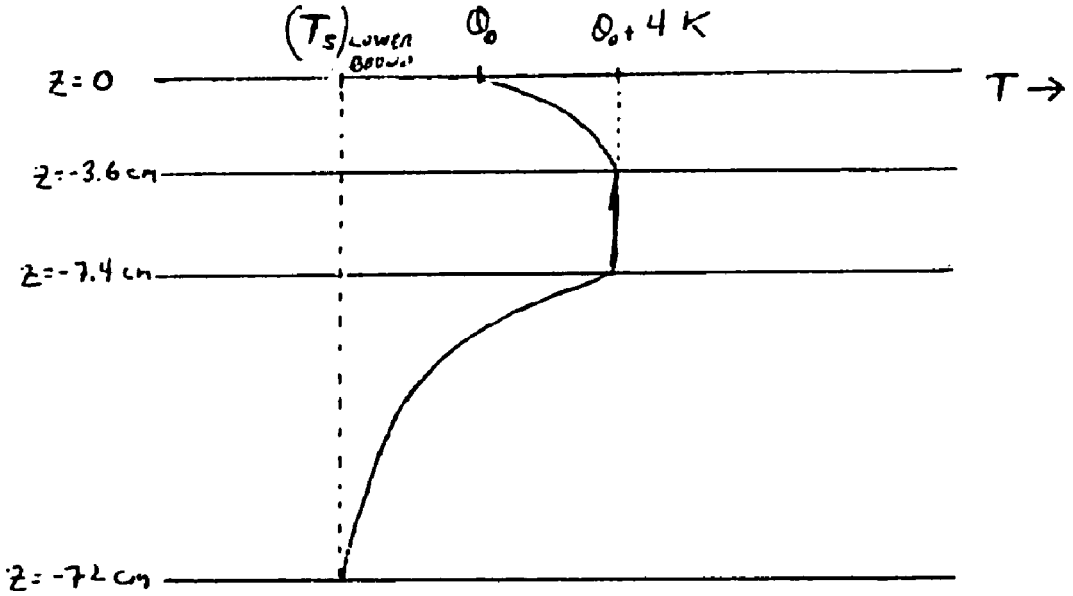


Fig. 3.1: Schematic diagram (not drawn to scale) of initial soil temperature profile

T_s increases logarithmically with depth to a maximum of $\theta_0 + 4$ K, where θ_0 is the surface temperature. In the middle layer, T_s is constant with depth. In the deepest layer, T_s decreases logarithmically with depth to its constant lower boundary level, which is set equal to the mean shelter level temperature for the 24 hours preceding the start of the model run. The boundary between layers 1 and 2 is set at a depth of 3.6 cm; the boundary between layers 2 and 3 at a depth of 7.4 cm.

D. FORMULATION OF EXCHANGE COEFFICIENT

The mean turbulent flux of an atmospheric property is parameterized by an exchange coefficient K multiplied by the vertical gradient of that property. If A represents the property being affected, then the mean flux of A is expressed $K_A(\partial A/\partial z)$. K has dimensions L^2T^{-1}; its magnitude represents the intensity of turbulent transfer.

The intensity of turbulent transfer is governed by a combination of shear stress and thermal stability. Since θ is a prognostic variable, thermal stability is internally generated by the model. The shear stress is externally specified in terms of a friction velocity, u_*, where

$$u_* \equiv (\tau/\rho)^{\frac{1}{2}} \tag{3.8}$$

in which τ is the shear stress and ρ is the air density.

Shear stress and stability information are combined

in each of two stability- dependent surface-layer wind profiles, from which an expression for K can be obtained through manipulation and substitution. The two profiles have in common the dimensional stability parameter known as the "Obukhov length"

$$L = \frac{u_*^3 \rho c_p T}{kg H} \tag{3.9}$$

where k is von Karman's constant (assumed to be 0.4), g is the acceleration of gravity, H is the turbulent flux of sensible heat (positive downward), and T is a scaling temperature (assumed in this model to be 285 K).

Pilie et al derive a K expression from the so-called KEYPS profile (Lumley and Panofsky, 1964)

$$S^4 - \frac{\gamma S^3}{L} = 1 \tag{3.10}$$

where

$$S \equiv \frac{kz}{u_*} \frac{\partial u}{\partial z} \tag{3.11}$$

is the non-dimensional wind shear, and γ is a constant, taken by Pilie et al to be 17. However, analysis of wind observations (Lumley and Panofsky, 1964; Businger, 1973) has shown that the Monin-Obukhov expression for non-dimensional wind shear

$$S = \phi\left(\frac{z}{L}\right) \tag{3.12}$$

fits observations taken under stable conditions more closely than does the KEYPS profile. In this model, the Monin-Obukhov expression is used as a basis for K under

stable conditions.

A Taylor expansion is usually performed on (3.12) about the point $(z/L)=0$, which corresponds to a neutral stratification. Thus

$$S \simeq 1 + \frac{\beta z}{L} \tag{3.13}$$

where β is a constant. According to Businger, the best fit to observed wind profiles is obtained with $\beta=4.7$.

The first step in the derivation of K from (3.13) is to introduce expressions for the fluxes of momentum and heat. The mean flux of momentum is dimensionally equivalent to the shear stress per unit density. By definition of the exchange coefficient for momentum and of u_*

$$F_m \equiv K_m \frac{\partial u}{\partial z} \equiv \tau/\rho \equiv u_*^2 \tag{3.14}$$

where F_m denotes the flux of momentum and K_m the exchange coefficient for momentum. Similarly

$$H \equiv \rho c_p K_H \frac{\partial \theta}{\partial z} \tag{3.15}$$

where H denotes the flux of sensible heat and K_H the exchange coefficient for heat.

Since $\partial u/\partial z$ is not a product of the model, it cannot appear in the final formulation of K. From (3.14) is obtained

$$\frac{\partial u}{\partial z} = \frac{u_*^2}{K_m} \tag{3.16}$$

which is substituted into (3.11) to obtain

$$S = \frac{ku_* z}{K_m} \tag{3.17}$$

Equating (3.13) and (3.17)

$$1 + \frac{\beta}{L} z = \frac{ku_* z}{K_m} \tag{3.18}$$

Equation (3.15) is substituted into the expression for L to obtain

$$L = \frac{u_*^3 T}{kgK_H (\partial\theta/\partial z)} \tag{3.19}$$

At this point, the assumption is made that $K_m=K_H=K$. Businger (1973) obtains from analysis of wind and temperature profile observations a value of 1.34 for the ratio K_H/K_m under neutral conditions. He notes that K_H/K_m approaches 1 as the atmosphere becomes more stable. For the purposes of the fog model, it is assumed that the turbulent transfer of all three atmospheric variables -- θ, q, and ℓ -- can be represented by the same value of K at a given time at a given level of the atmosphere.

With $K_m=K_H=K$, (3.19) can be substituted into (3.18)

$$1 + \frac{\beta z k g K (\partial\theta/\partial z)}{u_*^3 T} = \frac{ku_* z}{K} \tag{3.20}$$

The terms of (3.20) can then be arranged to form a quadratic in K

$$\beta z k g \frac{\partial\theta}{\partial z} K^2 + (u_*^3 T)K - ku_*^4 zT = 0 \tag{3.21}$$

which can be solved for K using the quadratic formula.

Although the quadratic formula yields two solutions, only one of them is positive. The relevant solution is

$$K = \frac{-u_*^3 T + (u_*^6 T^2 + 4\beta z^2 k^2 g(\partial\theta/\partial z) u_*^4 T)^{\frac{1}{2}}}{2\beta z k g(\partial\theta/\partial z)} \qquad (3.22)$$

When $\partial\theta/\partial z=0$, (3.20) reduces to

$$K = k u_* z \qquad (3.23)$$

When model fog is present, a moist adiabatic lapse rate is neutrally stable, and $\partial\theta/\partial z$ in the expression for K must be replaced by

$$\frac{\partial\theta_w}{\partial z} = \frac{\partial\theta}{\partial z} + (\Gamma_m - \Gamma) \qquad (3.24)$$

where θ_w is the wet-bulb potential temperature, Γ_m is the local moist adiabatic lapse rate, and Γ is the dry adiabatic lapse rate. Since model fogs are close to the surface, Γ_m can be approximated from the wet adiabats on a pseudoadiabatic chart, in °K m^{-1}, as

$$\Gamma_m = [0.6 + 0.03(293-\theta)]/\ 170 \qquad (3.25)$$

When $\partial\theta_w/\partial_z < 0$, Equation (3.22) is replaced by the expression for K derived by Pilie <u>et al</u>

$$K = \frac{kz}{\sqrt{2}}\left\{-\gamma\frac{g}{T}\frac{\partial\theta_w}{\partial z}(kz)^2 + \left[\left(\gamma\frac{g}{T}\frac{\partial\theta_w}{\partial z}(kz)^2\right)^2 + 4u_*^4\right]^{\frac{1}{2}}\right\}^{\frac{1}{2}} \qquad (3.26)$$

The expression derived for K is applied at each level of the model atmosphere. u_* is held constant with respect to both height and time. The validity of this approach is discussed below.

The layer in which shear stress is relatively constant with height extends upward only to about 20 m at night (Lumley and Panofsky, 1964). Above this layer, the wind profiles upon which Equations (3.22) and (3.25) are based may not be valid. Little is known about the magnitude of turbulent transfer above the surface layer. The fact that diurnal variations in θ of 5 K or more are observed at heights of the order of the fog model top indicates that K is significant at this level and, in the absence of further observational information, motivates the extension of (3.22) and (3.25) to the model top.

A second significant uncertainty rests in the assumption of time-independence for u_*. The nocturnal shear-stress measurements reported by Wyngaard (1975) show that u_* decreases sharply after sunset on clear nights.

Finally, the Monin-Obukhov profile may break down under conditions of extreme stability. The Richardson number

$$Ri = \frac{g}{\theta} \frac{(\partial\theta/\partial z)}{(\partial u/\partial z)^2} \qquad (3.27)$$

is generally used as a measure of the stability. Businger (1973) notes the existence of a "critical" value of Ri above which turbulent flow becomes laminar. Businger argues that because momentum cannot be transfered downward

through a laminar layer, the wind shear at the upper boundary of the layer increases until it drives Ri below its critical value, breaking up the laminar flow and producing a "burst" of turbulence. In effect, K under such conditions is assumed to represent the mean of many such turbulent "bursts".

E. TREATMENT OF LONG-WAVE RADIATION

The net surface long-wave flux in (3.5) and the long-wave flux divergence term in (3.1) are computed from the profiles of θ, q, and ℓ generated by the model. The assumptions made in computing these terms depend upon whether or not fog is present in the model atmosphere.

The net long-wave flux is the difference of the upward and downward fluxes. Symbolically

$$F_N = F_\uparrow - F_\downarrow \tag{3.28}$$

The surface is assumed to radiate as a black body at the temperature T_o $(=\theta_o)$ obtained by solving (3.5). Thus

$$F_\uparrow = \sigma T_o^4 \tag{3.29}$$

where σ is the Stefan-Boltzmann constant.

In the absence of fog, $F_\downarrow$ includes contributions from atmospheric water vapor and carbon-dioxide. The long-wave radiative properties of water vapor can be expressed by a flux emissivity ϵ. ϵ characterizes the contribution of the water vapor at one level to the long-wave

flux at another, and is a monotonically decreasing function of the amount of water vapor between the two levels. Water vapor emissivity has been tabulated by Staley and Jurica (1970). The analytical expression

$$\varepsilon = 0.59 \left(\frac{T_o}{T_w} \right)^{\frac{1}{4}} \left[1 - \frac{1}{2} \sum_{n=1}^{2} \frac{1}{1+A_n \tilde{w}^{\frac{1}{2}}} \right] \qquad (3.30)$$

has been derived from Staley and Jurica's emissivity tables by Ramanathan (1976). (3.30) defines the emissivity of a water vapor surface at a height z_w with respect to the long-wave flux at a reference level z_R. In (3.30), T_w is the temperature at z_w, T_o=293 K, A_1=19, A_2=3.5, and $\tilde{w}$ is the "effective" water vapor path length between z_R and z_w, in cm. $\tilde{w}$ is defined thus, in terms of q

$$\tilde{w} = \int_{z_R}^{z_w} \frac{P(z)}{P_o} \left(\frac{T_o}{T(z)} \right)^{\rho} q \, dz \qquad (3.31)$$

The temperature dependence of (3.30) is ignored for the purposes of this model.

The contribution of a water vapor "slab" to the downward flux at the surface is illustrated graphically in Figure 3.2. The slab in the diagram is assumed to have a mean temperature T_w. The amount of long-wave flux emitted from the top of the slab which reaches the surface without being absorbed is equal to $\varepsilon\sigma\bar{T}_w^4$, while the flux from the bottom of the slab reaching the surface is equal to $(\varepsilon+\Delta\varepsilon)\sigma\bar{T}_w^4$. Thus the net contribution of the slab to

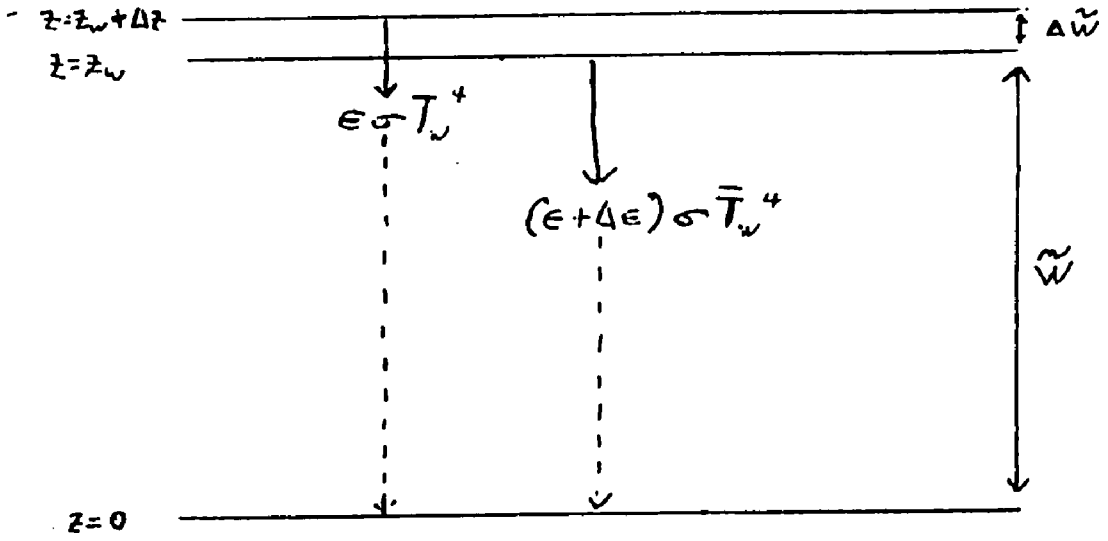


Fig. 3.2: Contribution of a water vapor slab to the downward flux of long-wave radiation at the surface

$F_{\downarrow}$ at the surface is $(\Delta\varepsilon)\ \bar{T}_w^4$, which for $\Delta\tilde{w} < \tilde{w}$ can be approximated as

$$F_{\downarrow} = \sigma T^4 \left(\frac{d\varepsilon}{d\tilde{w}}\right)_{\tilde{w}} \Delta\tilde{w} \tag{3.32}$$

The total contribution of atmospheric water vapor to $F_{\downarrow}$ is computed by summing all such slabs. Thus

$$(F_{\downarrow})_{H_2O} = \sum_i \sigma \bar{T}_i^4 \left(\frac{d\varepsilon}{d\tilde{w}}\right)_{\tilde{w}_i} \Delta\tilde{w}_i \tag{3.33}$$

The contribution of CO_2 to $F_{\downarrow}$ is approximated by adding $0.184\sigma T_o^4$ to (3.33) (Haltiner and Martin, 1957).

The temperature change resulting from the divergence of the net long-wave flux due to water vapor is computed by the method of Brooks (1950). Atwater (1966) compared several methods of computing long-wave flux and flux divergence near the surface. In the nocturnal case, the results were not significantly different from one another. The Brooks method was chosen for this model because it is the most economical.

Brooks bypasses the direct computation of net flux at levels above the surface by deriving an equation for radiative temperature change at a given level

$$\frac{dT}{dt}(z_R) = \frac{g(z_R)}{c_p}\left(\frac{P(z_R)}{1000}\right)^{\frac{1}{2}}\left[\sum_{i=1}^{n} A_i (\sigma \bar{T}_i^4)\left(\frac{d\varepsilon}{d\tilde{w}}\right)_{\tilde{w}_i} + \sigma T^4 \left(\frac{\partial\varepsilon}{\partial\tilde{w}}\right)_{\tilde{w}_T} + \sum_{j=1}^{m} A_j (\sigma \bar{T}_j^4)\left(\frac{d\varepsilon}{d\tilde{w}}\right)_{\tilde{w}_j}\right] \tag{3.34}$$

The indices i and j refer to water vapor slabs above and below z_R, respectively. $P(z_R)$ is expressed in millibars. The middle term in the brackets is evaluated at a level assumed to be the top of the water vapor atmosphere.

Evaluation of (3.33) using radiosonde data shows that approximately 12% of the downward long-wave flux at the surface is contributed by water vapor above the model top. For this reason, significant levels of T and q between the model top and the 400 mb level are included when evaluating (3.33) and (3.34). These values are obtained from the sounding used to initialize the model, and are held constant throughout the model run.

When fog is present in the model atmosphere, long-wave radiation is absorbed and scattered by fog droplets. The degree to which a fog interacts with the long-wave flux depends upon the number and size of the droplets, information which the model does not predict. Pilie et al (1972) parameterize fog absorption of long-wave radiation in terms of the prognostic variable ℓ, utilizing a mean mass absorption coefficient k_w. Scattering by fog droplets is ignored by Pilie et al. They also assert that k_w is valid as long as the proportion of fog droplets with radii exceeding 10 μm is small.

k_w is obtained by performing radiative transfer calculations for a representative droplet size spectrum. Pilie et al compute a k_w of 0.15 $m^2 g^{-1}$, while Kondratyev

(1965) suggests a value of 0.06 $m^2 g^{-1}$. The value of Pilie et al is used in this model.

The net long-wave flux at a given level in the fog is given by

$$F_w(z) = F_{NT} \exp\left[-1.6k_w \rho \int_z^{z_T} \ell(z')\, dz'\right] \qquad (3.35)$$

where F_{NT} is the net long-wave flux at the fog top. It is assumed that the fog top radiates as a black body; F_{NT} is computed exactly as F_N is computed at the surface in the absence of fog. The factor 1.6 accounts for the angular dependence of the radiation field.

Equation (3.35) is differentiated with respect to z to obtain

$$\frac{\partial F_N}{\partial z} = 1.6k_w \rho \ell(z) \exp\left[-1.6k_w \rho \int_z^{z_T} \ell(z')\, dz'\right] \qquad (3.36)$$

the divergence of the net long-wave flux within the fog. For all levels at which fog exists in the model, (3.36) is substituted into (3.1), in lieu of (3.31). Above the fog top, (3.34) is evaluated at each level with the fog top replacing the surface; this is consonant with the assumption of the fog top as a black body.

The effect of water vapor within the fog is thus ignored. Since liquid water absorbs very strongly in the frequency range where terrestrial long-wave radiation is most intense, while water vapor is virtually transparent at these frequencies, it seems justifiable to assume that

the effect of liquid water predominates in the divergence of long-wave flux within fog.

F. SATURATION ADJUSTMENTS

The effects of phase changes of water in the model atmosphere are represented by S_{LH}, which appears in equation (3.1), and S_p, which appears in equations (3.2) and (3.3). Condensation takes place when θ and q become such that the model atmosphere is supersaturated. Conversely, evaporation takes place when liquid water is present and the model atmosphere becomes subsaturated.

A two-step diagnostic procedure formulated by McDonald (1963) is performed whenever condensation or evaporation is required by the combination of θ, q, and ℓ at a given level of the model. The procedure is based upon the Clausius-Clapeyron equation for saturation vapor pressure. The case of condensation is discussed below.

First, the temperature is adjusted to account for latent heat release. θ is converted to actual temperature by (3.6), $\bar{q}$ to vapor pressure by means of the approximation

$$e = q\left(\frac{P}{621}\right) \tag{3.37}$$

In both (3.6) and (3.37), P in millibars in approximated as a function of height by

$$P = 1000 - \frac{z}{8.5} \quad (z \text{ in meters}) \tag{3.38}$$

If the temperature and vapor pressure before adjustment are represented by T_o and e_o, and e_{so} is the saturation vapor pressure at T_o, then

$$T = T_o + A(e_o - e_{so}) \tag{3.39}$$

where

$$A = (\varepsilon L R T_o^2)/(c_p P R T_o^2 + \varepsilon^2 L^2 e_{so}) \tag{3.40}$$

In (3.40), R is the universal gas constant, ε=0.621, and L is the latent heat of vaporization of water. L is a function of temperature, given by

$$L(T) = 597.3 - 0.566 \quad (T-273) \text{ cal } g^{-1} \tag{3.41}$$

Once T is obtained, the vapor pressure is reduced by the following relation

$$e = e_o - (c_p P/\varepsilon L)(T-T_o) \tag{3.42}$$

so that the supersaturation is eliminated. The adjusted liquid water concentration is then given by

$$\ell = \ell_o + (e_o - e) \tag{3.43}$$

It should be noted that the adjustments in the case of evaporation can be no greater than those required to evaporate all liquid water present. If evaluation of (3.43) yields a negative l, then (3.41) and (3.42) are re-evaluated so that

$$T = T_o - A\ell_o \tag{3.44}$$

$$e = e_o + \ell_o \tag{3.45}$$

G. PARAMETERIZATION OF DROPLET SETTLING

The flux of liquid water due to the gravitational settling of fog droplets is defined by

$$G \equiv \bar{V}\,\ell \tag{3.46}$$

where $\bar{V}$ is the mean droplet fall speed. The fall speed of an individual droplet of radius r is given by Stokes' Law (Byers, 1965)

$$V(r) = \frac{2}{9}\frac{\rho_L}{\eta} g\, r \tag{3.47}$$

where ρ_L is the density of water, η is the viscosity of air, and g is the acceleration of gravity. For a given droplet size distribution

$$\ell = \frac{4}{3}\pi\rho_L \int_0^\infty N(r) r^3\, dr \tag{3.48}$$

$$\bar{V} = \frac{\int_0^\infty N(r)\, V(r)\, r^3\, dr}{\int_0^\infty N(r)\, r^3\, dr} \tag{3.49}$$

From experimentally determined droplet size distributions, Brown and Roach (1976) computed both ℓ and $\bar{V}$, obtaining the relationship

$$\bar{V} = s\,\ell \tag{3.50}$$

where s is a constant. For ℓ in g kg^{-1} and $\bar{V}$ in cm sec^{-1}, Brown and Roach determined the value of s to be 6.25. Equation (3.50) is substituted for $\bar{V}$ in Equation (3.3).

H. NUMERICAL PROCEDURE

The prognostic equations (3.1) through (3.4) are expressed in numerical form and integrated with respect to time. Equation (3.5), the surface heat balance equation is diagnostically solved in each time step.

Within a given time step, each term in the prognostic equations is integrated separately, with the exception of the turbulent exchange and droplet settling terms in (3.3), which are integrated simultaneously.

The turbulent exchange terms in equations (3.1) and (3.2) are integrated implicitly, utilizing an algorithm developed by Fisher and Caplan (1963) for application to one-dimensional model grid with variable spacing and variable exchange coefficients. Fisher and Caplan expand the equation

$$\frac{\partial Q}{\partial t} = \frac{\partial}{\partial z}\left(K\frac{\partial Q}{\partial z}\right) \tag{3.51}$$

into finite difference form and show that it can be expressed as a series of equations

$$Q_R = E_R Q_{k+1} + F_k \tag{3.52}$$

where the subscript k denotes a grid level. Since Q_o, the lower boundary value of Q, is known from the previous time step

$$E_o = 0 \tag{3.53}$$

$$F_o = Q_o \tag{3.54}$$

satisfies (3.52). Fisher and Caplan then show that

$$E_k = f(E_{K-1}) \tag{3.55}$$

$$F_k = g(E_{k-1}, F_{k-1}) \tag{3.56}$$

where f and g contain values of K and Q from the previous time step, along with grid spacing and time step information. Thus, starting from known surface values, the grid can be scanned upward to obtain the E_k and F_k. Starting from the known upper boundary values, the grid is then scanned downward to obtain new values of the variable Q.

A similar algorithm can be derived for the implicit integration of the turbulent exchange and droplet settling terms in (3.3). If k_s is substituted for K, the Fisher-Caplan algorithm can be applied to the integration of (3.4) as well.

When no fog is present in the model atmosphere, equations (3.29) and (3.33) are evaluated at the surface to obtain the net surface long-wave flux. When fog is present, (3.29) and (3.33) are evaluated at the fog top; the net surface flux is then obtained from (3.35).

Once the net surface long-wave flux has been computed, the surface heat balance, equation (3.5), can be solved for θ_o. In finite difference form, (3.5) becomes

$$\sigma\theta_o^4 - F_\downarrow - \rho c_p \frac{K_1}{z}\frac{(\theta_1-\theta_o)}{z_1} - \rho_L \frac{K_1}{z}\frac{(q_1-q_0)}{z_1} + \rho_s c_s k_s \frac{(\theta_o - T_s(-1))}{z_s(-1)} = 0 \tag{3.57}$$

Newton's method is used to solve (3.57) for θ_o. Note that F_N is not directly computed in the presence of model fog. However, if the upward component of F_N obtained from (3.35) is assumed to be σT^4, the use of Newton's method to solve (3.57) within fog is valid.

The rate of radiative temperature change at each level is then determined by solution of (3.34) at levels where no fog is present and (3.36) within fog. The long-wave flux divergence term in (3.1) is integrated by multiplying the diagnostically determined rate of change by the time step length.

At this point, temperature and vapor pressure are computed from θ and q at each level, and relative humidity is evaluated. If the vapor pressure at any level exceeds the saturation value, thermodynamic adjustments are made by solution of (3.39), (3.42), and (3.43). Temperature and vapor pressure are then converted back to θ and q.

The final operation within the time step is the evaluation of K at each level of the model atmosphere, utilizing (3.22) when the atmosphere is stable and (3.26) when it is unstable.

Fisher and Caplan assert that their implicit integration scheme for the turbulent exchange terms is numerically stable, but that oscillations about the correct solution may appear if the quantity $\Delta t K/(\Delta z)^2$, where Δt is the time step length and Δz is the grid spacing, be-

comes too large. It is assumed that the combined integration in this model of the turbulent exchange and droplet settling terms in equation (3.3) is likewise stable, and that the rest of the terms in the model equations do not affect numerical stability.

A time step of 150 sec is sufficiently small to prevent noticeable oscillations in the prognostic variables in the absence of model fog. When model fog is present, the time step is reduced to 10 sec, as suggested by Pilie et al (1972), to compensate for increased values of K within the fog.

Oscillations in ℓ begin to appear when ℓ exceeds about 0.5 g kg^{-1}. The amplitude of these oscillation is roughly half the value of ℓ. Further reduction of the time step, to 5 sec, does not remove the oscillations. Since 0.5 g kg^{-1} is an unrealistically high value of ℓ, generated by apparent shortcomings in the modelling of the fog radiative processes, it was decided to halt the model run whenever the oscillations appeared; the numerical cause of the oscillations was not pursued further.

CHAPTER IV: VERIFICATION OF THE MODEL

A. SELECTION OF CASES

Eleven cases in which nocturnal fog formed at Flint, Michigan during the period 1957-63 were selected for model verification. The following criteria were used in selecting these cases: (1) a case had to include at least one hourly observation of fog or ground fog with visibility equal to or less than 1/2 mile; (2) the mean cloud cover during the period between sunset and fog formation could not exceed 3/10; and (3) the surface synoptic pattern had to show negligible temperature or moisture advection. Criteria (2) and (3) were necessary because the effects of cloud cover and advection are not accounted for in the model.

Initial conditions for each case were obtained from the 0000 GMT (1900 EST) Flint radiosonde data. It was desired that the model be initialized close to sunset in order that (1) the development of the pre-fog inversion would be modeled as completely as possible; and (2) incoming solar radiation need not be taken into account. Therefore, the selection of cases was limited to the months of September and October, during which sunset occurs within one hour of 1815 EST at Flint.

B. VERIFICATION PROCEDURE

In each case, the model was run until model fog ap-

peared, or for 12 hours if model fog failed to form. The onset of model fog was defined as the time at which the liquid water concentration at z=1 m first exceeded 0.01 g kg^{-1}. In two of the selected cases, an attempt was made to simulate fog developement by running the model beyond the onset of fog.

For all model runs, the following input values were supplied:

$$k_s = 3 \times 10^{-7}\ m^2 sec^{-1}$$
$$\rho_s = 1000\ kg\ m^{-3}$$
$$c_s = 500\ cal\ kg^{-1}\ °K^{-1}$$
$$u_* = 10\ cm\ sec^{-1}$$

Diffusivity, (k_s) density, (ρ_s) and specific heat values (c_s) for the soil are those specified in the fog model of Pilie et al (1972) and are representative of a soil of average thermal characteristics (Geiger, 1965). The value of u_* specified here should be viewed as an arbitrary constant whose use in the computation of the exchange coefficient K produced credible model results. When substituted into the logarithmic wind laws, a u_* of 10 cm sec^{-1} taken together with a roughness height of 1 cm yields a wind speed of approximately 1.7 m sec^{-1} at a height of 10 m, a wind speed comparable to early evening observations in most of the fog cases.

The abundance of available condensation nuclei was accounted for in a crude way by allowing condensation to

take place in the model atmosphere when the relative humidity exceeded 97%, rather than 100%. At temperatures characteristic of fog formation in the selected cases, a relative humidity of 97% corresponds to a dew point depression of roughly 0.5 K; in 9 of the 11 fog cases considered, a dew point depression of 1° F (0.56 K) or greater was observed concurrently with the initial fog observation. It was assumed that the reduced relative humidity did not apply to dew formation.

C. RESULTS OF PRE-FOG SIMULATIONS

Relevant information concerning each of the Flint fog cases selected for model verification is given in Table 4.1. The 1815 EST dew point depression is obtained from the shelter-level radiosonde data. The mean pre-fog wind speed is the mean of the hourly wind speed observations between 1900 EST and the time of the first fog observation. Note that in 7 of the 11 cases the first fog observation is associated with a visibility of 1 1/2 to 6 miles; in 4 cases, two or more hours elapse between the first fog observation and the first visibility observation of 1/2 mile or less.

Empirical schemes for forecasting nocturnal fog from routinely obtained surface data are usually based upon dew point depression and wind speed at sunset (e.g., George, 1950). The data displayed in Table 4.1 show that

TABLE 4.1

RELEVANT DATA FOR SELECTED FLINT FOG CASES

CASE NO.	DATES	INITIAL DEW PT DEPR. (°C)	MEAN PRE-FOG WIND SPD (MPH)	HOUR OF FIRST F OR GF (EST)	VIS AT FIRST F OR GF OBSERVATION (MI)	HOUR OF FIRST VIS≤1/2 MI (EST)
1	8-9 SEP 1957	10.4	1.3	0200	1 1/2	0500
2	18-19 SEP 1958	8.1	0.8	0500	2	0600
3	20-21 SEP 1960	2.9	0.0	2100	1/2	2100
4	9-10 OCT 1960	5.8	1.3	0300	1/2	0300
5	11-12 OCT 1960	7.4	3.3	0100	6	0200
6	17-18 SEP 1961	7.5	5.8	0600	1/2	0600
7	7-8 OCT 1961	6.5	6.3	0400	2	0500
8	5-6 OCT 1962	3.1	4.0	2000	5	0100
9	6-7 OCT 1962	3.7	0.0	0000	2	0700
10	15-16 SEP 1963	7.5	2.8	0300	5	0600
11	12-13 OCT 1963	6.9	0.2	0400	5	0500

small dew point depressions at sunset are generally associated with early fog formation. However, the relationship between the mean wind speed and fog onset time is less clear.

Figures 4.1-4.11 compare temperatures and dew points computed from θ and q at the 1 m level of the model with Flint hourly observations from each of the cases considered. Table 4.2 is a comparison of model-predicted and observed fog onset times. In Figures 4.1-4.11, Table 4.2, and in the following discussion, all model times cited are referenced to 1815 EST, the assumed release time of the 0000 GMT radiosonde.

The observed appearance of fog was verified by the model in 8 of the 11 cases. In all cases where the model predicted fog, model fog onset times were within two hours of those actually observed.

However, model success in predicting fog onset was not necessarily associated with similar success in verifying observed temperatures and dew points. Cases 2 and 11 exemplify this point. In case 2, the agreement between model predictions and observations is excellent for both temperature and dew point, yet the model does not verify the observed fog. On the other hand, in case 11 model and observed fog onset times differ by only 0.41 hr, yet model temperature and dew point differ from observations

TABLE 4.2

COMPARISON OF MODEL AND OBSERVED
FOG ONSET TIMES

CASE	MODEL FOG ONSET (HOURS AFTER 1815 EST)	OBSERVED FOG ONSET
1	NONE	7.75
2	NONE	8.75
3	2.78	2.75
4	9.78	8.75
5	NONE	6.75
6	10.07	11.75
7	8.91	9.75
8	3.17	1.75
9	5.07	5.75
10	8.77	8.75
11	10.16	9.75

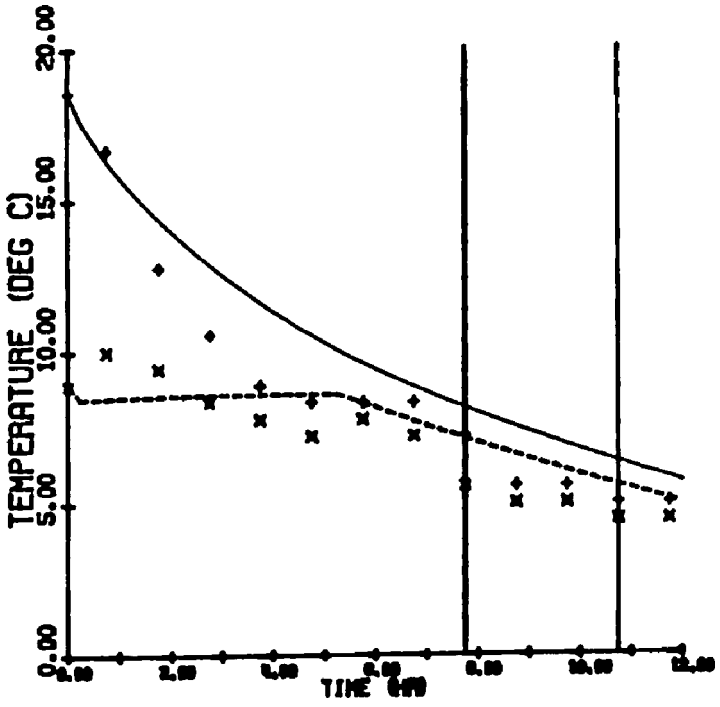


Fig. 4.1: Comparison of model-generated temperature and dew point with Flint hourly observations for case 1. (——): model temperature; (---): model dew point; (+): observed temperature; (×): observed dew point. Time is referenced to 1815 EST. The first vertical line denotes the initial F or GF observation. The second denotes the initial observation in which visibility was 1/2 mi. If only one vertical line is present, the two coincide.

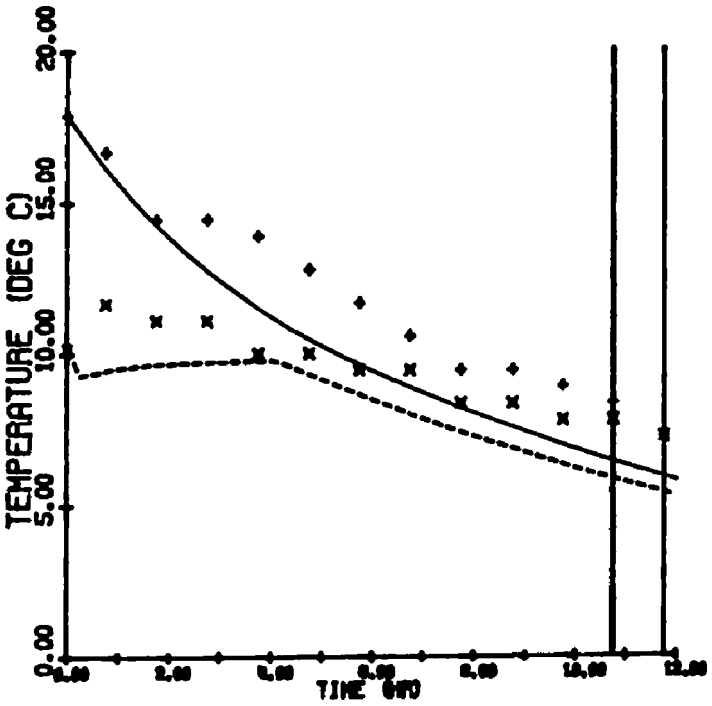


Fig. 4.2: As in Fig. 4.1, for case 2

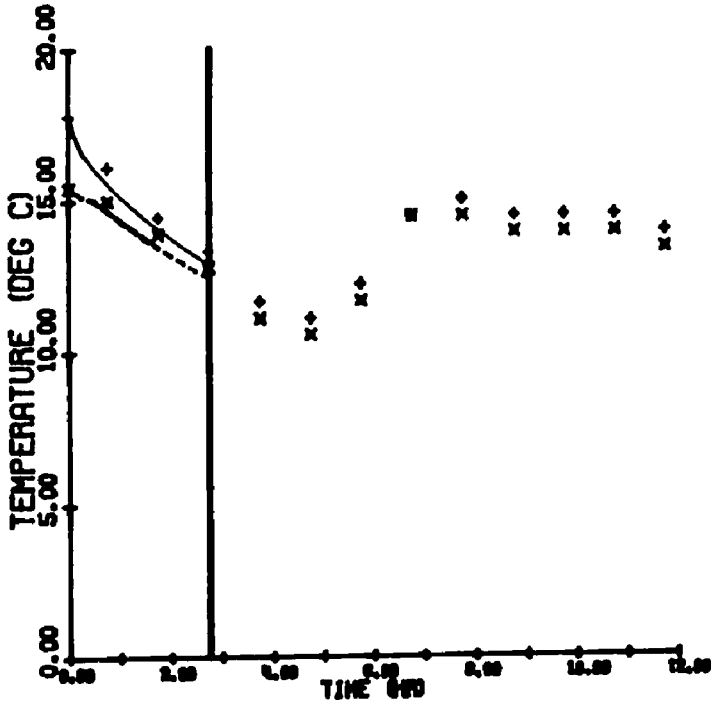


Fig. 4.3: As in Fig. 4.1, for case 3

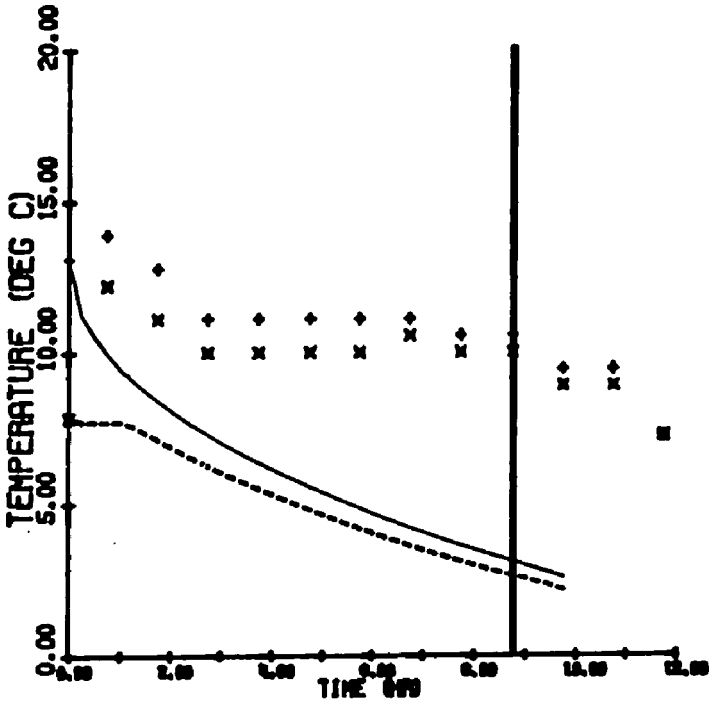


Fig. 4.4: As in Fig. 4.1, for case 4

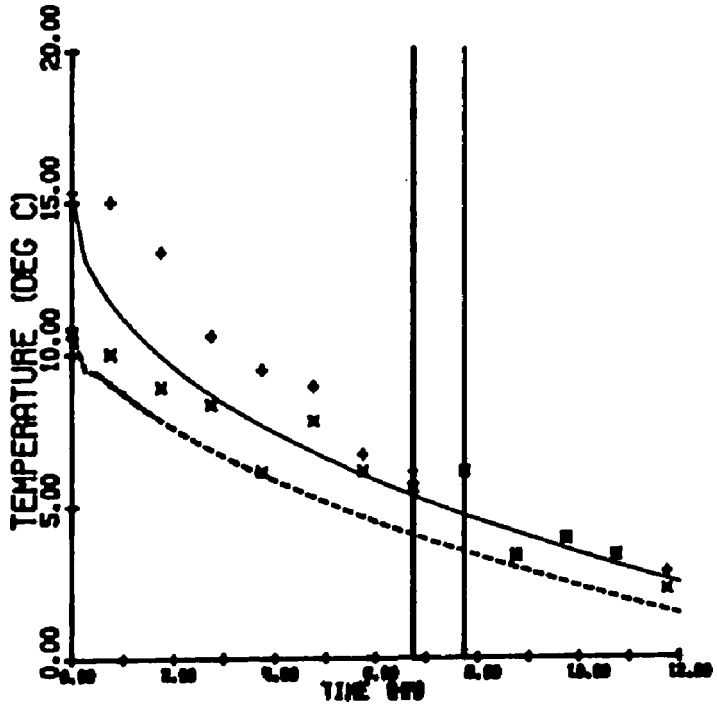


Fig. 4.5: As in Fig. 4.1, for case 5

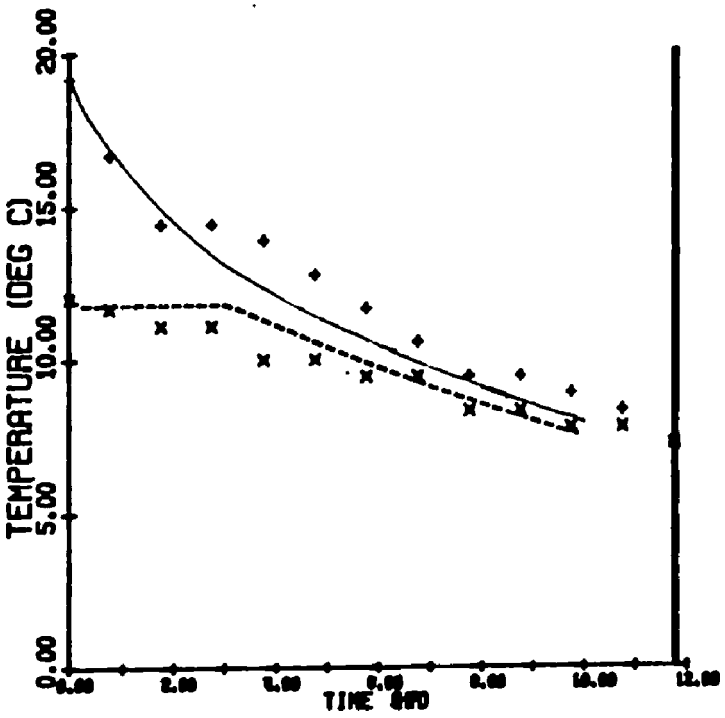


Fig. 4.6: As in Fig. 4.1, for case 6

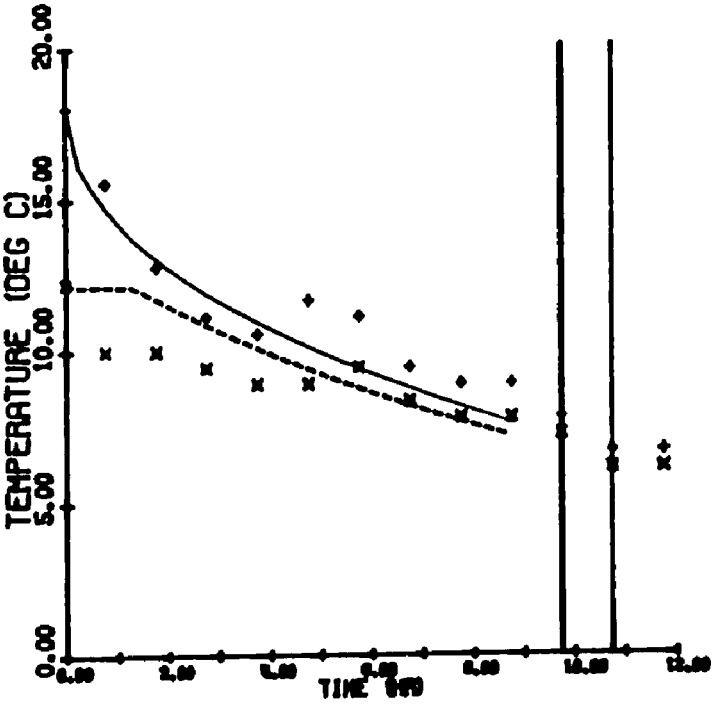


Fig. 4.7: As in Fig. 4.1, for case 7

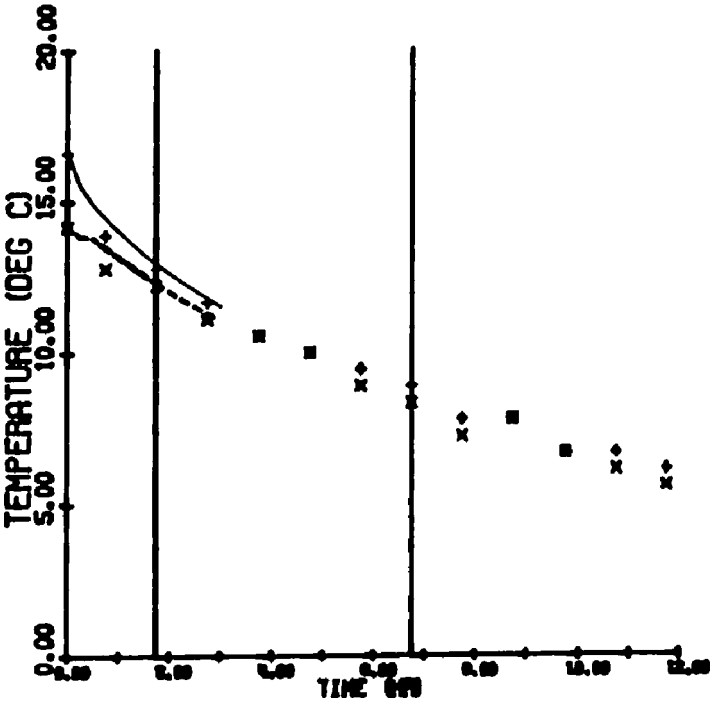


Fig. 4.8: As in Fig. 4.1, for case 8

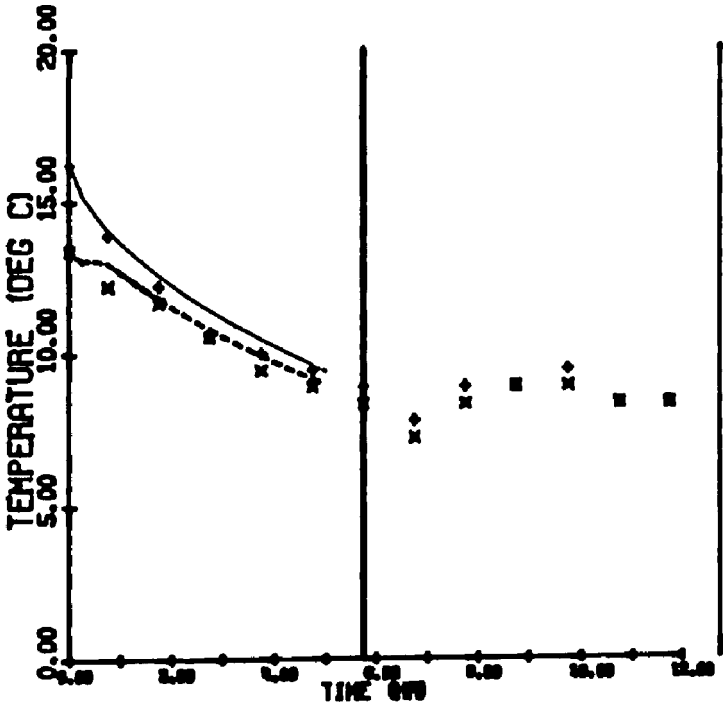


Fig. 4.9: As in Fig. 4.1, for case 9

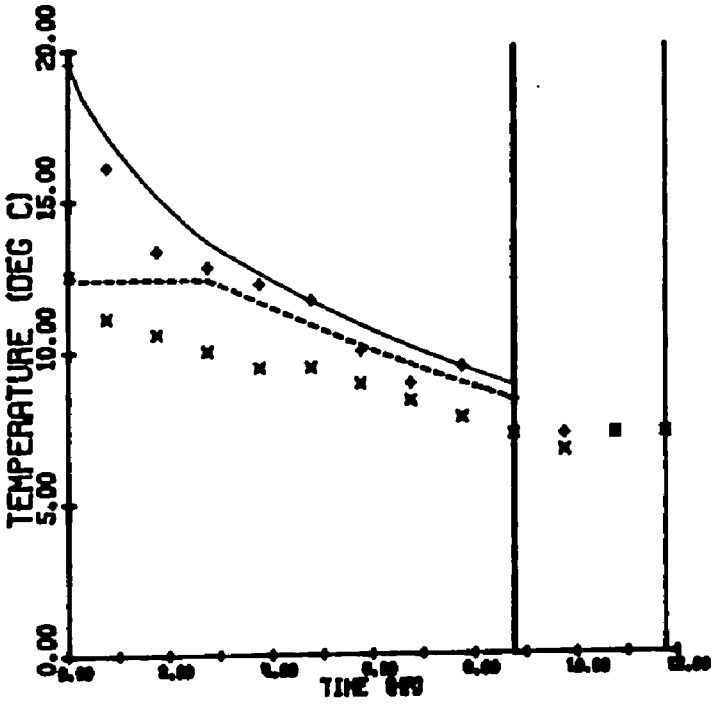


Fig. 4.10: As in Fig. 4.1, for case 10

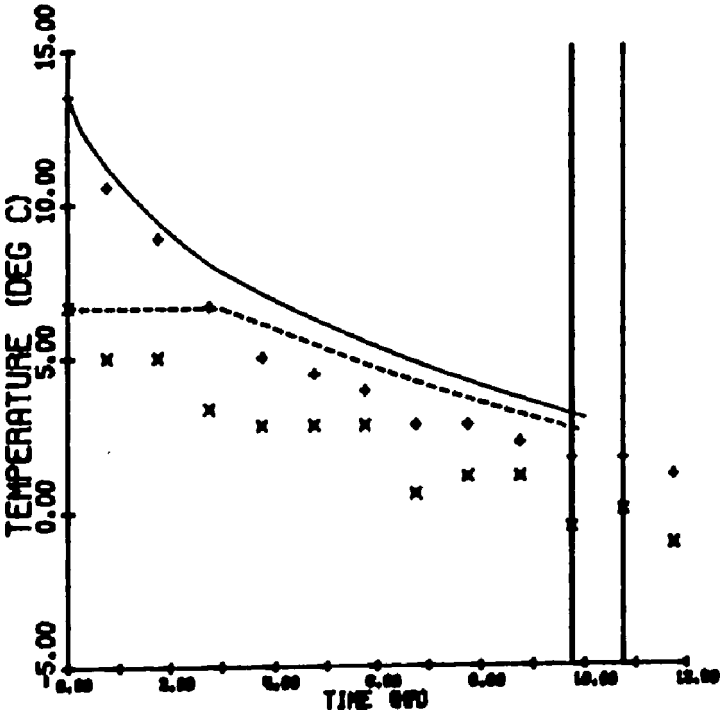


Fig. 4.11: As in Fig. 4.1, for case 11

at the time of observed fog onset (0400 EST, or t=9.75 hr) by 1.3°C and 3.2°C respectively. The successful verification of fog onset time in case 11 must be viewed as coincidental.

The model-predicted dew point patterns reflect the initial and lower boundary conditions placed upon q. Three distinct features can be seen in the plots of model dew point against time: (1) a slight drop in dew point during the first 15 minutes of model operation; (2) a period of relatively constant dew point; and (3) a nearly parallel decrease of temperature and dew point, with model fog forming if the two curves converge sufficiently. Case 6 (Fig. 4.6), which clearly exhibits each of these features, will be used as an example for discussion.

Figure 4.12 shows the model-generated profiles of q at t=0, t=1 hr, t=3 hr, and t=6 hr. It can be seen from the profile at t=0 that the initial condition requiring q at z=0 to equal q at z=1 m results in an inflection point at z=1 m. Turbulent exchange acts to remove this inflection point, producing a drop in q at z=1 m (and thus in the 1 m dew point) at the start of the model run.

The flat portion of the 1 m dew point curve results from the lower boundary condition imposed on q. q remains constant at z=0 from the start of the model run until the ground cools to saturation; the dew point at z=1 m thus remains relatively constant during this period. In model

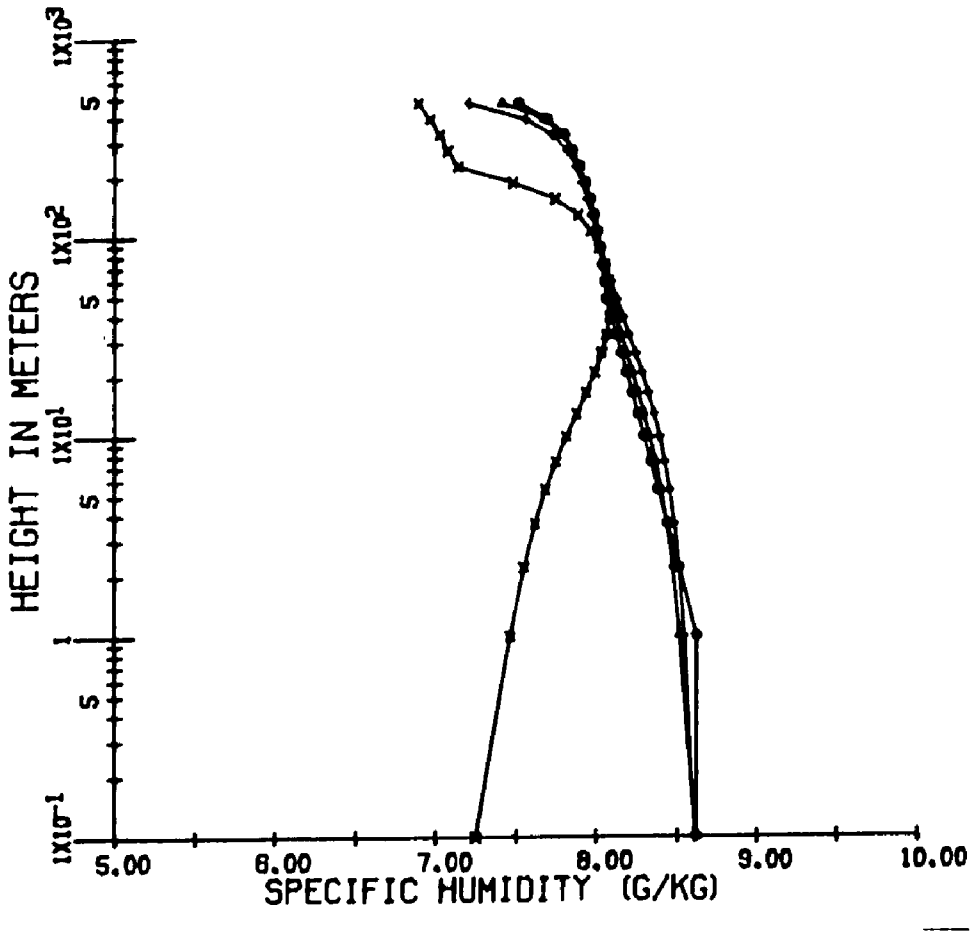


Fig. 4.12: Model-generated profiles of specific humidity for case 6. (—●—): t=0; (—▲—): t=1 hr; (—+—): t=3 hr; (—*—): t=6 hr.

runs where the initial dew point depression is small (cases 3, 8, and 9), surface saturation is reached very early in the model run and this feature is not apparent in the model output.

After saturation has been attained at z=0, further surface cooling reduces q as dew is formed. A turbulent flux of moisture, directed from the atmosphere toward the surface, develops. As this flux removes moisture from the model column, the dew point at z=1 m decreases.

As can be seen in Figures 4.1-4.11, observed behavior of the low-level dew point is highly variable, especially in the first few hours after sunset. Initial and lower boundary conditions imposed upon moisture in the model take into account neither the wetness of the soil nor the transfer of moisture between soil and atmosphere, both of which may vary from case to case and may influence the dew point at shelter level.

The greatest source of model error in replicating observed temperature and dew point lies in the inability of such a simple model to account for transient physical processes such as sub-synoptic advection, vertical motion, and aerosol-induced long-wave flux divergence. Such processes are very likely responsible for hour-to-hour changes in the sign of the observed temperature and dew point tendencies. In case 2, for example, a rise of 1°F in dew point was observed in the hour before fog onset, while in case 5, a

dew point rise of 3°F occured between 2200 and 2300 EST, with fog first observed at 0100 EST. Failure to predict these dew point rises may be related to the failure of the model to verify observed fogs in the two cases.

D. RESULTS OF FOG DEVELOPMENT SIMULATIONS

Attempts to simulate fog growth and development were made for cases 3 and 10. Case 3 exemplifies deep fog, while case 10 is representative of ground fog.

Hourly observations of visibility, visibility obstruction, temperature, dew point, wind direction, and wind speed for case 3 are shown in Table 4.3. Ground fog is first observed at 2100 EST, fog at 2300 EST. The minimum observed visibility, 1/16 mile, occurs at 0000 EST, after which fog persists, though with increasingly greater visibilities, until 0800 EST.

As evidenced by the temperature rise of 7°F observed between 2300 and 0200 EST, fog in this case apparently grew to sufficient depth to reduce net surface radiative heat loss to a value smaller than that of the combined fluxes of sensible heat toward the surface from the atmosphere and soil. The temperature rise may in turn have been responsible for the thinning of the fog after 0000 EST. The appearance of a wind at 0000 EST, after six hours of observed calm, is probably related to destabilization resulting from the surface warming.

Fog was formed by the model in case 3 after 2.78

TABLE 4.3

HOURLY OBSERVATIONS AT FLINT
20-21 SEP 1960

HOUR (EST)	VIS (MI)	OBSTR	TEMP (°F)	DEW PT	WIND DIR	WIND SPD (MPH)
1800	10		66	58	CALM	
1900	6	H	61	59	CALM	
2000	6	H	58	57	CALM	
2100	1/2	GF	56	55	CALM	
2200	1/2	GF	53	52	CALM	
2300	1/8	F	52	51	CALM	
0000	1/16	F	54	53	E	5
0100	1/2	F	58	58	E	6
0200	1 1/2	F	59	58	E	7
0300	2	F	58	57	E	5
0400	2	F	58	57	ESE	6
0500	2	F	58	57	E	4
0600	2	F	57	56	SE	4
0700	1	F	57	56	ESE	5
0800	3	F	57	56	E	7

hours, in virtual agreement with observations. Large oscillations in model liquid water concentration, probably related to the exaggeration of this variable by the model, forced a halt to the model run after 6 hours.

Observed temperature and dew point are compared with model-generated 1 m temperature and dew point in Fig. 4.13. Figures 4.14 and 4.15 show profiles of θ and K at the beginning of the model run and at t=2.75 hr, just before model fog onset. Figures 4.16, 4.17 and 4.18 show profiles of θ, K, and ℓ during the period of fog development, while Figure 4.19 gives the liquid water concentration at z=1 m as a function of time.

The model faithfully simulates observations during the ground fog stage. Liquid water is confined to the first level of the model atmosphere until t=4 hr, consistent with the 2100 and 2200 EST ground fog observations. At t=3.75 hr, the model-predicted liquid water concentration is 0.038 g kg^{-1}. According to the relationship of Eldridge (1971), this corresponds to a visibility of about 230 m, comparing favorably to the observed 2200 EST visibility of 1/8 mile. Model temperature and dew point at z=1 m are consistent with both the 2100 and 2200 EST observations.

However, model simulation of the upward development of the fog after 2200 EST is less successful. Model fog first appears above the 1 - m level at t=4 hr, growing to

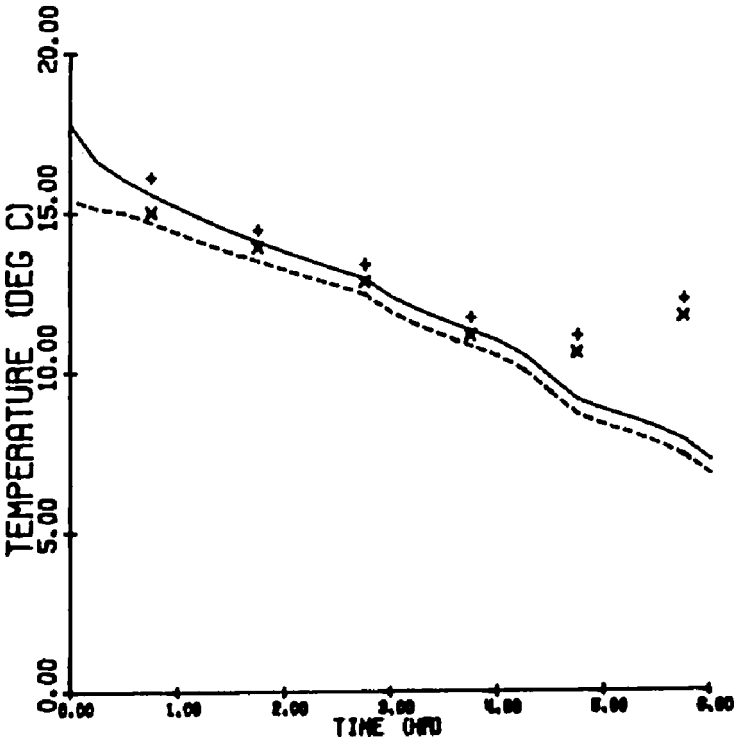


Fig. 4.13: Comparison of model-generated temperature and dew point with Flint hourly observations for both pre-fog and post-fog periods, case 3. Legend as in Figure 4.1.

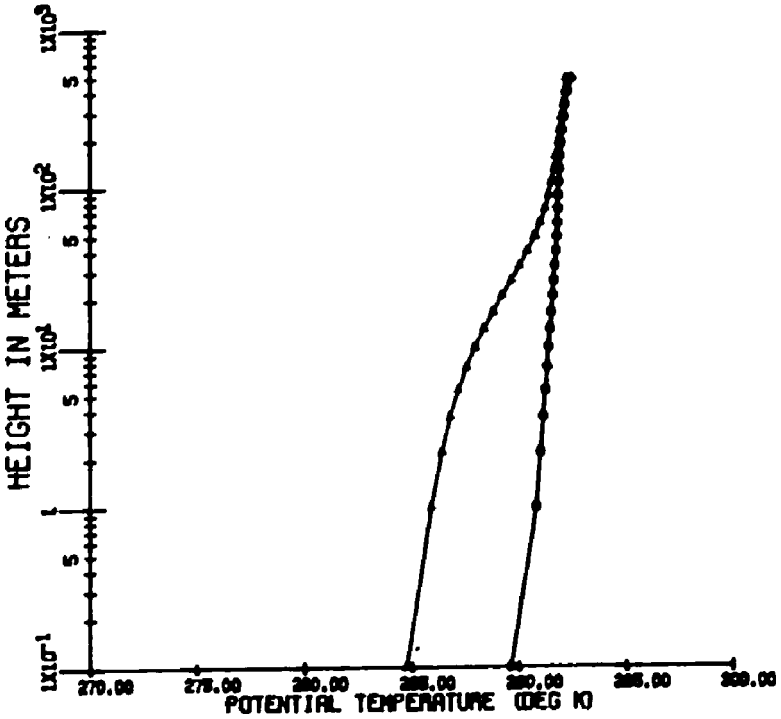


Fig. 4.14: Evolution of pre-fog θ profile, case 3. (—●—): t=0; (—▲—): t=2.75 hr.

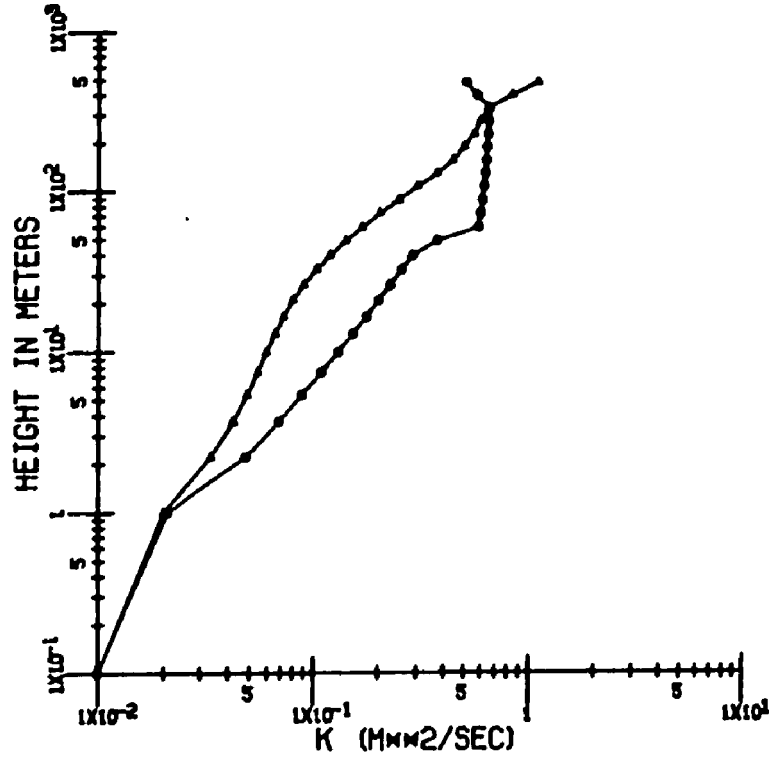


Fig. 4.15: As in Fig. 4.14, for K.

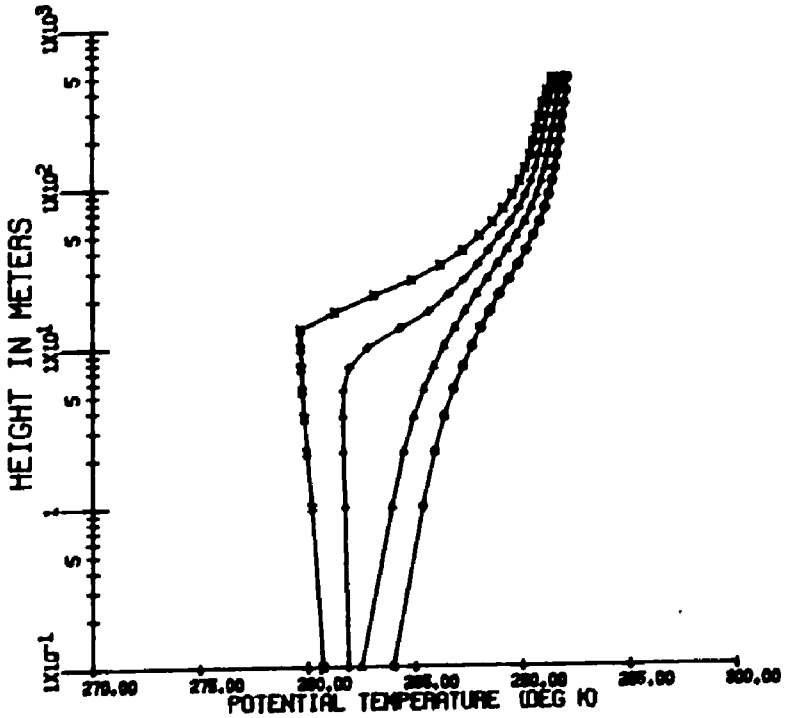


Fig. 4.16: Evolution of post-fog model θ profile, case 3. (—●—): t=3 hr; (—▲—): t=4 hr; (—+—): t=5 hr; (—✱—): t=6 hr.

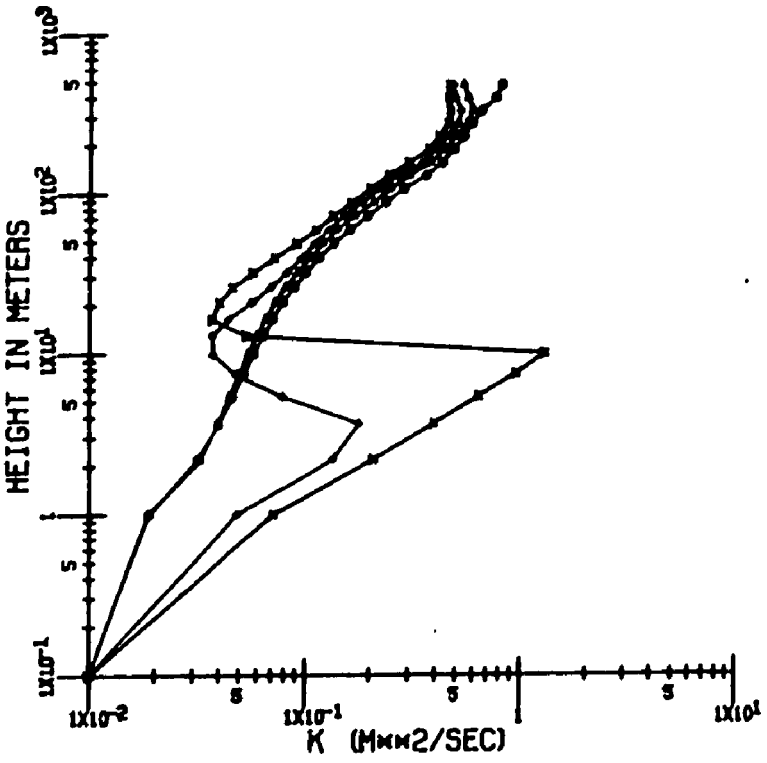


Fig. 4.17: As in Fig. 4.16, for K.

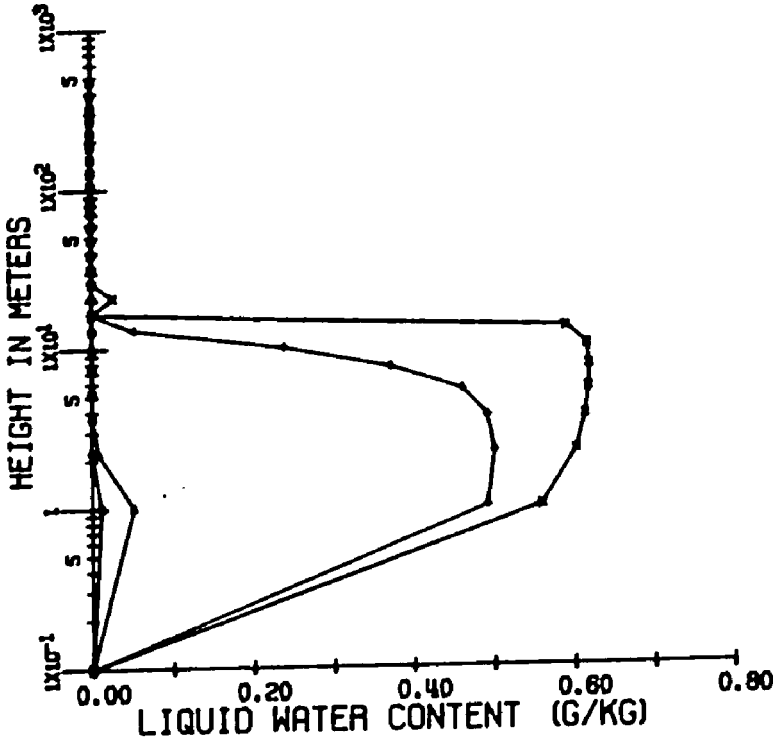


Fig. 4.18: As in Fig. 4.16, for ℓ.

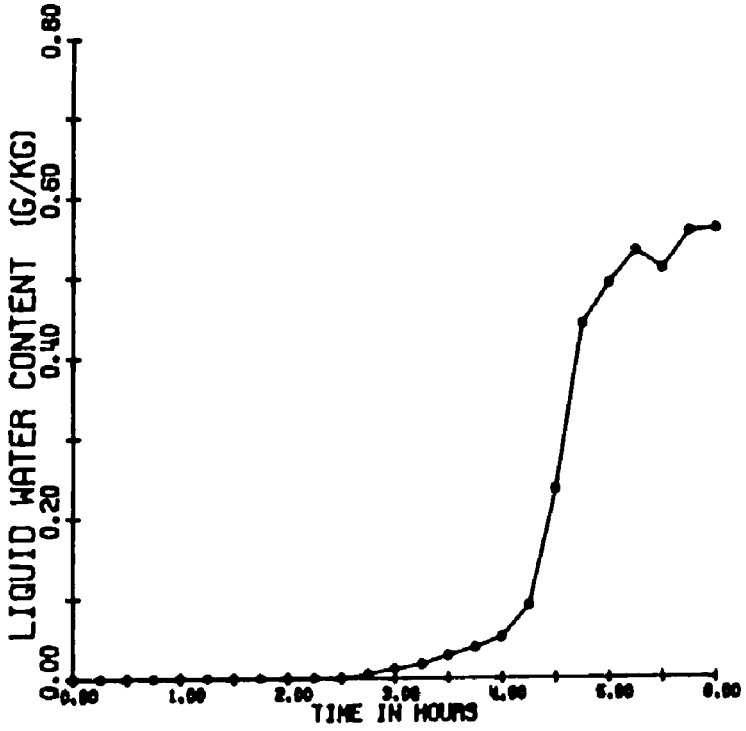


Fig. 4.19: Model-generated ℓ at z = 1 m as function of time, case 3.

a height of 12.9 meters by t=5 hr. The fog top remains at this height through t=6 hr, with an isolated layer of liquid water appearing at z=20.8 m. Model liquid water concentrations increase explosively after t= 4 hr. At t=6 hr, ℓ is virtually constant with height from 1.0 to 12.9 m at 0.6 g kg^{-1}, an unrealistically high value. The model fails to reproduce the observed rise in temperature and dew point after 2300 EST.

The combination of large liquid water concentrations and limited upward fog growth results in the computation of exaggerated values of long-wave radiative cooling within the model fog. Exaggerated radiative cooling is associated with similarly exaggerated rates of vapor condensation, further increasing ℓ.

Radiative cooling dominates the evolution of the θ profile during model fog development. The downward propagation of the cooling through turbulent exchange is evidently sufficient to counteract the reduction of net surface radiative heat loss by the fog. Thus, the model surface continues to cool, in contradiction to observations.

Additionally, the radiative cooling creates a barrier to the upward development of the model fog, as can be seen from the model θ and K profiles. As the model fog develops an unstable layer appears within the fog. K increases sharply in this layer. Conversely, the in-

version intensifies above the level of maximum radiative cooling, reducing K in this region and thus inhibiting the upward turbulent propagation of liquid water and of the cooling itself.

Hourly observations of visibility, visibility obstruction, temperature, dew point, wind direction, and wind speed for case 10 are given in Table 4.4. A very thin ground fog is observed at 0300 EST, with a visibility of 5 miles. Ground fog persists through 0700 EST. The minimum observed visibility of 1/2 mile is reported at both the 0600 and 0700 EST observations.

During the period of observed fog, the temperature rise observed in case 3 is absent. However, the observed temperature remains constant at 45°F from 0400 through 0600 EST, a period during which the visibility decreases from 2 miles to 1/2 mile. In the absence of fog, temperature would be expected to decrease under clear, calm conditions. Thus, it might be inferred that some reduction in net surface radiative heat loss resulted from the observed ground fog.

Observed case 10 temperature and dew point are compared with model-generated 1 m temperature and dew point in Figure 4.20. Figures 4.21-4.22 show model generated θ and K profiles at t=0 and at t=8.75 hr, immediately before model fog onset. Figures 4.23-4.25 show profiles of θ, K, and ℓ during the period of model fog development,

TABLE 4.4

HOURLY OBSERVATIONS AT FLINT
15-16 SEP 1963

HOUR (EST)	VIS (MI)	OBSTR	TEMP (°F)	DEW PT	WIND DIR	WIND SPD (MPH)
1800	10		67	54	ESE	6
1900	10		61	52	ESE	7
2000	10		56	51	SE	7
2100	10		55	50	SE	4
2200	10		54	49	CALM	
2300	10		53	49	CALM	
0000	10		50	48	SE	3
0100	7		48	47	CALM	
0200	7		49	46	CALM	
0300	5	GF	47	45	CALM	
0400	2	GF	45	44	SW	3
0500	2	GF	45	45	CALM	
0600	1/2	GF	45	45	E	4
0700	1/2	GF	47	47	E	3
0800	2	H	52	52	CALM	

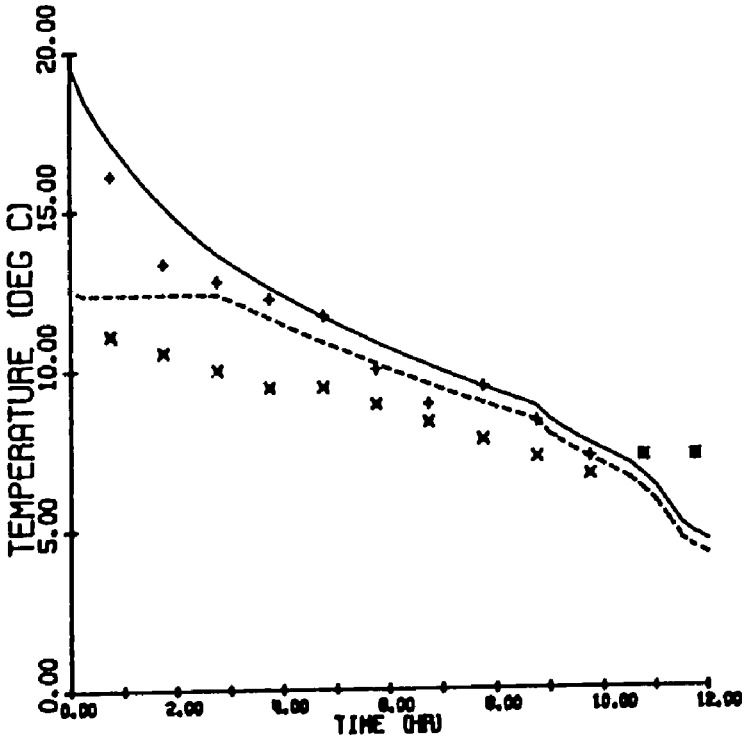


Fig. 4.20: Comparison of model-generated temperature and dew point with Flint hourly observations for both pre- and post-fog periods, case 10. Legend as in Fig. 4.1.

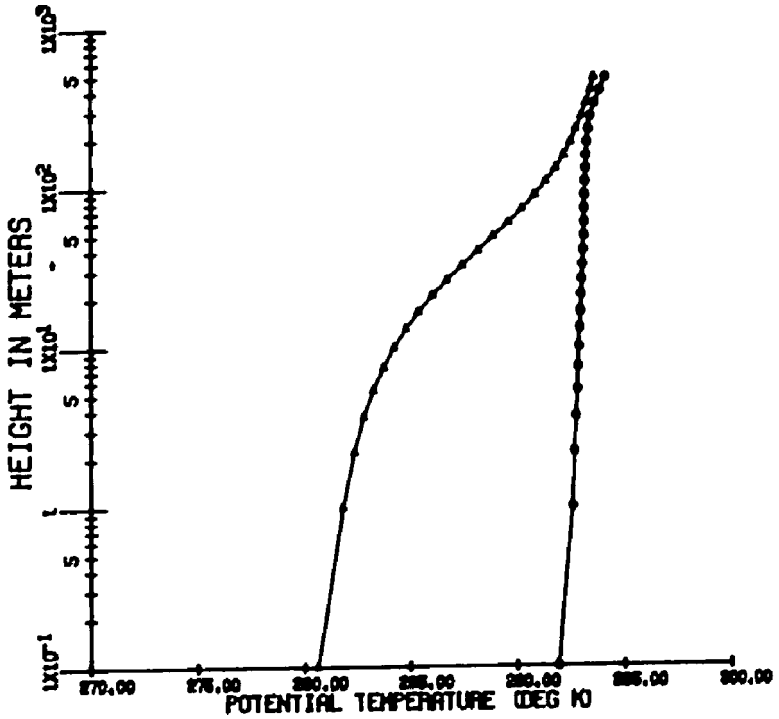


Fig. 4.21: Evolution of pre-fog θ profile, case 10. (—●—): t=0; (—•—): t=8.75 hr.

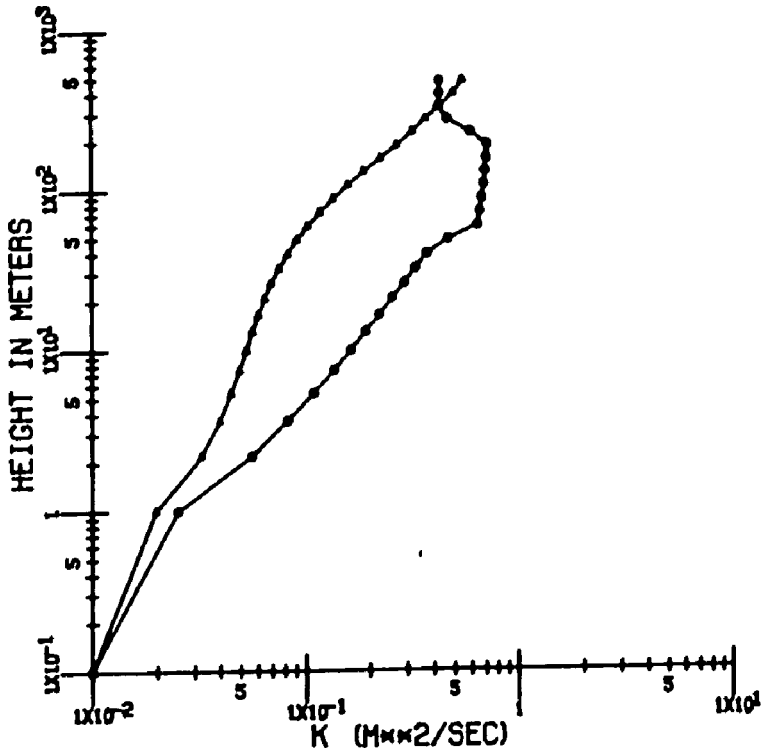


Fig. 4.22: As in Fig 4.21, for K.

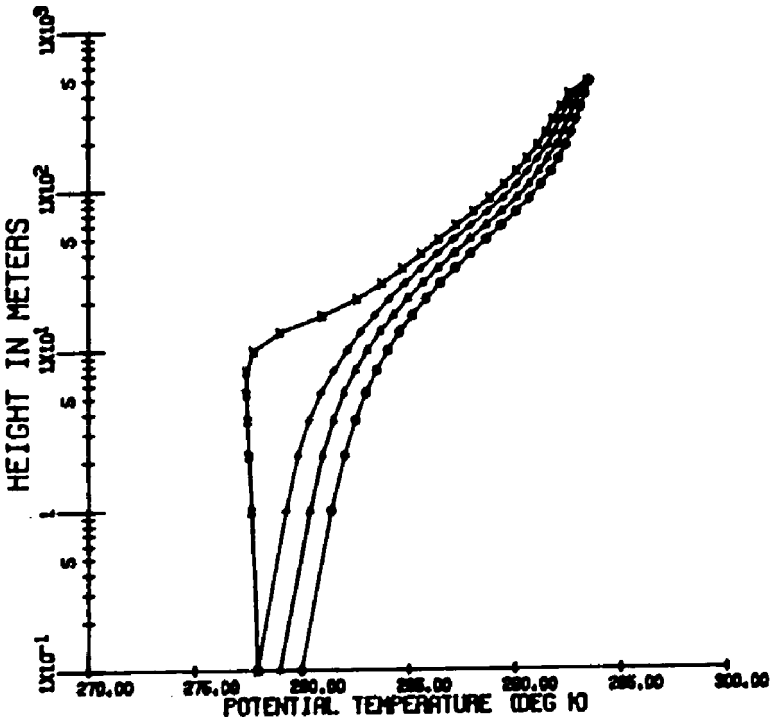


Fig. 4.23: Evolution of post-fog model θ profile, case 10. (—•—): t=9 hr; (—▲—): t=10 hr; (—+—): t=11 hr; (—✱—): t=12 hr.

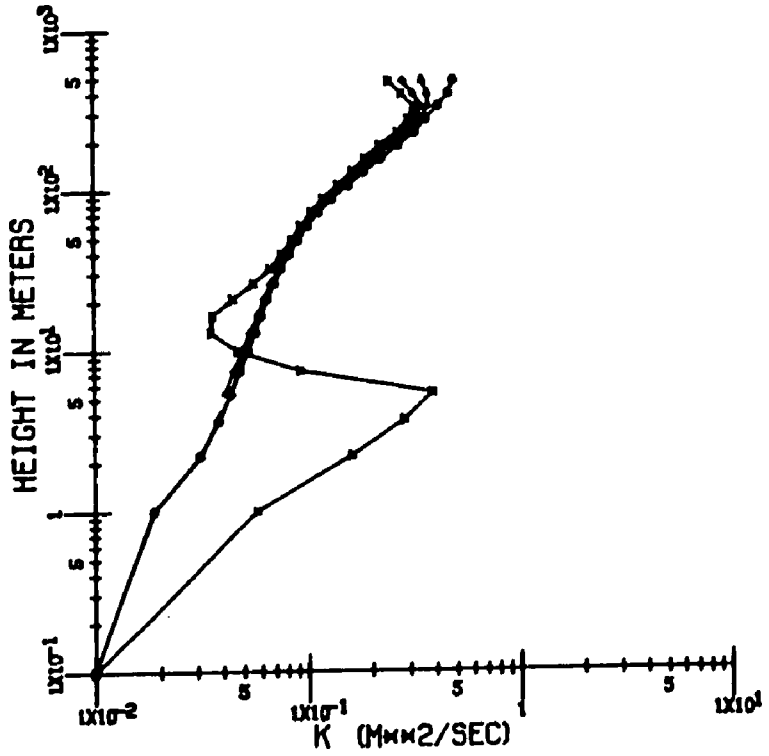


Fig. 4.24: As in Fig. 4.23, for K.

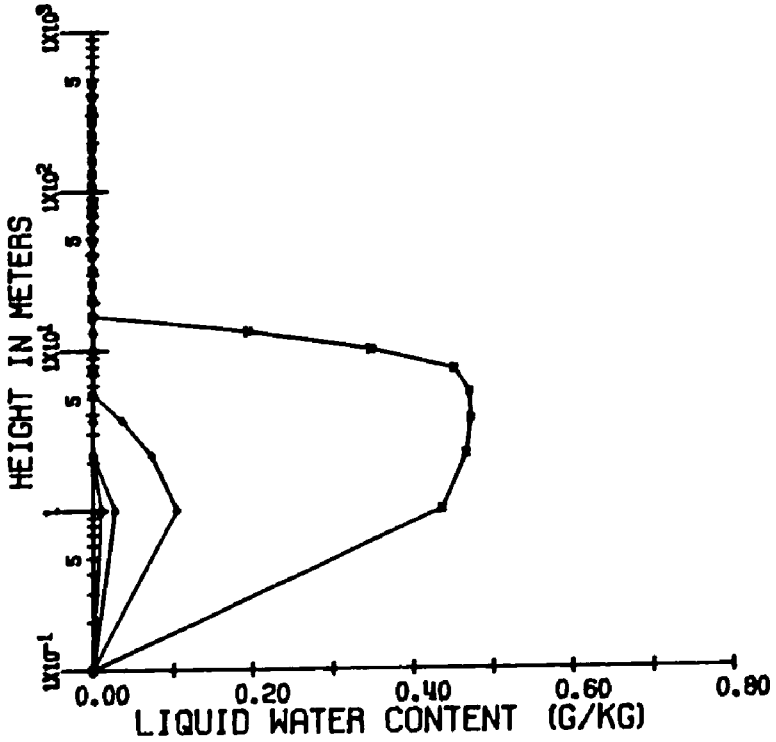


Fig. 4.25: As in Fig. 4.23, for ℓ.

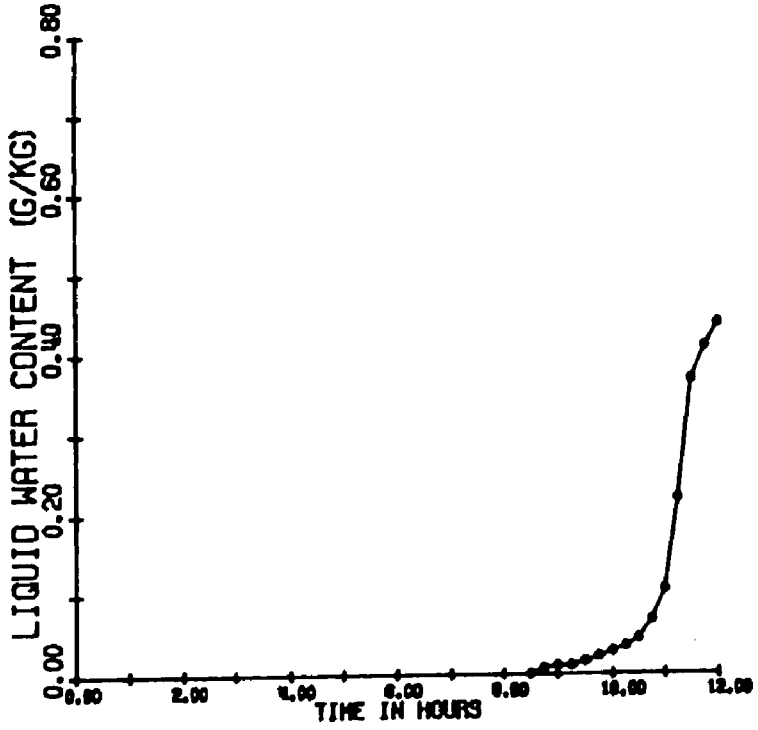


Fig. 4.26: Model-generated ℓ at z = 1 m as function of time, case 10.

and Figure 4.26 gives the liquid water concentration at z=1 m as a function of time.

The onset of model fog at t=8.77 hr is in virtual agreement with the first observation of ground fog at 0300 EST. Liquid water is confined to the 1 m level until t=10.5 hr, at which time upward model fog growth commences. By the end of the model run at t=12 hr, the model fog has reached a height of 12.9 m. Concurrent with upward growth are a sharp increase in liquid water concentration and the development within the fog of an unstable layer, similar to the features displayed in case 3. As in case 3, model temperature and dew point at z=1 m continue to fall after model fog onset.

The model fogs in cases 3 and 10 are very similar, although the observed fogs are not, a fact which indicates that the model is incapable of differentiating between ground fog and deep fog. However, the model fogs appear to be representative of observed patterns of deep fog formation at Flint. Deep fog ("F") was reported in 7 of the 11 cases considered here. In each of the deep fog cases, the initial deep fog observation is preceeded by one or more ground fog observations. Visibility at the initial deep fog observation is always equal to or less than 1/2 mile. Correspondingly, in the case 3 and case 10 model fog simulations, 1.2 and 1.7 hr respectively, elapse between model fog onset and the first appearance of li-

quid water above the first atmospheric level. It is apparent from both observations and model results that a ground fog must attain sufficient liquid water concentration before it can develop upward.

E. APPLICATION OF THE MODEL TO "NO-FOG" SITUATIONS

To complete the series of model verification experiments, the model was run on six cases in which fog failed to form at Flint on clear nights. Except for the absence of fog, these cases met the same criteria as the fog cases discussed previously. Additionally, it was required that the initial shelter-level dew point depression in each of the no-fog cases be less than 10.4°C, the maximum initial dew point depression observed among the fog cases. These conditions allow a true test of the ability of the model to distinguish between fog and no-fog situations.

Input parameters and model run procedure for the no-fog cases were identical to those described in section B. Table 4.5 summarizes relevant data on the no-fog cases, while Figures 4.27-4.32 show the comparisons of model-generated 1 m temperature and dew point with Flint hourly observations. The model predicted fog in each of the no-fog cases except for case 14. In case 12, the fog prediction appears related to the inability of the model to simulate transient processes. Model-generated 1 m temperature and dew point are in relative agreement with observations

TABLE 4.5

RELEVANT DATA FOR SELECTED
Flint "NO-FOG" CASES

CASE NO.	DATES	INITIAL DEW PT DEPR. (°C)	MEAN 1900-0600 WIND SPEED (MPH)	MODEL FOG ONSET (HR)
12	29-30 SEP 1959	7.1	2.4	11.95
13	9-10 OCT 1959	4.8	3.1	7.54
14	15-16 SEP 1961	7.0	4.1	NONE
15	26-27 SEP 1961	5.3	3.8	8.99
16	28-29 SEP 1961	6.4	3.3	11.67
17	5-6 OCT 1961	7.4	6.4	10.15

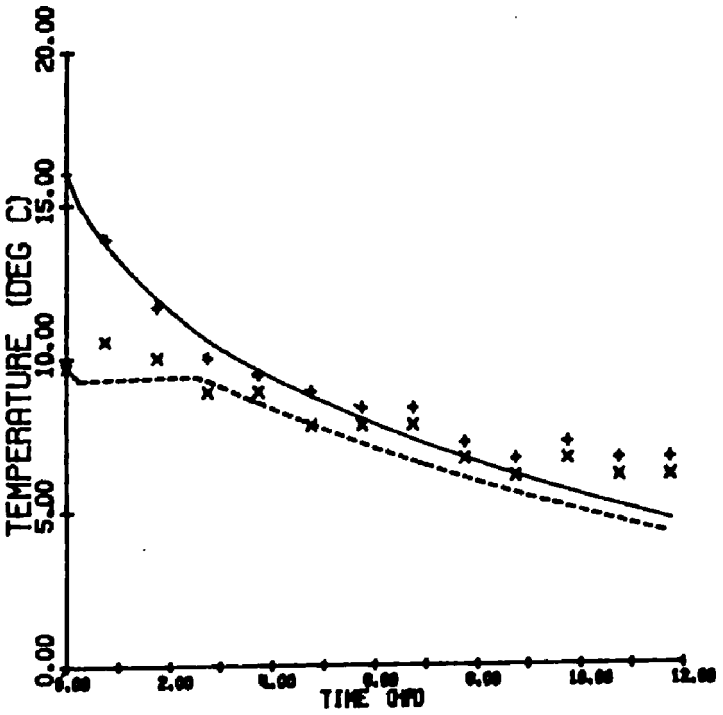


Fig. 4.27: As in Fig. 4.1, for case 12.

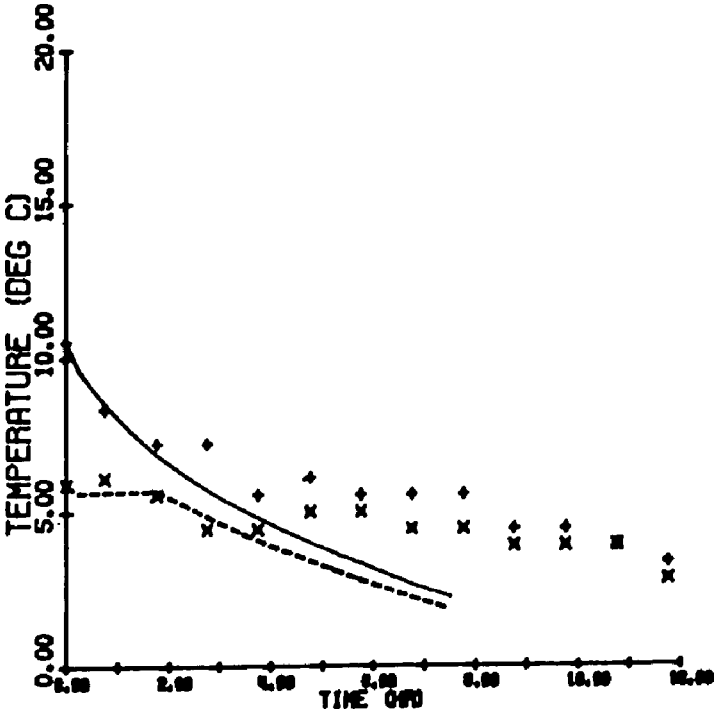


Fig. 4.28: As in Fig. 4.1, for case 13.

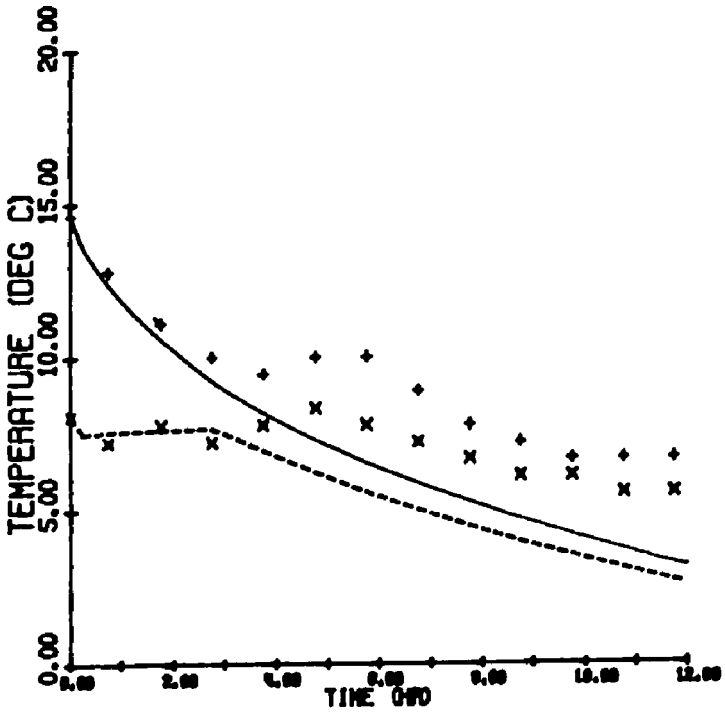


Fig. 4.29: As in Fig. 4.1, for case 14.

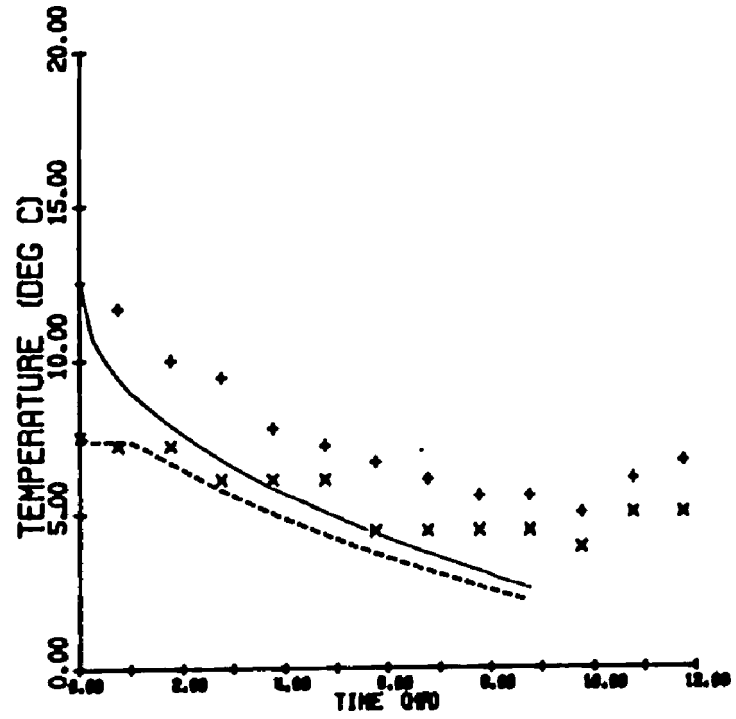


Fig. 4.30: As in Fig. 4.1, for case 15.

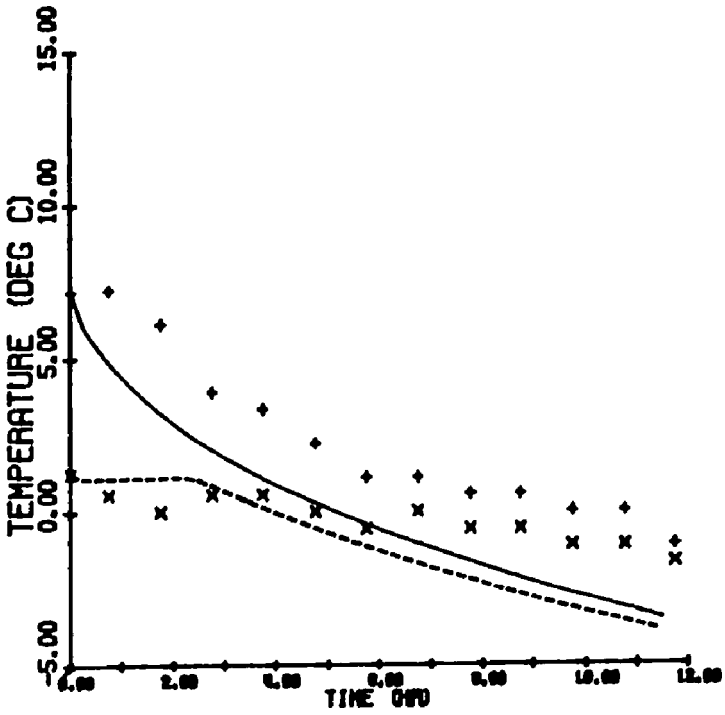


Fig. 4.31: As in Fig. 4.1, for case 16.

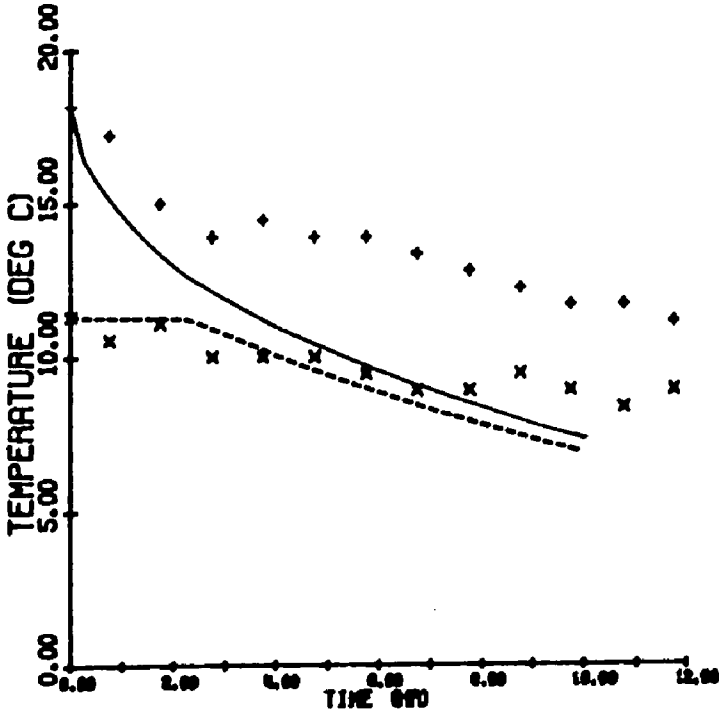


Fig. 4.32: As in Fig. 4.1, for case 17.

through 0300 EST. The model fails, however, to predict the warming observed between 0300 and 0400 EST, a warming which might very well have prevented fog formation in this case.

Cases 13 through 17 are each characterized by model-generated 1 m temperatures significantly lower than those observed temperatures, a result which suggests that atmospheric turbulent exchange in these cases was more intense than that represented by model-generated exchange coefficients.

To test this assertion, cases 13 through 17 were rerun with u_* increases to 15 cm sec^{-1}, all other conditions remaining the same. Model fog formed only in case 17, at t=8.42 hr. Model-predicted temperatures at z=1 m and t = 8 hr in each case are approximately 1°C higher than they are with u_* = 10 cm sec^{-1}, although still lower than observed temperatures. Model-predicted dew points are also higher, as a result of decreased cooling, and thus higher saturation values of q at the surface. Increased model-generated turbulence, however, results in an increased downward flux of moisture. Thus, the increase in the model dew point at z=1 m is slightly less than the corresponding increase in model temperature, preventing or delaying model fog formation.

The model results in the no-fog cases suggest that turbulence inhibits fog formation. These results also

illustrate the difficulties inherent in the use of a model of this type to distinguish between potential fog and no-fog situations, based on routinely available observations. For the model to be effective, a method of assigning or predicting u_* over a 12-hour period would be necessary. None is obvious at this point.

CHAPTER V: ANALYSIS OF MODEL SENSITIVITY

A. MOTIVATION AND PROCEDURE

As detailed in the previous two chapters, a number of assumptions are made in running this model. These assumptions encompass (1) model initialization procedure; (2) formulation of boundary conditions for model variables; and (3) assignment of values to atmospheric and soil parameters. In this chapter, the response of the model to alterations in a number of these assumptions will be discussed. This analysis is meant to test the sensitivity of the model and, by extension, to examine the relationship of various characteristics of the atmosphere and soil to fog formation.

The sensitivity studies have been limited to the pre-fog stage, except in the cases of two parameters which apply only to fog: the bulk mass absorption coefficient k_w and the droplet settling parameter s. Factors which affect atmospheric behavior before fog forms continue to exert an effect after fog formation. However, it was felt that carrying the model sensitivity runs past the onset of model fog would shed little light upon atmospheric physics, given the poor performance of the model in simulating fog development in the verification experiment.

All model sensitivity tests are based upon case 6 of the previous chapter except those for k_w and s, which are based on case 3. The term "basic run" will be used here

to refer to model results from the verification experiment. Each sensitivity test involves the variation of a given assumption or parameter over a range of forms or values, with all other model specifications identical to those of the basic run. Certain features of the model output are then compared to results of the basic run to determine the effect of the variation.

B. EFFECT OF INITIAL SOIL TEMPERATURE PROFILE

In the basic run for case 6, the three-layer initial soil profile described in chapter 3 is assumed. The temperature at the soil-atmosphere interface is 291.74 K, equal to the initial surface value of θ obtained by extrapolating the 0000 GMT radiosonde data. T_s at the lowest soil level, $z=-0.72$ m, is arbitrarily assumed to be 289 K and is held constant throughout the model run.

Model runs were made specifying each of two initial soil temperature profiles, which are illustrated along with the basic profile in Fig. 5.1. In run B1, the soil is initially isothermal with depth, at a temperature of 291.74 K. In run B2, the top two layers of the basic initial soil profile are eliminated; T_s is interpolated logarithmically from 291.74 K at the surface to 289 K at the lowest level.

Model fog forms at t=10.07 hr in the basic run, at t=8.76 hr in run B1, and at t=8.32 hr in run B2. Fig. 5.2 compares the behavior of θ at z=1 m in the basic run, run

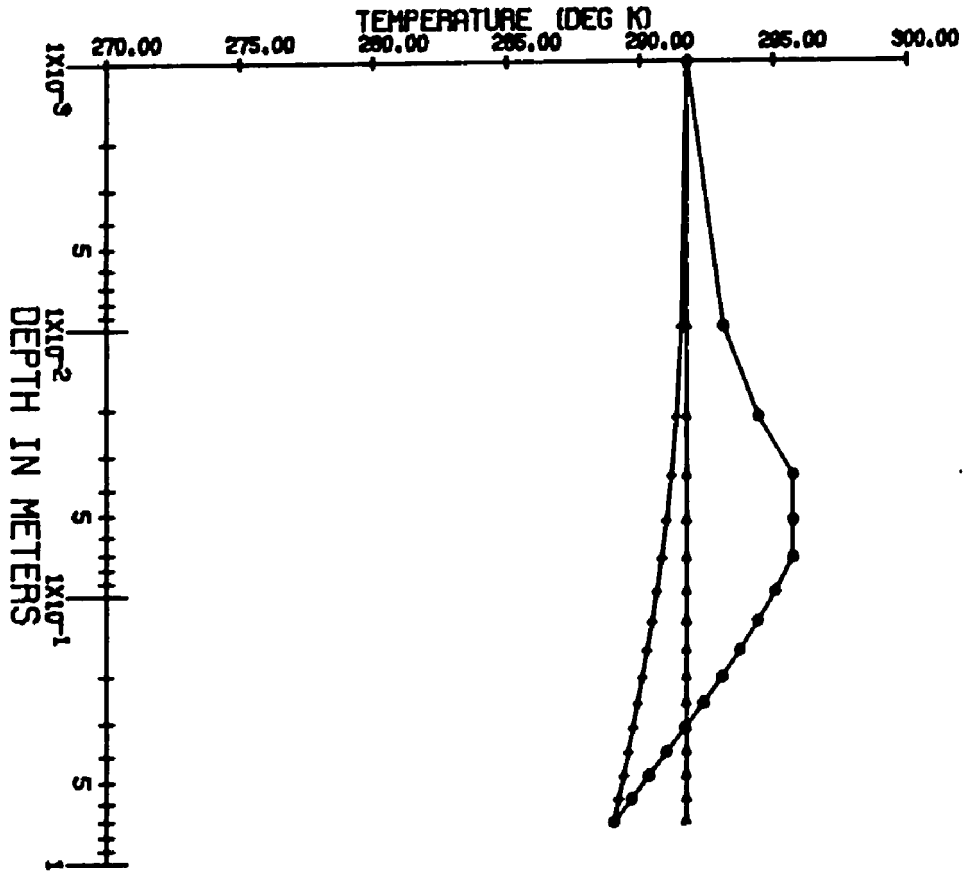


Fig. 5.1: Initial soil temperature profiles. (—●—): basic run; (—+—): run B1; (—+—): run B2

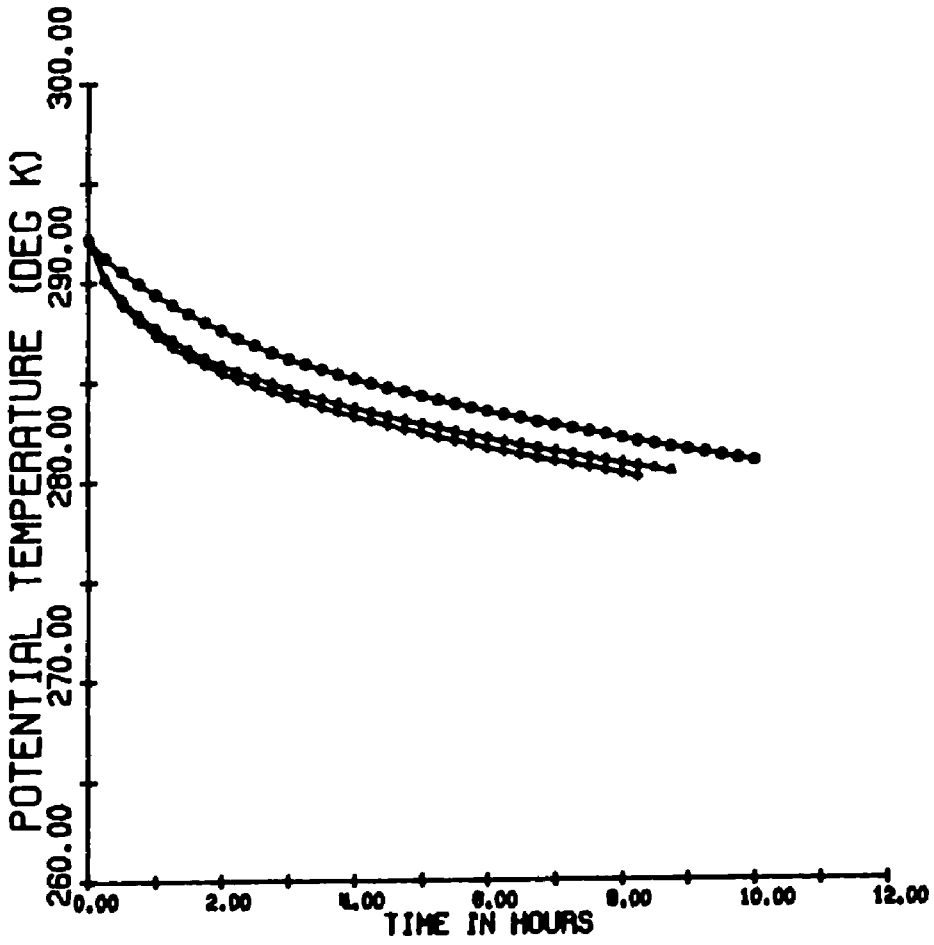


Fig. 5.2: Model-predicted θ at z = 1 m.
(—●—): basic run; (—▲—): run B1
(—+—): run B2

B1, and run B2. The behavior of θ at levels near the surface reflects the effect of soil flux heat on the surface heat balance. With the initial T_s profile of the basic run, the soil heat flux

$$Q_s \equiv \rho_s c_s k_s \frac{\partial T_s}{\partial z}$$

is initially directed toward the surface. In run B1, there is no initial soil heat flux, and in run B2, there is an initial soil heat flux directed away from the surface. Thus, cooling rates in the first hour of runs B1 and B2 are greater than in the basic run. Later in the model runs, T_s gradients become similar near the surface, and 1-m cooling rates are likewise similar. The increased cooling of the first hour, though offset in part by earlier commencement of atmospheric moisture loss through dew formation, is responsible for earlier model fog onsets in runs B1 and B2.

C. EFFECT OF SOIL PARAMETERS

Values must be assigned to three soil parameters: density (ℓ_s), specific heat (c_s), and thermal diffusivity (k_s). All three are part of the expression for soil heat flux appearing in the surface heat balance equation. Additionally, k_s appears in the prognostic equation for T_s. For the purpose of this analysis, $\rho_s c_s$ can be considered as a single parameter, the specific heat per unit volume.

In the verification experiment $\rho_s c_s = 5 \times 10^5 \text{cal m}^{-3}\ ^\circ\text{K}^{-1}$, and $k_s = 3 \times 10^{-7}\ \text{m}^2\text{sec}^{-1}$. In the model runs C1 and

C2, $\rho_s c_s$ was assigned values of 2×10^5 and 8×10^5 cal $m^{-3} \circ K^{-1}$, respectively. In model runs C3 and C4, k_s was assigned the respective values of 1×10^{-7} and 6×10^{-7} $m^2 sec^{-1}$. Both $\rho_s c_s$ and k_s generally increase with soil moisture content (Geiger, 1965).

In run C1, fog forms at t=5.21 hr, while fog fails to form in run C2. When $\rho_s c_s$ is reduced, the flow of heat from the soil to surface is likewise reduced, increasing the surface cooling rate throughout the model run. The reverse occurs when $\rho_s c_s$ is increased. The behavior of θ at z=1 m, shown in Fig. 5.3, reflects the difference in surface cooling rates resulting from the variations in $\rho_s c_s$.

When k_s is varied, the effect upon soil heat flux is similar to that produced by variation of $\rho_s c_s$. Reduced k_s in run C3 results in increased low-level atmospheric cooling and a model fog onset at t=6.66 hr. The increased k_s in run C4 inhibits cooling; model fog does not form in this run. Fig. 5.4 illustrates the comparative behavior of θ at z=1 m in the basic run, run C3, and run C4.

The results presented in this and the previous section indicate that the model is sensitive to assumptions concerning the soil. However, the physical implications of these results are less clear. If all other conditions, including the initial T_s profile, are identical, the model results show that fog formation is more likely over "dry"

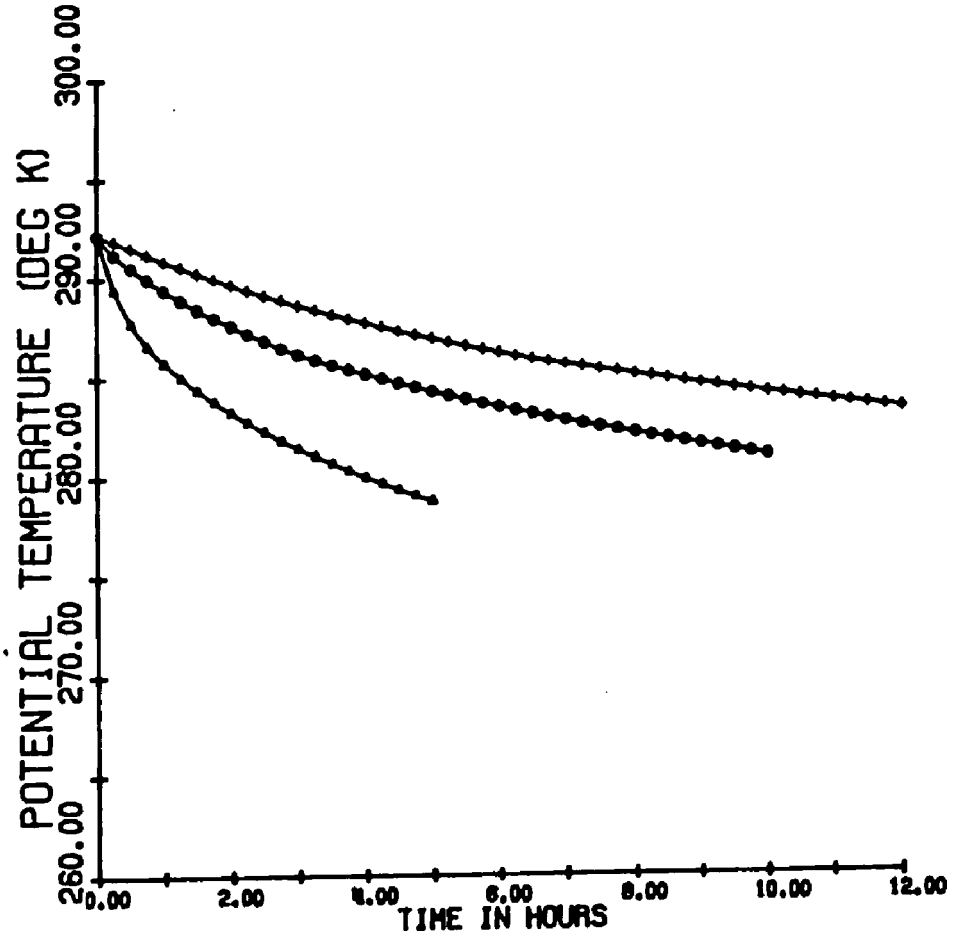


Fig. 5.3: Model-predicted θ at z = 1 m.
(—•—): basic run; (—▲—): run C1
(—+—): run C2

Basic run: $\rho_s c_s = 5 \times 10^{+5}$ cal m^{-3} $°K^{-1}$
Run C1: $\rho_s c_s = 2 \times 10^{+5}$ cal "
Run C2: $\rho_s c_s = 8 \times 10^{+5}$ cal "

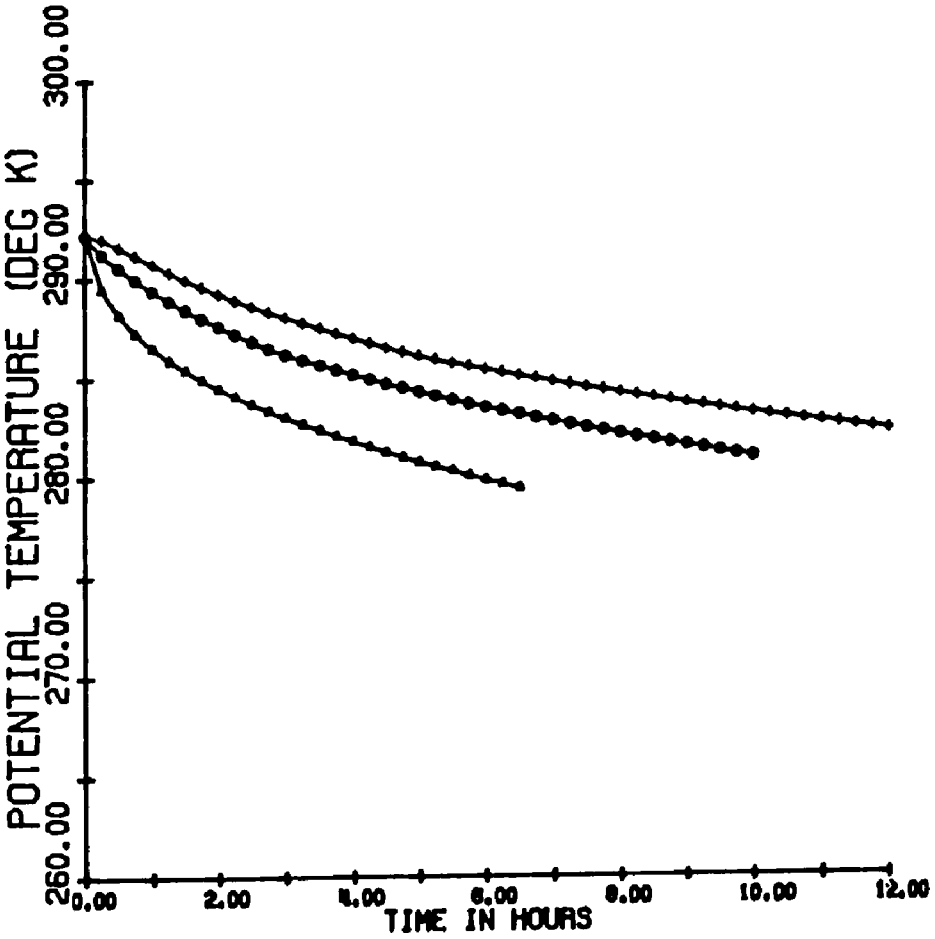


Fig. 5.4: Model-predicted θ at z = 1 m.
(—●—): basic run; (—◂—): run C3
(—+—): run C4

Basic run: $k_s = 3 \times 10^{-7}$ $m^2 sec^{-1}$
Run C3: $k_s = 1 \times 10^{-7}$ "
Run C4: $k_s = 6 \times 10^{-7}$ "

soil (low values of $\rho_s c_s$ and k_s) than over "wet" soil (high values of $\rho_s c_s$ and k_s). Yet in reality, the profile of T_s at sunset is by no means independent of the soil characteristics. Large values of k_s, for example, would tend to facilitate heat transfer within the soil during the day, weakening the gradients of T_s resulting from diurnal heating. According to model results in runs B1 and C4, a smoothing of the initial T_s profile would tend to cancel the effect of an increase in k_s. The difficulty in drawing physical conclusions from studies of this type is thus illustrated.

D. MODEL RESPONSE TO CHANGES IN THE INITIAL θ PROFILE

While most objective fog forecasting schemes (e.g., George, 1950) rely upon shelter-level observations alone, a model of this type utilizes vertical profiles of θ and q as initial conditions. Model run D1 was made to test the effect on model output of data levels other than shelter-level. The initial θ profile for run D1 is obtained from a temperature sounding with the following characteristics: (1) the shelter-level (1.5 m) temperature is identical to the initial shelter-level temperature in the case 6 basic run; (2) the temperature at a height of 100 m is 2 K higher than at shelter-level; and (3) a dry adiabatic lapse rate exists between 100 m and the model top at 472 m. Temperatures at significant levels above the model top are identical in the basic run and in run D1;

profiles of q are also identical.

Fig. 5.5 compares the initial θ profiles in the basic run and in run D1. Note that the downward extrapolation of the initial θ profile from shelter-level produces an initial surface value of θ 3.1 K cooler in run D1 than in the basic run.

Fog fails to form in run D1. Figures 5.6 and 5.7 show the comparative behavior of θ and q, respectively at z=1 m in the basic run and in run D1. The lower initial value of θ at the surface in run D1 is responsible for the increased cooling at 1 m within the first hour. After the first hour, the 1-m cooling rate is slightly lower in run D1 than in the basic run, as more heat is transferred downward from aloft. Surface saturation is reached 1.25 hr earlier in run D1 than in the basic run; as a result, atmospheric moisture loss via dew formation is sufficiently increased over the basic run to prevent model fog formation. It should be noted that run D1 is the only run in this series in which increased cooling at 1 m is <u>not</u> associated with earlier fog formation. The results of run D1 suggest that a strong inversion in the first meter at sunset does not favor the formation of nocturnal fog.

E. EFFECT OF THE SURFACE MOISTURE CONDITION

In the model runs of the previous chapter, the surface value of q is assumed initially equal to the value of q at 1 m, and held constant until the surface cools to

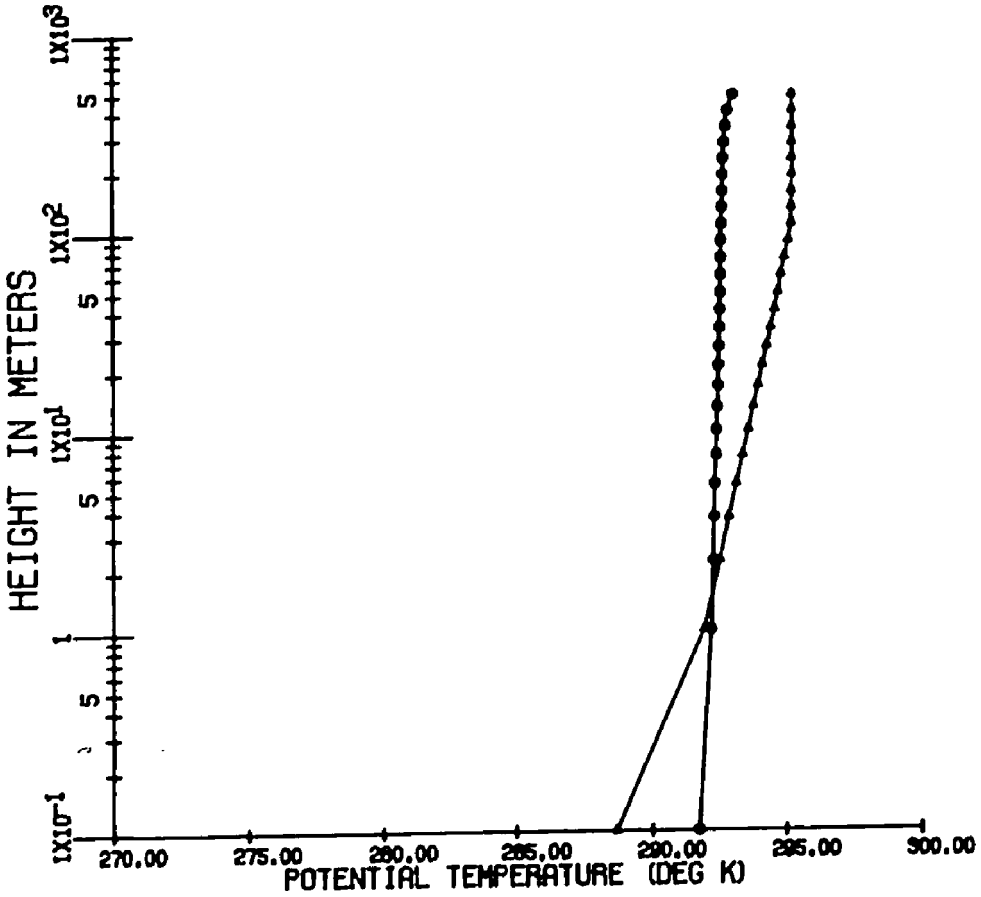


Fig. 5.5: Initial θ profiles.
(—●—): basic run; (—▲—): run D1

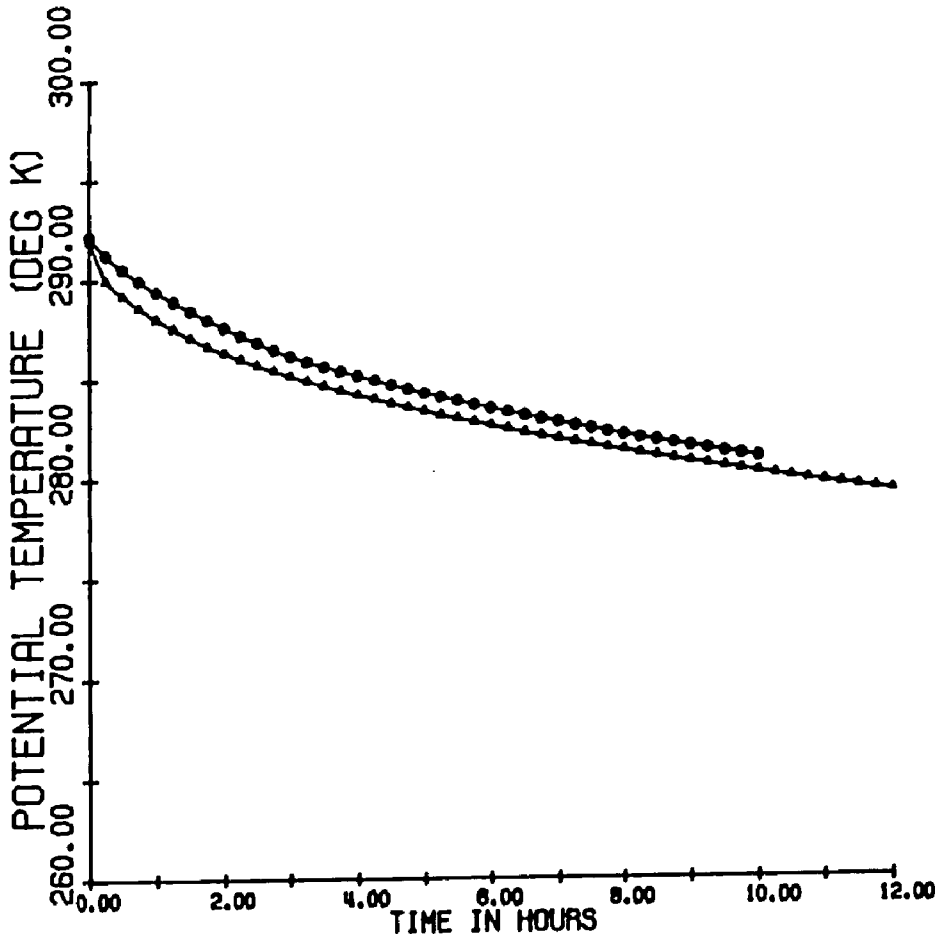


Fig. 5.6: Model-predicted θ at z = 1 m.
(—●—): basic run; (—▲—): run D1

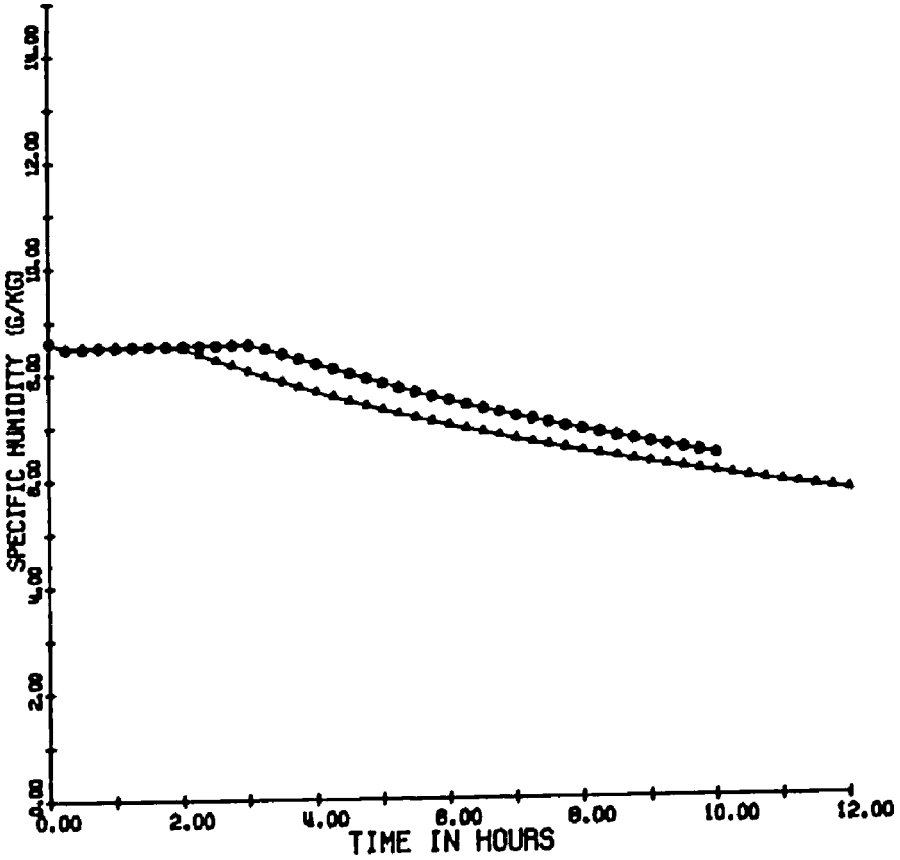


Fig. 5.7: Model-predicted q at z = 1 m.
(—●—): basic run; (—▲—): run D1

saturation. Once surface saturation is reached, q is assumed to equal the saturation value at the surface temperature, with continued surface cooling resulting in a flux of moisture toward the surface as dew is formed.

Two alternative formulations of the surface moisture condition were tested. In run E1, the surface is assumed to be initially saturated. In run E2, dew formation is suppressed by maintaining the surface specific humidity at its initial value after surface saturation is reached.

Model fog appears in run E1 at t=9.12 hr, or 0.95 hr earlier than in the basic run. Fig. 5.8 compares the behavior of q at 1 m in the basic run and in run E1. Initial saturation results in a strong upward moisture flux at the beginning of run E1. While q increases sharply at 1 m in the first 15 minutes of this run, surface cooling and concurrent dew formation result in the rapid establishment of a moisture inversion and a reversal of the low-level moisture flux. Between t=0.25 hr and t=3 hr, the q excess in run E1 decreases from 2.32 to 0.27 g kg^{-1}; after 9 hr, the excess is only 0.05 g kg^{-1}. The effect of initial surface saturation on θ is minimal, amounting to an excess of 0.08 K at t=9 hr.

In run E2, model fog onset occurs at t=3.72 hr. Fig. 5.9 shows the q profiles at t=3.5 hr for the basic run and for run E2. The area enclosed by the two profiles and the horizontal axis represents the atmospheric moisture

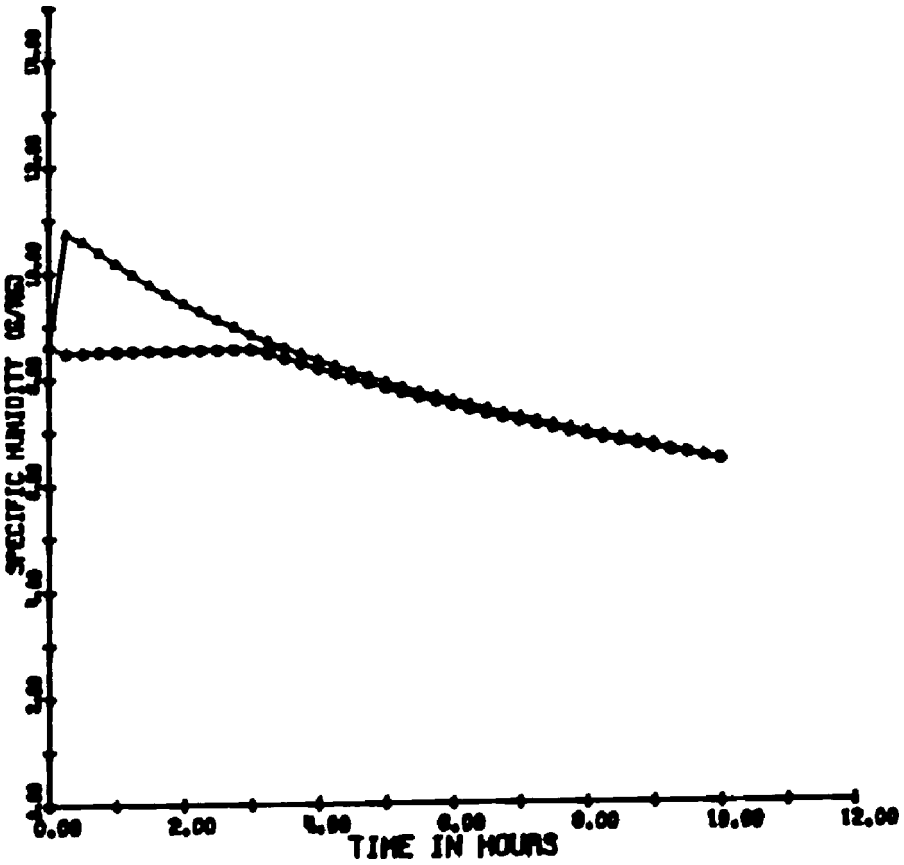


Fig. 5.8: Model-predicted q at z = 1 m.
(—●—): basic run; (···▲···):
run E1 (initial saturation at z = 0)

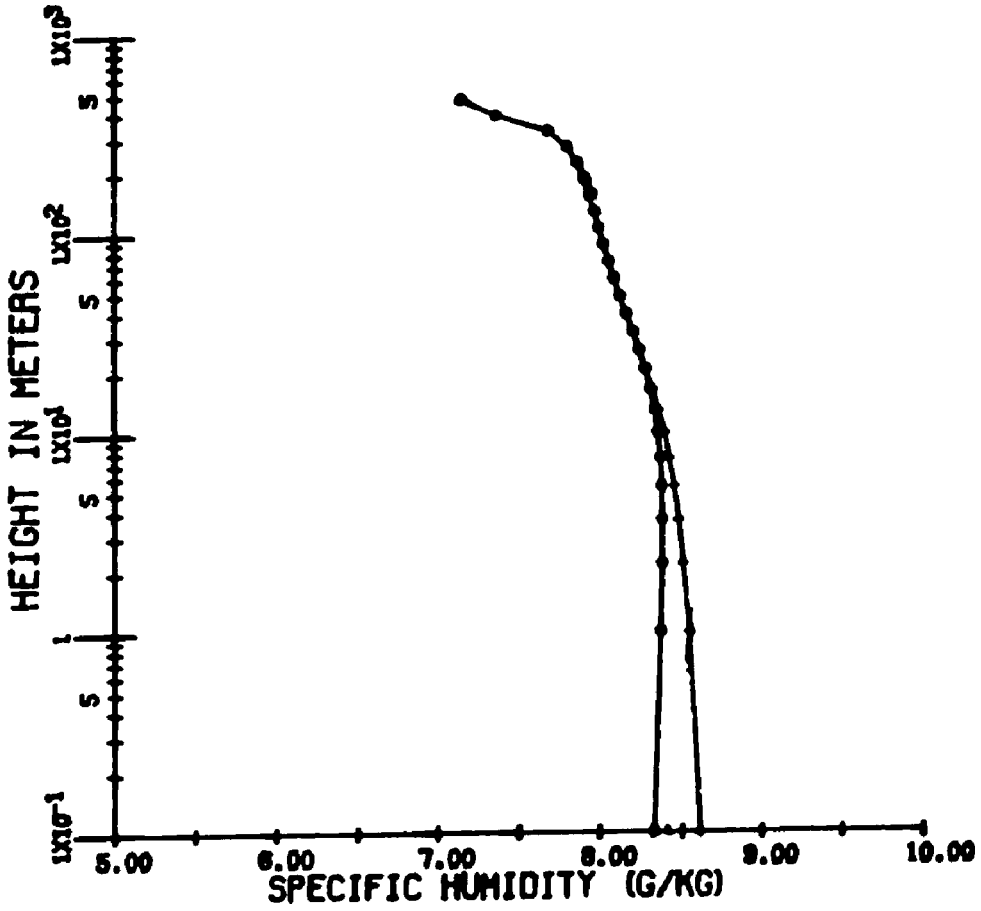


Fig. 5.9: Profiles of q at t = 3.5 hr.
(—●—): basic run; (—▲—): run E2 (no dew)

loss incurred through dew formation in the first 3.5 hr of the basic run. Retention of this moisture in run E2 results in early fog onset.

The results of model runs E1 and E2 illustrate the critical relationship between dew and fog, and the importance of accurate representation of low-level moisture fluxes in an effective fog prediction model.

F. THE RELATIONSHIP BETWEEN CONDENSATION RELATIVE HUMIDITY AND MODEL FOG ONSET

In a polluted atmosphere, the abundance of available condensation nuclei reduces the relative humidity at which condensation may commence. In order to determine the relationship between condensation relative humidity and model fog onset time, a case 6 model run was made in which no condensation relative humidity was specified. In Fig. 5.10, relative humidity computed from θ and q at 1 m is plotted against time. The curve in Fig. 5.10 can be used to determine the time at which condensation would commence in case 6 if a given condensation relative humidity were assigned. (Although model fog onset has previously been defined as the time at which ℓ first exceeds 0.01 g kg^{-1}, initial condensation precedes model fog onset by less than 0.10 hr in all cases considered in this study.)

After dew formation commences, at t=3 hr, the 1 m model relative humidity increases very slowly with time. Model fog onset time is this shown to be extremely sensi-

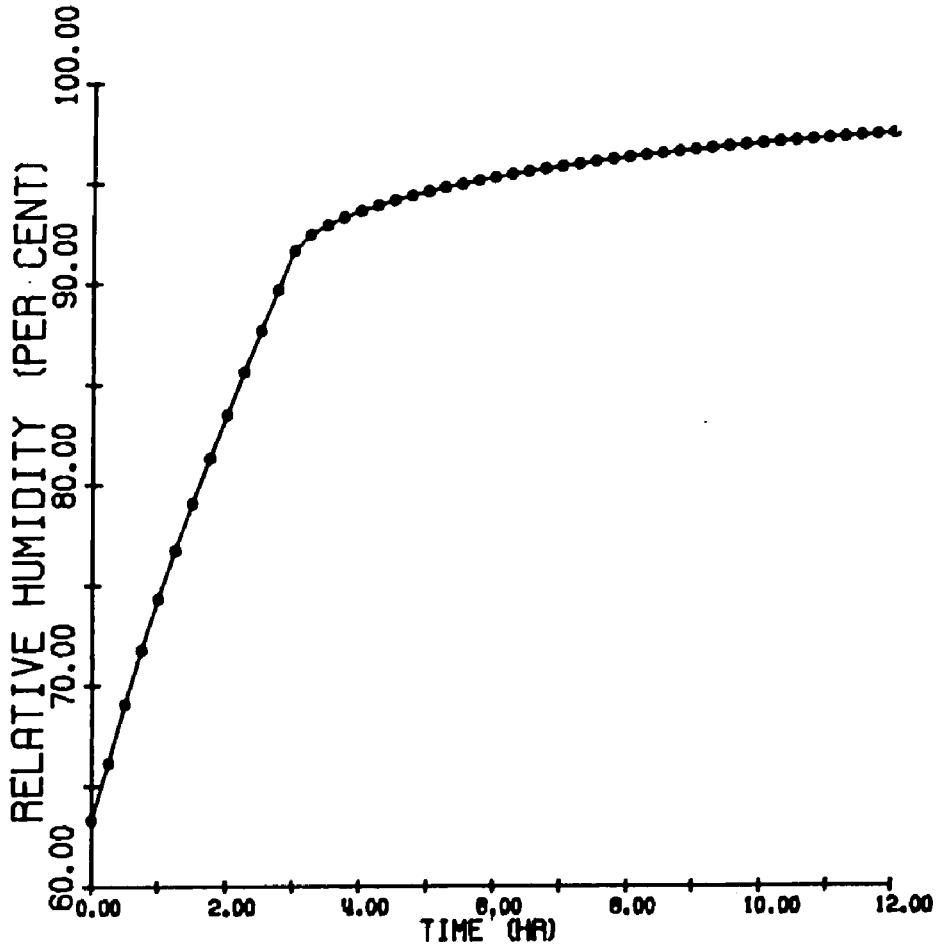


Fig. 5.10: Relative humidity computed from model θ and q at z = 1 m, for case 6.

tive to the relative humidity at which condensation is allowed to take place.

G. EFFECT OF TURBULENT EXCHANGE COEFFICIENT

The computation of turbulent exchange coefficients by the model requires the arbitrary specification of the friction velocity u_*. In the verification experiments, u_* was assigned a value of 10 cm sec^{-1}. Model runs G1 and G2 were made on case 6 with assigned values of 5 and 20 cm sec^{-1}, respectively. Fog forms at t=7.96 hr in run G1, 2.11 hr earlier than in the basic run. Fog fails to form in run G2.

Fig. 5.11 shows the initial profiles of K computed by the model in the basic run, run G1, and run G2. Fig. 5.12 compares the behavior of θ at 1 m in the three model runs, while Figures 5.13 and 5.14 compare the profiles of θ and q at t=7 hr.

A reduction in K at all model levels which occurs in run G1 results in increased cooling at the surface, due to a decrease in the turbulent flux of heat from above. As shown in Fig. 5.13, the increased cooling is transmitted upward only to the first few meters of the atmosphere; at higher levels, decreased turbulent exchange is associated with decreased cooling. The specific humidity, governed at low levels by surface cooling once dew formation commences, shows the same pattern. In run G1, the increase moisture loss at 1 m does not compensate for the

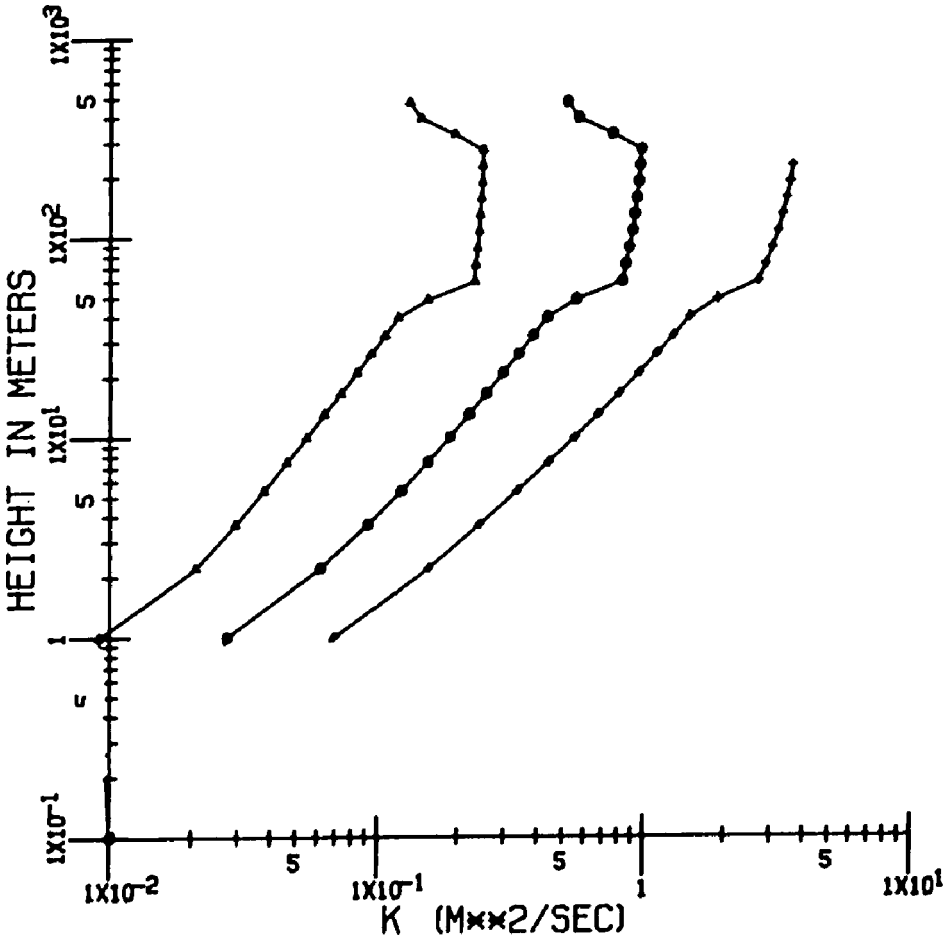


Fig. 5.11: Initial K profiles.
(—●—): basic run; (—▲—): Run G1;
(—+—): Run G2

Basic run: $u_\star$ = 10 cm sec^{-1}
Run G1: $u_\star$ = 5 "
Run G2: $u_\star$ = 20 "

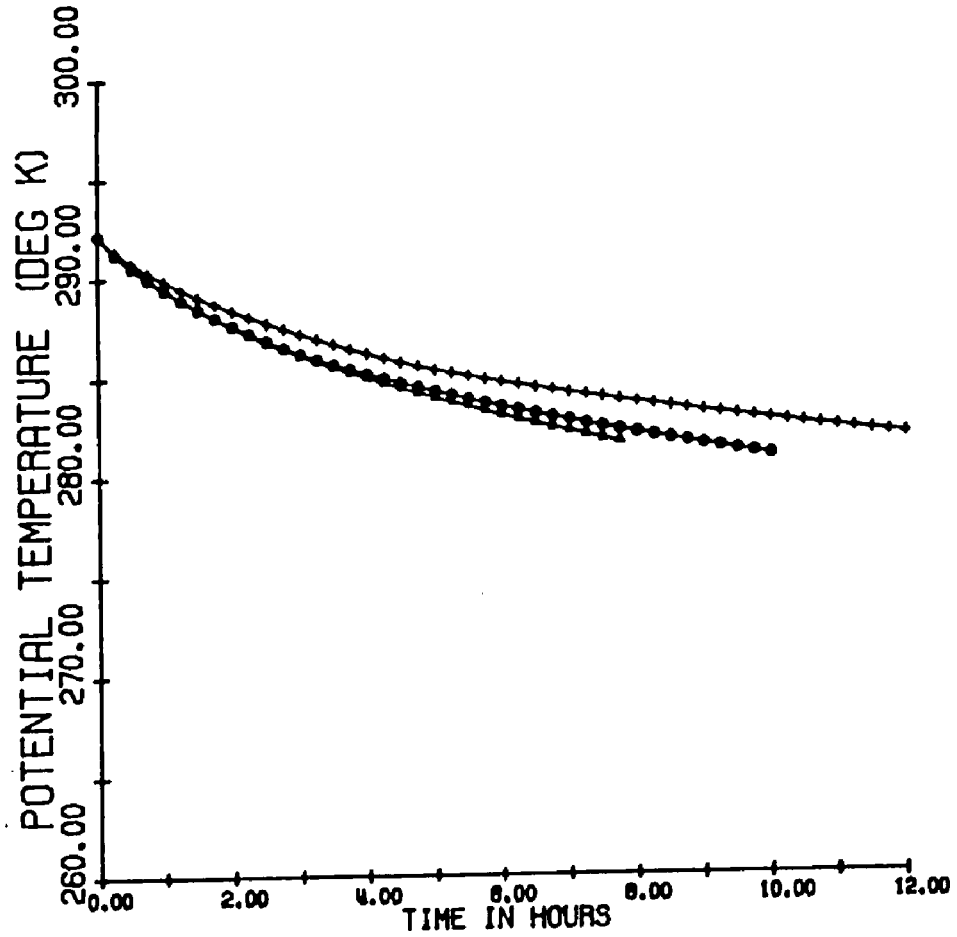


Fig. 5.12: Model-predicted θ at z = 1 m.
(—●—): basic run; (—▲—): run G1;
(—+—): run G2

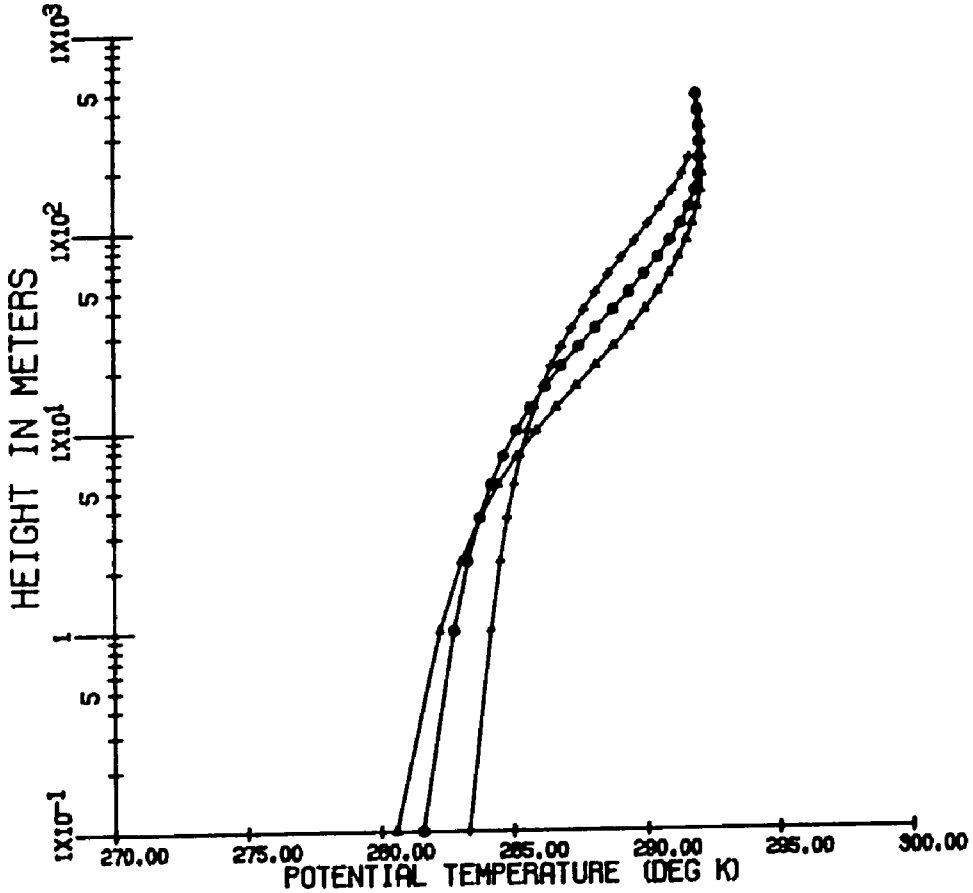


Fig. 5.13: Profiles of θ at t=7 hr.
(—●—): basic run; (—▲—): run G1;
(—+—): run G2

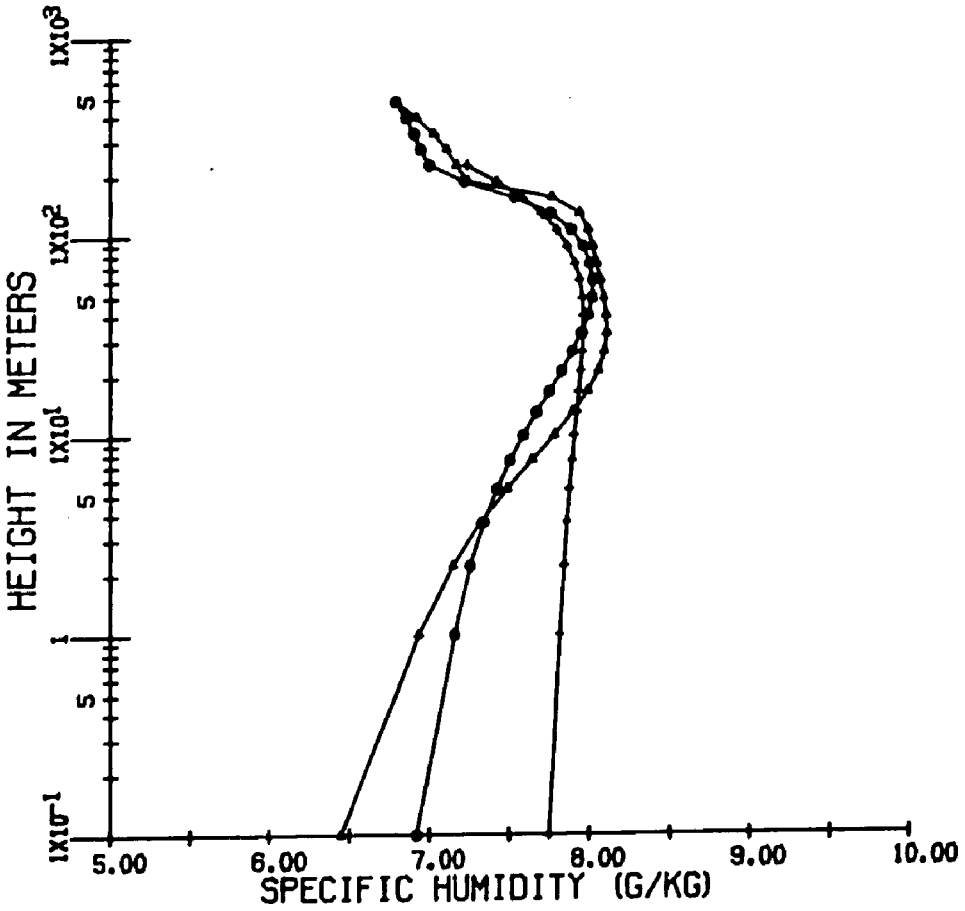


Fig. 5.14: Profiles of q at t=7 hr.
(—●—): basic run; (—▲—): run G1;
(—+—): run G2

increased cooling at this level; thus, the earlier appearance of model fog.

The increased exchange coefficients of run G2 produce effects opposite to those shown by run G1--decreased cooling at the surface and lower levels of the atmosphere, increases cooling at higher levels, and parallel behavior of the q profile.

Considering the fact that initial values of K are reduced by roughly a factor of 3 when u_* is reduced from 10 to 3 cm sec^{-1}, the effect upon θ and q near the surface in run G1 is relatively small. For example, θ at 1 m cools by 9.44 K in 7 hours in the basic run, and by 9.98 K in 7 hours in run G1. The evaluation of each of the terms in the surface heat balance, given below for the basic run and run G1 at t=7 hr, may explain this result. All values given are in cal m^{-2} sec^{-1}; fluxes with positive values are directed away from the surface.

	basic run	run G1
net long wave flux	22.84	21.62
turbulent flux of sensible heat	-3.46	-1.24
turbulent flux of latent heat	-1.61	-0.85
soil heat flux	-17.77	-19.53

The turbulent flux of sensible heat from the atmosphere toward the surface is far smaller than either the net long-wave flux or the flux of heat from the soil.

Thus, a large relative change in the turbulent flux of sensible heat is compensated by much smaller relative changes in the larger terms, and the surface heat balance in run G1 is satisfied at surface temperatures only slightly cooler than in the basic run.

Model run G3 was made with the turbulent exchange coefficient set equal to zero at all levels. Model fog forms in run G3 at t=3.76 hr. Fig 5.15 compares the behavior of θ at 1 m in the basic run and in run G3. In the absence of turbulent exchange, long-wave flux divergence is the only mechanism which can cool the model atmosphere. Long-wave flux divergence, acting alone in run G3, produces nearly the same amount of cooling at 1 m (although not at higher levels) as do the combined divergences of the turbulent and radiative fluxes in the basic run. Without turbulence, the formation of dew cannot induce low-level atmospheric moisture loss, and fog forms early in the model run. Indeed, the fog which forms in run G3 can accurately be termed "radiation fog." The results of run G3 suggest that a period of calm occurring when the air near the ground is close to saturation may trigger fog formation.

H. EFFECT OF FOG PARAMETERS

The bulk mass absorption coefficient k_w was assigned a value of 0.15 $m^2 g^{-1}$ in the verification experiment. Model runs H1 and H2 were made on case 3 of the previous chapter

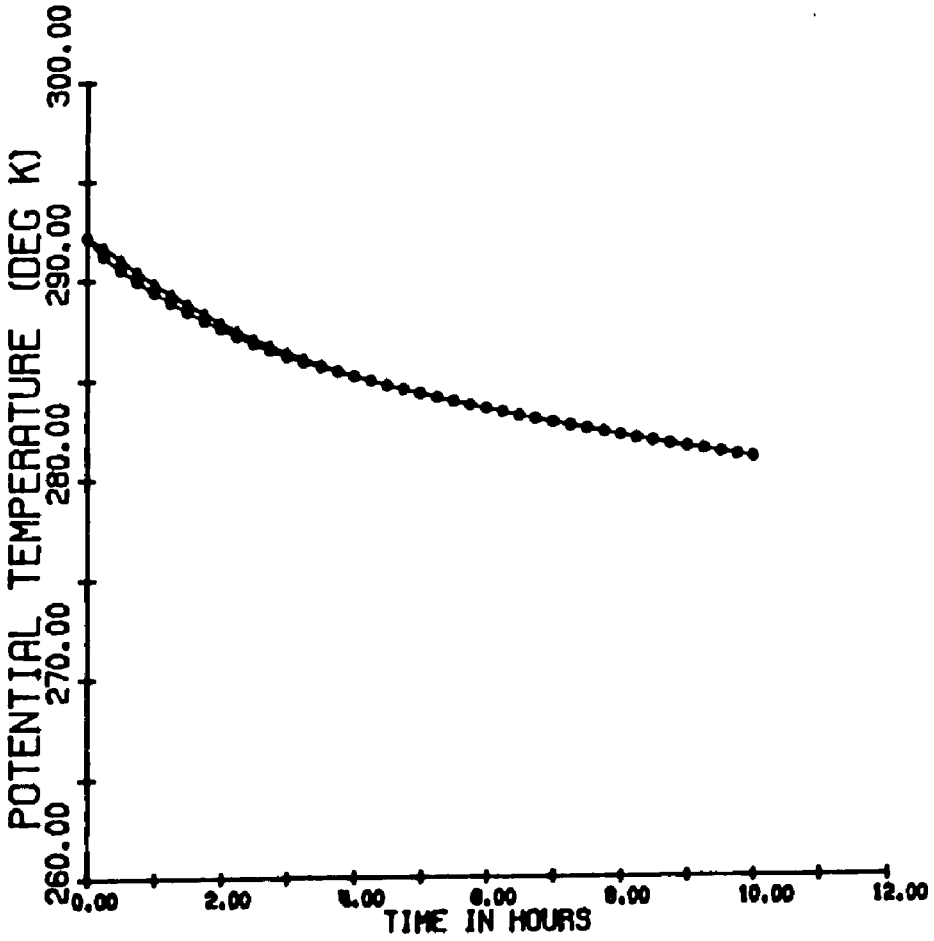


Fig. 5.15: Model-predicted θ at z = 1 m.
(—●—): basic run; (—▲—): run G3

Basic run: $u_* = 10$ cm sec^{-1}
Run G3: $u_* = 0$

with assigned k_w values of 0.06 and 0.30 $m^2 g^{-1}$, respectively. Run H1, like the case 3 basic run, was terminated at t=6 hr. Run H2 was terminated at t=4.25 hr, when large oscillations in model-predicted ℓ began to appear.

Figures 5.16 and 5.17 compare θ and ℓ at 1 m in the case 3 basic run, run H1, and run H2. Figure 5.18 compares the profiles of ℓ in the three runs at t=4 hr, and Fig. 5.19 compares the profiles of ℓ in the basic run and in run H1 at t=6 hr. When k_w is increased, ℓ increases earlier and more explosively than in the basic run; the profile of ℓ at t=4 hr in run H2 is very similar to the profile of ℓ at t=6 hr in the basic run. As in the basic run, the cooling rate of 1 m increases during the period of explosive fog growth, in contradiction to observations. When a smaller value of k_w is assumed, ℓ increases more slowly; maximum values of ℓ attained in run H1 are considerably closer to measured values than are the maximum values of ℓ in the basic run. However, the amount of cooling which takes place at 1 m between model fog onset and t=6 hr is virtually the same in the two runs.

The parameter s, which relates mean droplet fall velocity to liquid water concentration, was assigned the value 6.25 in the verification experiment. In model run H3, no droplet settling was allowed. In run H4, s was assigned a value of 15. Figures 5.20 and 5.21 compare θ and ℓ at 1 m in the case 3 basic run, run H3 and run H4.

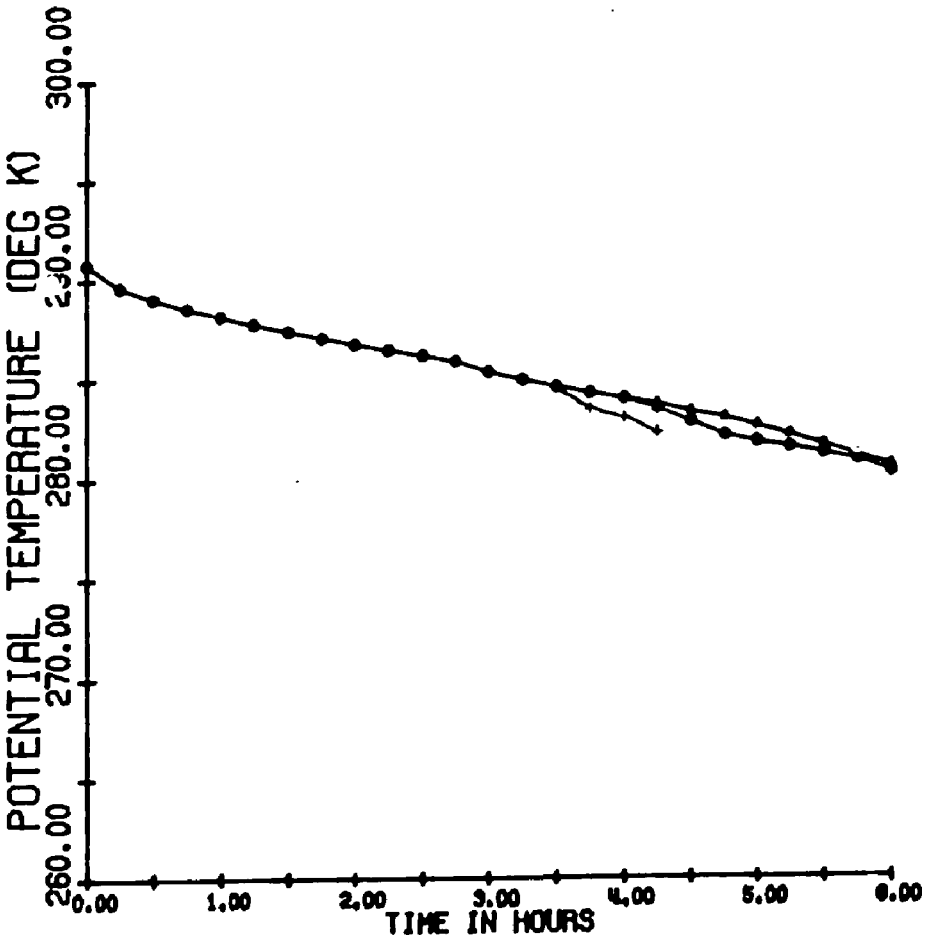


Fig. 5.16: Model-predicted θ at z = 1 m.
(-●-): basic run; (-▲-): run H1;
(-+-): run H2

Basic run: $k_w = 0.15$ $m^2 g^{-1}$
Run H1: $k_w = 0.06$ "
Run H2: $k_w = 0.30$ "

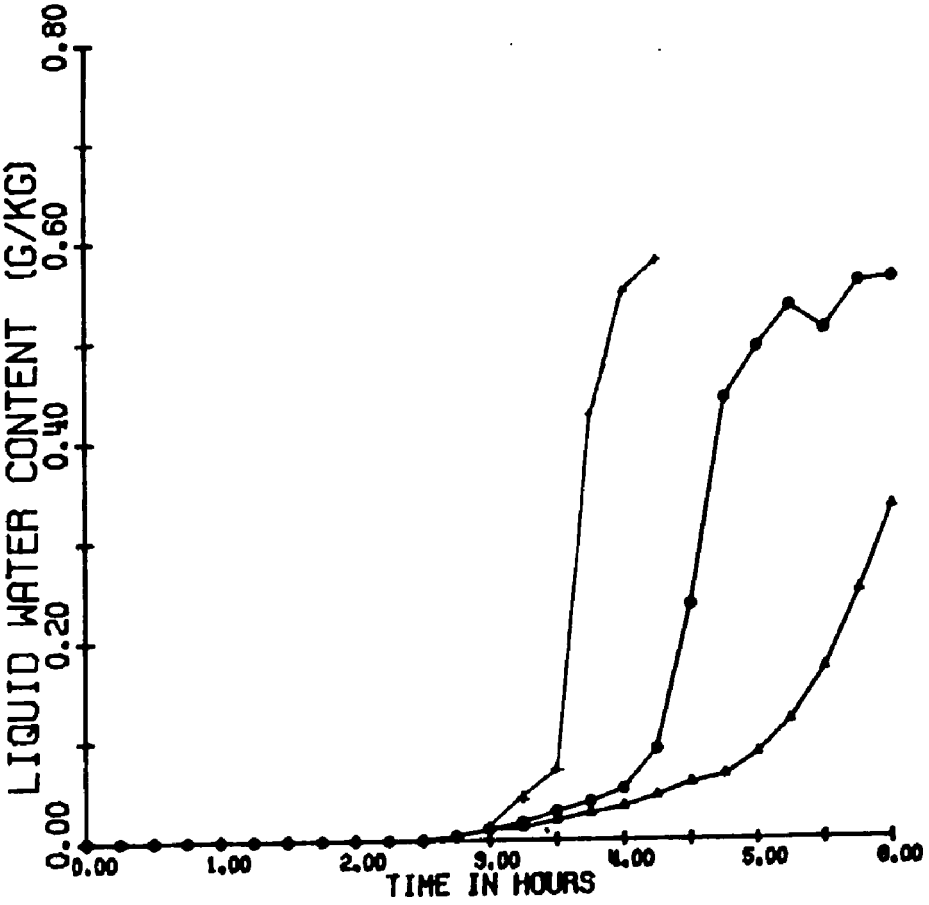


Fig. 5.17: Model-predicted ℓ at z = 1 m.
(—●—): basic run; (—▲—): run H1
(—+—): run H2

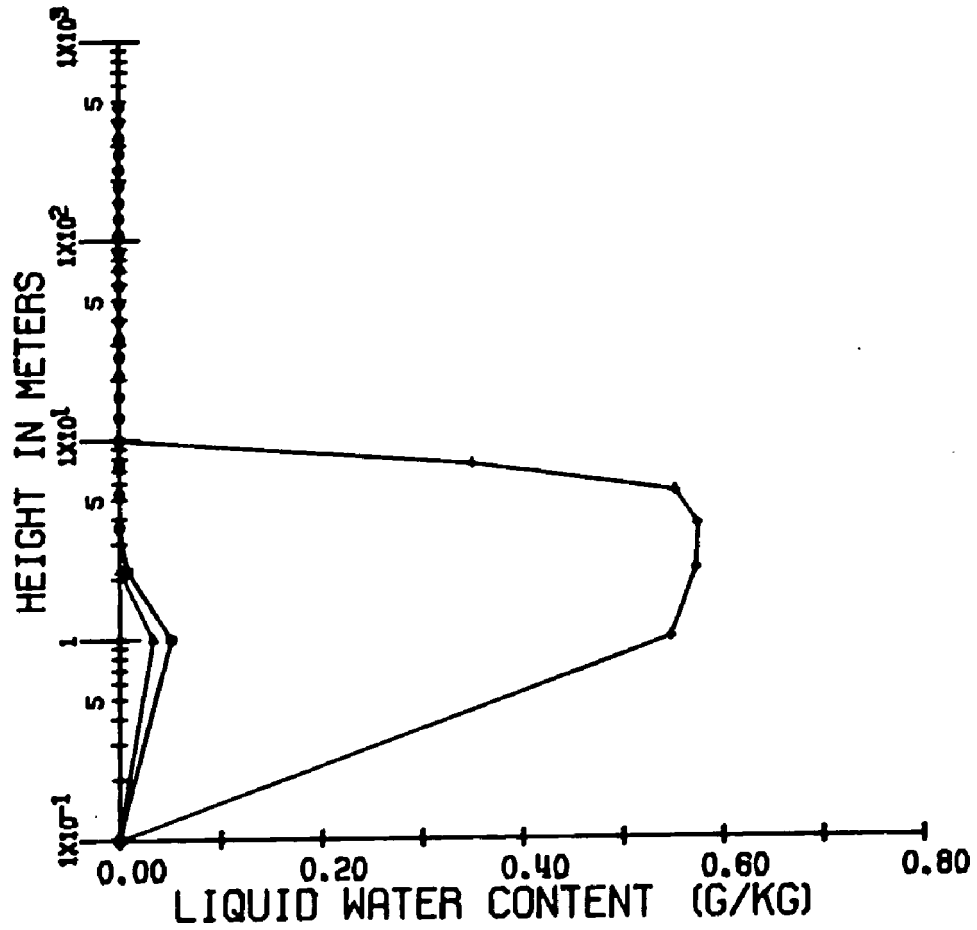


Fig. 5.18: Profiles of ℓ at t=4 hr.
(—●—): basic run: (—▲—): run H1;
(—+—): run H2

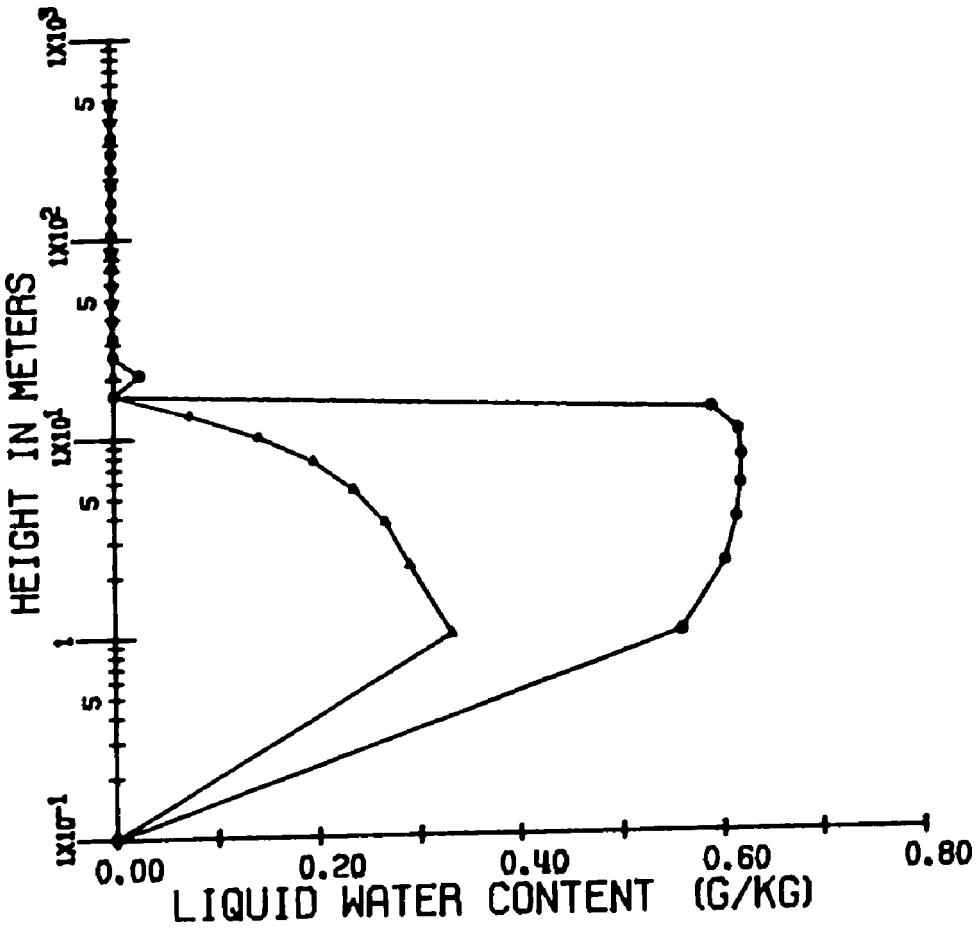


Fig. 5.19: Profiles of ℓ at t=6 hr.
(—●—): basic run; (—▲—): run H1

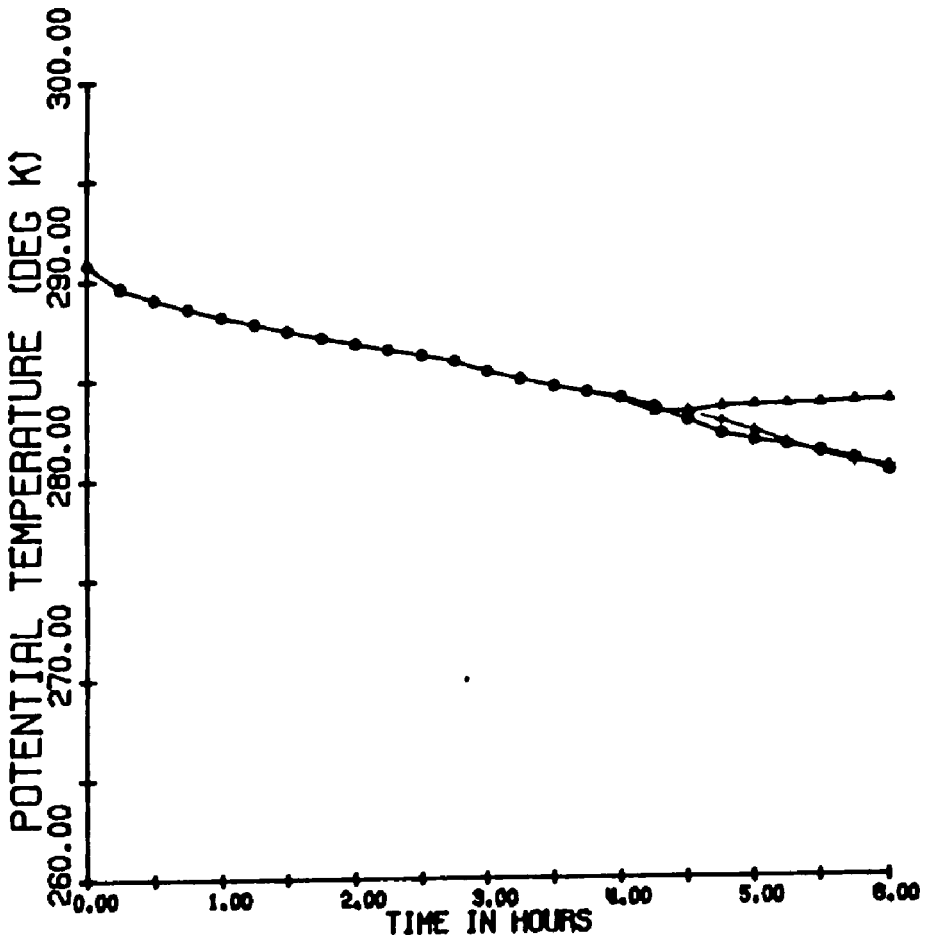


Fig. 5.20: Model-predicted θ at z = 1 m.
(—■—): basic run; (—▲—): run H3;
(—+—): run H4

Basic Run: s = 6.25
Run H3: s = 0
Run H4: s = 15

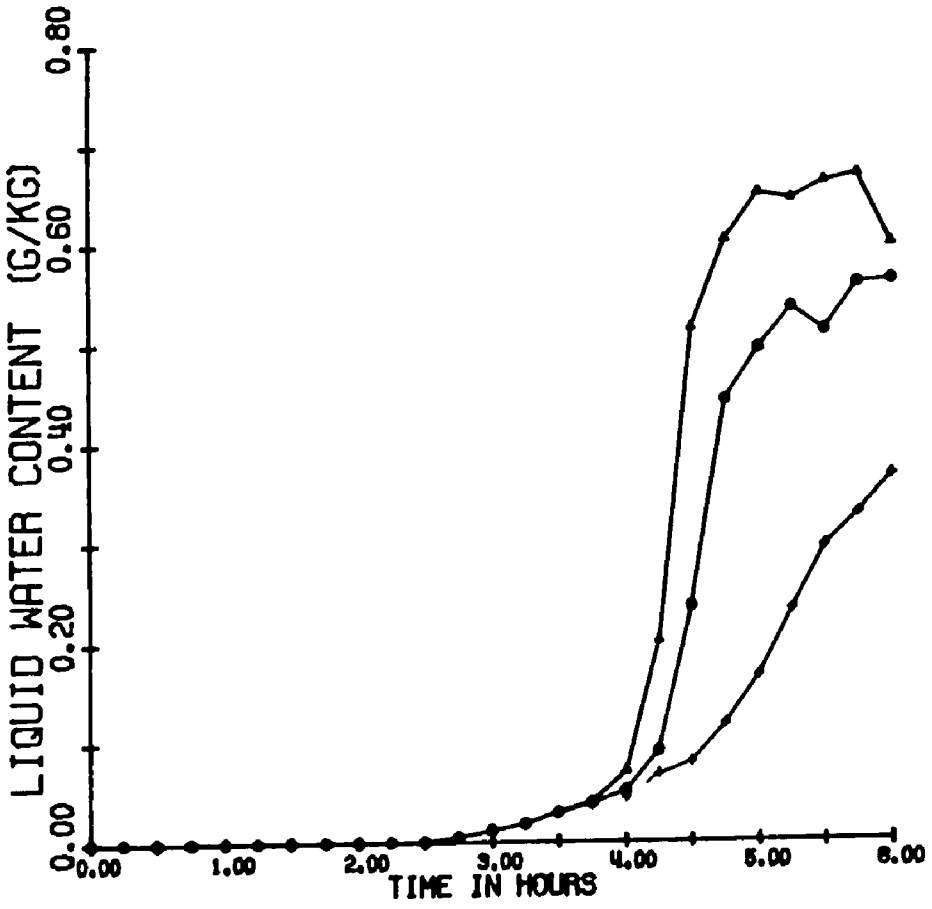


Fig. 5.21: Model-predicted ℓ at z = 1 m.
(—●—): basic run; (—▲—): run H3;
(—+—): run H4

Figure 5.22 compares the profiles of ℓ at t=6 hr. The suppression of droplet settling in run H3 allows model fog to grow to a height of 60 m; ℓ increases sharply with height to values exceeding 1.2 g kg^{-1} at the fog top. The large amount of liquid water in the model column reduces net surface radiative heat loss sufficiently so that θ rises at 1 m after t=4 hr. In run H4, increased droplet settling velocities limit liquid water concentrations and fog upward growth, but the θ decrease at 1 m during model fog is similar to that in the basic run.

The formulation of this model does not provide realistic predictions of <u>both</u> θ and ℓ in a fog situation. The assumption that a developing fog can be characterized by values of k_w and s which are constant with height and time appears not to be valid in this context. Additionally, k_w does not account for the scattering of long-wave radiation by fog droplets, a process which Zdunkowski and Barr (1972) suggest may reduce long-wave cooling within fog.

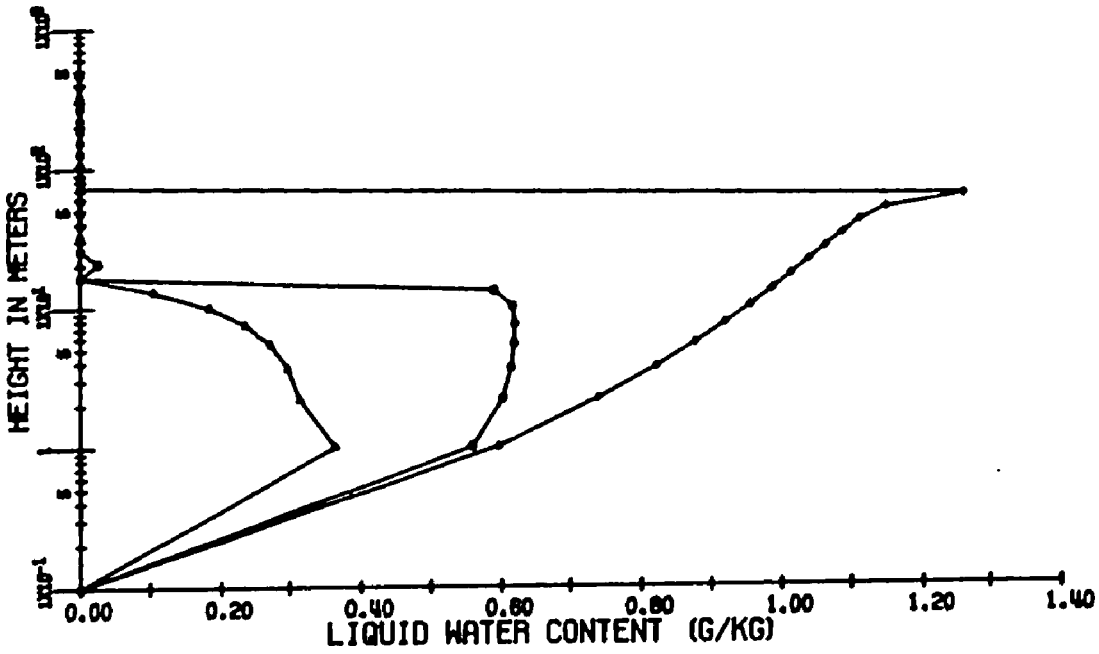


Fig. 5.22: Profiles of ℓ at t=6 hr.
(-●-): basic run; (-▲-): run H3;
(-+-): run H4

CHAPTER VI: CONCLUSIONS

This study has involved the development and testing of a numerical model which predicts the onset and development of fog on clear nights. The model has been verified against observations. Additionally, the sensitivity of the model to alterations of several assumptions and parameters has been investigated.

The results of the study indicate that the model is potentially viable as an aid in forecasting the onset of fog. The model predicted fog in eight of eleven cases in which fog was observed to form on clear nights at Flint, Michigan. In each case in which observed fog was verified by the model, predicted and observed fog onset times were within two hours of one another. Temperatures predicted by the model were generally within 1 to 2°C of those observed.

With all parameter values identical to those assumed in the fog cases, the model was applied to six cases in which no fog was observed at Flint. The model predicted fog in five of the six cases. It was noted that model-generated 1 m temperatures were significantly lower than observed shelter-level temperatures in all but one of the no-fog cases: this suggested that model-generated turbulent exchange coefficients were too low. When the model was re-run with u_* increased from 10 to 15 cm sec^{-1},

model fog appeared in only one case of the six, and the agreement between model-predicted and observed temperatures improved.

If the model in current form is to be used to distinguish between fog and no-fog situations, a method of assigning u_* is essential. Observations of mean wind speed and temperature at two levels, if available, would allow computation of u_* from the Monin-Obukhov expression for wind shear. Alternatively, the variance of the wind direction and/or wind speed, observed over a specified period preceding model initialization, might serve as a basis for an estimate of u_*.

The study has indicated several areas in which further research is needed for improved fog forecasting. The most prominent of these is the relationship between dew and fog. The rate at which dew formation removes moisture from the atmosphere has been shown to be a crucial factor governing the appearance of fog. Measurements of dew accumulation and of the moisture flux in the first meter of the atmosphere are necessary if the modeling of the effects of dew formation is to be improved.

Turbulent exchange influences fog formation through its effect upon the behavior of θ and q. Model results show that relatively high levels of turbulence inhibit fog formation by limiting the cooling of the first few meters of the atmosphere. On the other hand, turbulent

exchange which is weak or absent enhances the likelihood of fog, primarily by reducing the flux of moisture toward the surface.

The use in the current model of a constant friction velocity as a basis for computations of the turbulent exchange coefficient is of doubtful validity, especially under conditions of extreme stability. The relative success of model θ prediction in the verification experiment may well be ascribed to the fact that the combined effect of turbulent and radiative heat flux divergences does not depend strongly on K when K is small. However, the specific humidity in the absence of fog is governed solely by the divergence of the turbulent moisture flux, which depends heavily upon the magnitude of K. A more realistic treatment of turbulent fluxes is needed to improve the prediction of q, and thus to improve the prediction of fog by the model.

Simultaneous observations of the mean fluxes and gradients of heat and moisture on clear nights might improve the parameterization of K. The application to nocturnal fog prediction of higher-order closure models, which predict the turbulent fluxes directly, might also be investigated.

The time of model fog onset has been shown to be very sensitive to variations in the relative humidity required for condensation. The relative humidity at which conden-

sation takes place in the atmosphere decreases as the number of available condensation nuclei increases. Application of the fog model in or near polluted urban areas would thus require that the availability of condensation nuclei be taken into account. Nuclei concentrations would have to be measured or estimated, and a relationship between condensation relative humidity and the concentration of nuclei would have to be determined. Use of the fog model in conjunction with area-wide air quality models might be explored.

Soil characteristics influence the formation of fog through their effect upon the surface heat balance. Knowledge of soil density, specific heat, and diffusivity at a given location would be necessary for operational use of the current model. A relationship between each of these parameters and the wetness of the soil need to be developed experimentally. A simple model of diurnal heating in the soil might be used to improve soil temperature initialization in the fog model.

Model prediction of fog liquid water concentration and vertical extent was relatively poor. Model results were similar for cases in which ground fog and deep fog were observed. The observed increase in temperature near the surface in the deep fog case could be simulated only by suppressing droplet settling, a measure which resulted in extremely large values of ℓ. It is apparent that a

constant mass absorption coefficient is not sufficient to represent the interaction between a developing fog and long-wave radiation. Parameterization of this interaction in the model would be improved if measurements of liquid water concentration and long-wave flux could be carried out at more than one level of a fog.

In summary, this study has shown that operational numerical prediction of nocturnal fog onset is feasible. The weakness of the model in predicting fog liquid water concentrations makes operational numerical prediction of fog visibility and vertical extent questionable at this point. Further model improvement requires a firmer quantitative understanding of the processes discussed above, an understanding which, for the most part, can only be gained through observations.

REFERENCES

Blackadar, A.K., 1962: The vertical distribution of wind and turbulent exchange in a neutral atmosphere. J. Geophys. Res., 67: 3095-3102.

Brooks, D. L., 1950: A tabular method for the computation ot temperature change by infrared radiation in the free atmosphere. J. Met., 7: 313-321.

Brown, R., and W.T. Roach, 1976: The physics of radiation fog: a numerical study. Quart. J. R. Met. Soc., 102: 335-354.

Eldridge, R.G., 1971: The relationship between visibility and liquid water content in fog. J. Atmos. Sci., 28: 1183-1186.

Businger, J.A., 1973: Turbulent transfer in the atmospheric surface layer. Workshop on Micrometeorology, American Meteorological Society, pp. 67-98.

Fisher, E.L. and P. Caplan, 1963: An experiment in numerical prediction of fog and stratus. J. Atmos. Sci., 20: 425-437.

Geiger, R., 1961: The Climate Near the Ground. Harvard University Press, 611 pp.

George, J.J., 1950: Fog. Compendium of Meteorology, American Meteorological Society, pp. 1179-1189.

Kolenkova, S.I., 1971: Characteristics of some atmospheric parameters in the boundary layer under fog conditions. Meteorologiia I Gidrologiia, 7: 20-27.

Lala, G.G., E. Mandel, and J.E. Jiusto, 1975: A numerical evaluation of radiation fog variables. J. Atmos. Sci., 32: 720-728.

Lumley, J., and H. Panofsky, 1964: The Structure of Atmospheric Turbulence. Interscience Publishers, 239 pp.

Mack, E.J., and W.J. Eadie, C.W. Rogers, W.C. Kocmond, and R.J. Pilie, 1973: A field investigation and numerical simulation of coastal fog. NASA Contractor Report CR-2201.

McDonald, J.E., 1963: The saturation adjustment in numerical modelling of fog. J. Atmos. Sci., 20: 476-478.

Pilie, R., W. Eadie, E. Mack, C. Rogers, and W. Kochmond, 1972: Investigations of warm fog properties. NASA Contractor Report CR-2078.

Ramanathan, V., 1976: Radiative transfer within the earth's troposphere and stratosphere: a simplified radiative-convective model. J. Atmos. Sci., 33: 1330-1346.

Staley, D.O., and G.N. Jurica, 1970: Flux emissivity tables for water vapor, carbon dioxide, and ozone. Appl. Meteor., 9: 365-372.

Zdunkowski, W., and B. Nielsen, 1969: A preliminary prediction analysis of radiation fog. Pure Appl. Geophys., 75: 278-299.

Zdunkowski, W. and A.E. Barr, 1972: A radiative-conductive model for the prediction of radiation fog. Boundary Layer Met. 2: 152-177.